Electrical plasma diagnostics for the measurement of ion related parameters at the substrate surface

Shailesh Sharma

2017

ELECTRICAL PLASMA DIAGNOSTICS FOR THE MEASUREMENT OF ION RELATED PARAMETERS AT THE SUBSTRATE SURFACE

Shailesh Sharma, M.Tech.

Thesis submitted for the degree of

DOCTOR OF PHILOSOPHY

Presented to

School of Electronic Engineering

Dublin City University

Research Supervisor:

Dr. Stephen Daniels

Dublin City University

December 2016

Declaration

I hereby certify that this material, which I now submit for assessment on the programme of study leading to the award of Doctor of Philosophy, Ph.D, is entirely my own work, and that I have exercised reasonable care to ensure that the work is original, and does not to the best of my knowledge breach any law of copyright, and has not been taken from the work of others save and to the extent that such work has been cited and acknowledged within the text of my work.

Signed:............................   ID No.: 13210397   Date: ....

Acknowledgements

After an intensive period of three years, today is the day when I am writing this note of thanks to everyone who contributed in this research work and supported in various ways. Though only my name appears on the cover of this thesis, many other people have significantly contributed to its production. I owe my gratitude to all the employees of Impedans Ltd. who have made this dissertation possible in such a short time.

My deepest gratitude is to my employment mentor Dr. David Gahan (C.T.O., Impedans Ltd.) who not only helped me to come and settle in Ireland but also took personal care of me during this period. I have been amazingly fortunate to have such an knowledgeable and experimentalist advisor. You taught me all basic things including background literature as well as experimental techniques to step forward in this research work. Your constant open door policy, invaluable advice during all of my graduate years at Impedans and DCU made a hassle-free path for me. I am also thankful to you for encouraging the use of correct grammar and

Contents

List of Figures

10

11

12

13

Abstract

Shailesh Sharma

Electrical plasma diagnostics for the measurement of ion related parameters at the substrate surface

As the semiconductor industries are advancing towards atomic scale dimensions, the knowledge of ion related parameters is becoming critical while developing highly advanced plasma etch and deposition processes. This thesis presents novel plasma diagnostic techniques to measure ion related parameters at the wafer surface. These techniques based on retarding field analyzer adds important functionality to this sensing technology and can provide useful insight which is intensely desired to meet the future needs of nano-manufacturing industries.

Plasma spatial profile in terms of ion energy and ion flux, ion angular distribution and ionized flux fraction are crucial parameters which can greatly influence ion enhanced plasma deposition and etch processes for the fabrication of next generations of sub - 10 nanometre integrated circuits. Ion related parameters measured in the bulk of the plasma may not precisely predict on how ions will interact at the surface of the substrate. Planar retarding potential analyzer is the most appropriate diagnostic which measures ion related parameters exactly on the surface of the substrate. In this thesis, we have demonstrated various possible methods with appropriate modifications in the existing sensor design to

improve its measurement functionality and subsequently help semiconductor industry develop tightly controlled plasma processes to achieve smallest possible feature size that can be created in the wafer.

The work in this thesis focuses on the measurement of a number of ion related parameters to investigate a variety of plasma assisted processes using newly developed techniques and modified designs of the sensor. The modified geometries associated with novel techniques are useful extensions to this sensing technology which makes it an attractive plasma diagnostic suitable to achieve the future needs. The main findings of this thesis concludes that measurement of ion related parameters at the location of the wafer surface using novel sensor design and techniques can provide useful means to process engineers in developing and control highly precise plasma processes.

CHAPTER 1

Introduction

1.1 Plasma processing for nanoelectronics

Following Moore's law, transistors/chip have been doubling every two years since 1959. Fabrication of CMOS transistors involves various deposition and etching processes. Isotropic etching of Si, W, Ta, Ti, Si_3N_4 was first demonstrated by researchers in 1970. It was a slow process and the need for faster etching was recognised. Plasma etching produces volatile products and low ion energies, while sputtering produces involatile products and high ion energies. Hosokawa *et al* [1] combined the volatile etch products with high ion energies to etch faster. In 1974, he introduced a mixture of fluoro-chloro-hydro-carbon as a sputtering gas in the reactor and achieved enhanced etching rates. Following his discovery, various reactive ion etching processes have been developed and anisotropic plasma
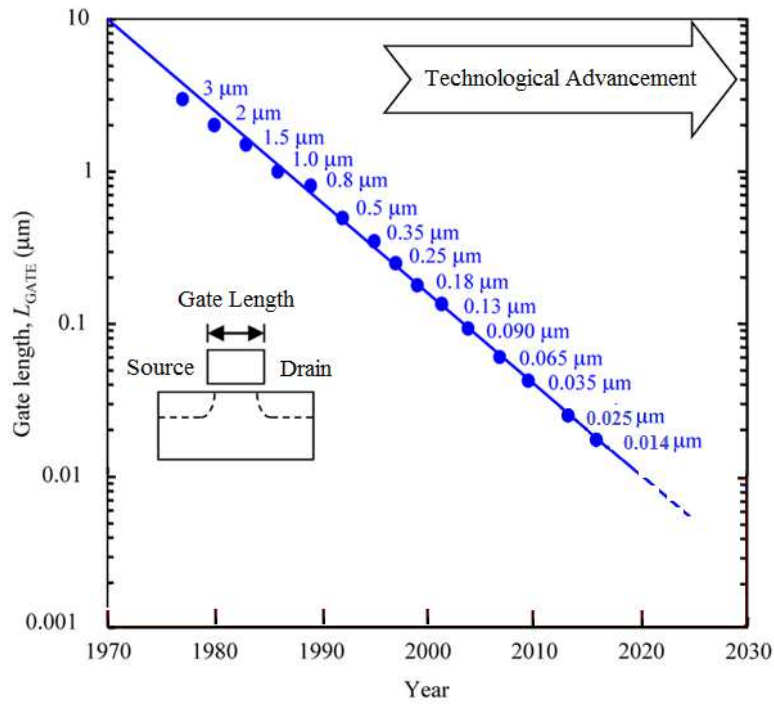
Figure 1.1: *Reduction in CMOS gate length over the years*

etching was born. Anisotropic etching enabled process engineers to build vertical structures using the wafer fabrication techniques. Increased precision in vertical patterning has given rise to a race of miniaturizing the CMOS transistors, and the gate lengths have started shrinking towards minimum possible values. Intensified research and development in plasma processes brought continuous reduction in CMOS gate lengths as shown in figure 1.1 [2]. As feature dimensions on a semiconductor chip continue to decrease in size, it will soon reach the dimensions on an atomic scale. CMOS gate lengths are expected to scale down as low as 30-atom dimensions in 2024. Atomic layer deposition (ALD) and atomic layer etching (ALE) are the recent technological advancements in which few atomic layers of material are being deposited and etched away for the creation of ever reducing dimensions. Plasma enhanced chemical va-

por deposition (PECVD), ionized physical vapor deposition (I-PVD) and high-power impulse magnetron sputtering (HiPIMS) are other types of deposition plasma processes which see widespread use in extremely small scale integrated circuit fabrication. As we enter the era of atomic-scale dimensions, precisely controlled plasma processes to create those tiny features are required to meet the future needs. Greater level of control over plasma processes is not possible unless various ion related parameters are measured and then tuned according to the requirement.

1.2   Role of ions during plasma processing

Ions play a crucial role during plasma processing of semiconductor wafers. There are a number of ion related parameters which need to be measured and controlled while developing a highly precise plasma process for the manufacturing of next generation integrated circuits (IC). Flux of ion species bombarding the wafer surface and the energy they have at impact are of particular importance in determining the process outcome. The sheath adjacent to the substrate surface controls the flux and the energy of ions impacting the substrate [3]. For deposition plasma processes, flux and bombarding energy of the ions directly affect the deposition rate and properties of the depositing film [4]. In dry etching applications where physical ion milling action takes place, the ion flux to the substrate surface influences the etch uniformity while the ion energy determines etch selectivity and etch rate [5, 6]. Spatial plasma profile, specifically uniformity of ion energy and ion flux across the wafer surface, is one of the salient parameters which can influence localized device performance.
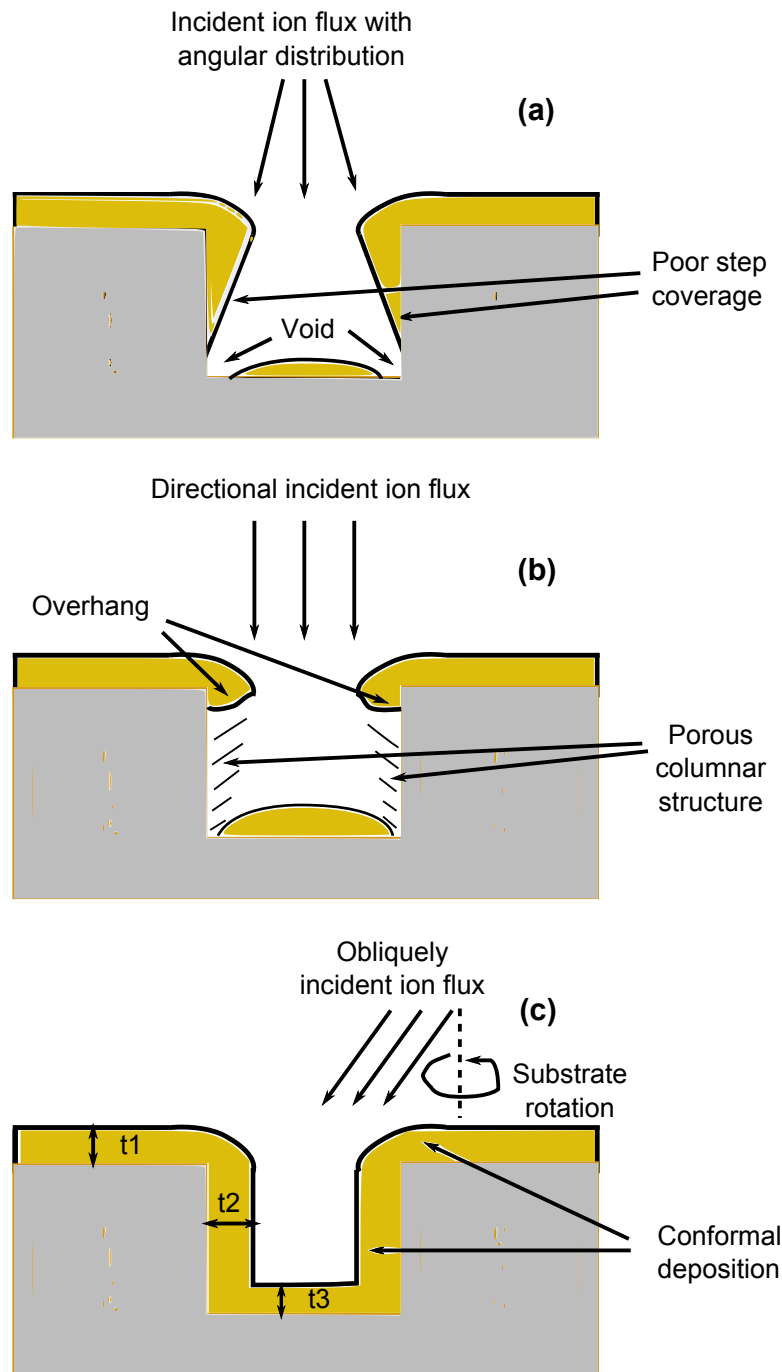
Figure 1.2: *Structure of the films deposited in trenches/vias (a) the incident flux is not directional and has a random angular distribution, (b) the incident flux is directional and normally incident to the substrate, (c) the incident flux is at fixed oblique angles relative to surface normal and substrate is rotated at certain speed.*

During the fabrication of integrated circuits, thin films of conducting materials are often deposited on nonplanar surfaces with deep vias and trenches which are patterned using dry/wet etching techniques into insulating layers called the interlayer dielectrics (ILD). The metal connecting lines at each layer are formed by filling trenches and vias in the ILD. The angular distribution of ions is one of the key parameters which can control conformality of deposited films over the trenches. Depending on plasma sheath thickness, intensity of sheath electric field and ion mean free path, the ions may hit the substrate in a direction perpendicular to the surface or at oblique angles relative to the surface normal. Step coverage (which is defined as the ratio of film thickness on the sidewall of the trench to film thickness on the top horizontal surface), bottom coverage (which is defined as the ratio of film thickness on the bottom of the trench to film thickness on the top horizontal surface) and film overhang (which is the material overhanging at the mouth/edge of the feature) are important aspects to be considered during metallization of high aspect ratio trenches which depends on ion angular distribution. Ions incident perpendicular to the surface may lead to poor step coverage on sidewalls while ions incident at oblique angles may lead to poor bottom coverage and can also form overhanging structures at the top corners of the trenches. Overhanging structures may block further deposition of the material into the trenches. All these effects can lead to void and pinhole formation when attempting to fill a surface feature. Karabacak *et al* [7] studied the effect of ion angular distribution on conformality of films sputter deposited over deep trenches/vias which is illustrated in figure 1.2. In (a) the incident ion flux is not directional and has a random angular distribution. The film deposition on the sidewall and bottom of the trench is less prefer-

(a)

Incident ion flux with
angular distribution

Undercut

Mask Layer

Etch Material
(e.g. Silicon)

(b)

Directional
incident ion flux

Mask Layer

Etch Material
(e.g. Silicon)
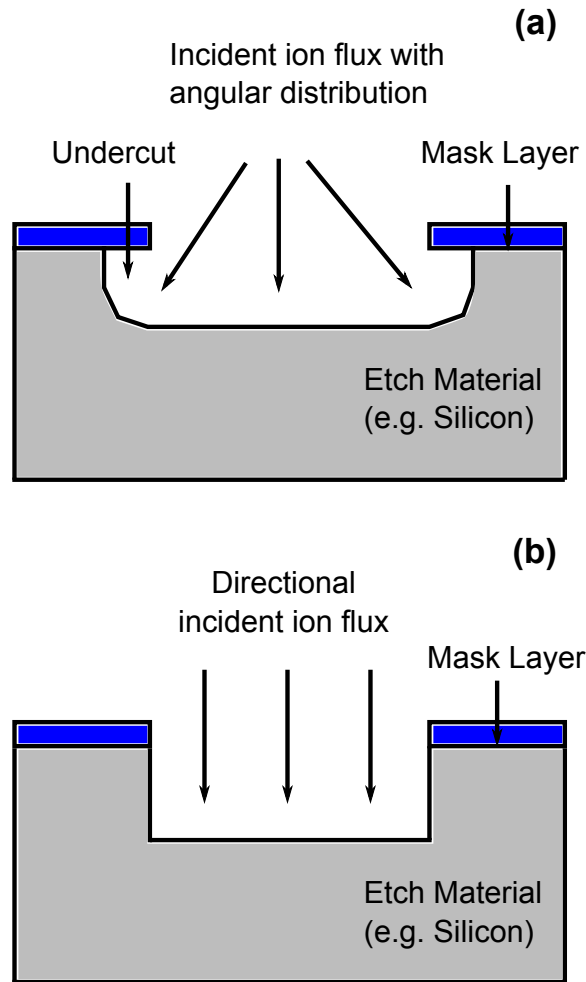
Figure 1.3: *(a) the incident ion flux has an angular distribution, (b) the incident ion flux is directional.*

ential than the top horizontal surface, leading to poor step and bottom coverage as well as void formation. In (b) the incident ion flux is directional and normally incident to the substrate. In this case, ions approach the sidewalls of the trench at high oblique angles $\sim 90^o$ with respect to the sidewall's surface normal and preferentially deposit on the upper regions of the sidewall. This causes a columnar, porous structure of the film forming on the sidewalls and more material overhanging at the corners which again gives rise to poor sidewall coverage (step coverage) and formation of voids. In (c) ions are allowed to impinge at fixed oblique angles from the surface normal, while the substrate is rotated around the axis at a certain speed so that particles can uniformly reach inside the entire trench surface. In this case, the overall coverage becomes more conformal (t1 $\sim$ t2 $\sim$ t3), void-free, and has a better step and bottom coverage as compared to that obtained by normal incidence deposition.

In anisotropic etching applications, ions are directed normal to the substrate surface and high directivity of the ions is required for producing high aspect ratio (depth to width) trenches. Ion angular distribution is the key parameter to control directivity of the ions. Nearly 90^0 profile, parallel to the surface normal, is desired for higher etch rate in vertical direction than in lateral direction. Ions striking the wafer at oblique angles from the surface normal may cause a loss of anisotropy in film etch and other unwanted damage of sidewalls (leading to undercut below the mask layer). In figure 1.3 the effect of ion angular distribution is shown on an etched structure when (a) the incident ion flux has an angular distribution which leads to undercutting problems (b) the incident ion flux is directional which results in the formation of vertical trench profile.

In sputter deposition processes when ion energies are high, the de-

posited film is supposed to be the result of two simultaneous competing processes: film deposition by target material species and film resputtering by background gas ions. The resputtering process causes the deposited particles to liberate back and return to the vapour phase. This resputtering process is a function of bombarding energy and incidence angle of the gas ions. The parameters which control energy and angle distribution of ions include the bias voltage, the ion density, the gas composition, and the mean free path (which also depends on the aforementioned parameters). The sputter/re-sputter yield of most materials increases with the increasing angle of ion incidence (from the surface normal) due to the increase in energy transfer closer to the surface and shows a maximum between 60^0 to 75^0 and then decreases at large glancing angles due to increase of ion reflection from the target surface. Resputtering process is briefly illustrated in figure 1.4 [8].

As semiconductor manufacturers continue to shrink feature sizes, undercutting and poor sidewall coverage in etch and deposition processes respectively are becoming more intolerable, and a tight control over the ion angular distribution is desired. Another factor influencing degree of anisotropy in accelerated ion assisted etching applications is the ion-to-neutral flux ratio, as the etch species can either be charged ions or neutral atoms/molecules. For infinitely large ratio (i.e. no neutrals), no neutral species are incident on the sidewalls and etching is perfectly vertical, while for zero ratio (i.e. no ions), all surfaces are subjected to same neutral flux and etching is isotropic. In deposition processes, thin film quality and deposition rates are also strongly dependent on the ion-to-neutral ratio. Researchers [9–11] have shown that film properties (microstructure, morphology, intrinsic stress, hardness) significantly
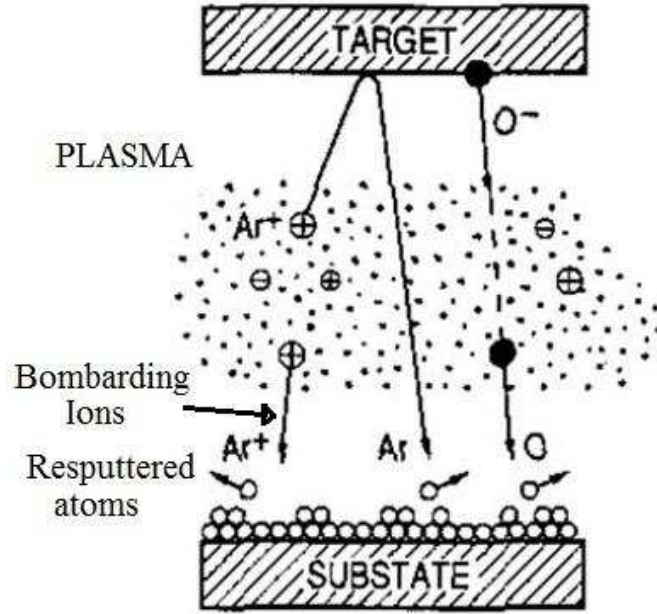
Figure 1.4: *Resputtering of deposited atoms by the energetic ions*

depend upon the ion/neutral flux ratio during the deposition process.

With ongoing miniaturization of IC's (shrinking feature size and increasing aspect ratio), there is a need to measure ion related parameters such as ion mass and their charge states, ion energy, ion flux, incident ion angle and ion-to-neutral flux ratio at the substrate surface in order to develop high precision plasma processes.

Various optical and electrical diagnostic techniques to deduce the information about the state and characteristics of the plasma have been developed in recent decades . Optical techniques rely on either the optical emission from the plasma or an external light source to probe the plasma species, whilst electrical techniques include plasma diagnostic techniques that measure electrical signals generated by the plasma, either as a part of its normal behaviour or in response to other electrical signals applied

as stimuli by the experimenter.

1.3   Existing diagnostics to measure ion parameters

Various plasma diagnostics exist to measure a number of ion related parameters. Among the key parameters which can be measured in a plasma process are ion current density, mass spectrum of ions, ion energy distribution, etc. Common plasma diagnostics are briefly described here.

1.3.1   Faraday probe

The faraday probe is a diagnostic tool used to measure the ion current density distribution in a plasma. A standard faraday probe consists of a flat plate metallic collector that is biased at potentials below plasma potential to ensure that plasma electrons are repelled. Thus, a good estimate/measurement of electron temperature and plasma potential is essential to any good faraday probe survey. When ions hit the face of the collector, electrons contained within the metal of the faraday probe stream to the probe's face to neutralize the collected ions. These moving electrons make up the probe current, which is equal to the ion current. Ion current density is determined by measuring the ion current and dividing by the area of the collector.

1.3.2   Mass analyzer

Mass analyzers are used to measure the mass spectrum of ions. There are several designs which have been used over the years [12, 13], some

with more universal applicability than others, and some with particular interest because of their compact nature. All commonly used mass analyzers use electric and magnetic fields to apply a force on charged particles (ions). From Newton's second law, it is apparent that the force causes an acceleration that is mass dependent, and the Lorentz force law tells us that the applied force is also dependent on the ionic charge. And therefore, mass analyzers separate ions according to their mass-to-charge ratio (m/q), rather than by their mass alone. Schematics of different types of mass analyzers are shown in figure 1.5 [14–16].

Magnetic sector mass analyzer

The magnetic sector separates ions of different m/q ratio by first accelerating them through a potential and then directing them to a uniform magnetic field perpendicular to their direction of motion. As moving ions enter a magnetic field, they experience two equal forces: force due to the magnetic field and the centripetal force. Ions with varying m/q ratio are deflected to a circular motion of a varying radius in a direction perpendicular to the applied magnetic field. Based on their path radius, ions travel to a set of exit slits. Each exit slit selects ions of a certain m/q ratio which can be determined if both magnetic field magnitude and voltage difference for region of acceleration are held constant. They are used for mass focusing; they focus angular dispersions. Magnetic sector analyzers are usually larger and higher cost than other mass analyzers, and are not well-suited for pulsed ionization methods.
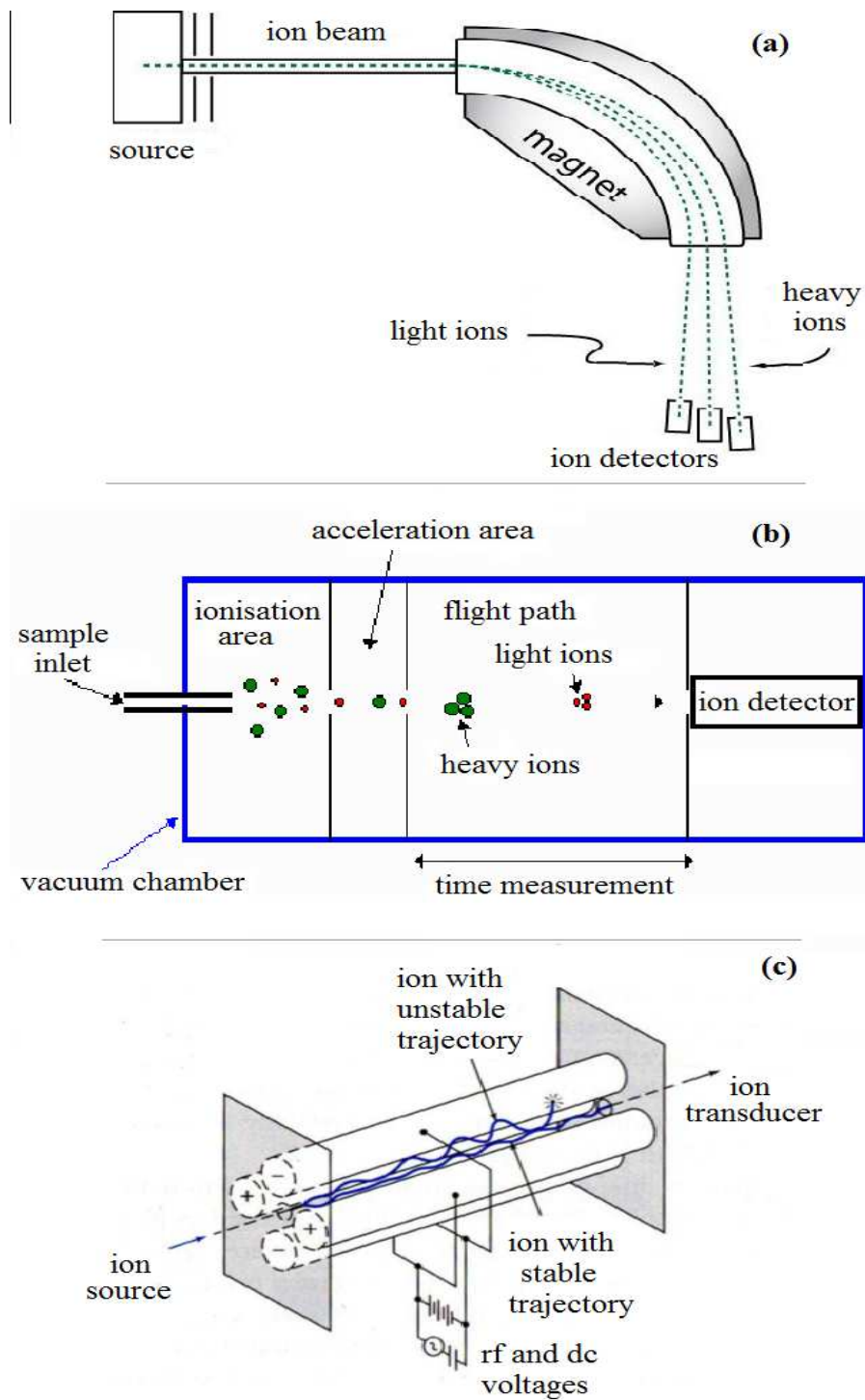
Figure 1.5: *(a) A magnetic sector mass analyzer, (b) time-of-flight mass analyzer and (c) quadrupole mass analyzer.*

Time of flight mass analyzer

Time-of-flight mass analyzer separate ions based on the kinetic energy and velocity in which ion's m/q ratio is determined via a time measurement. Ions are accelerated by an electric field of known strength. This acceleration results in an ion having the same kinetic energy as any other ion that has the same charge. The velocity of the ion depends on the m/q ratio. The time that it subsequently takes for the particle to reach a detector at a known distance is measured. This time will depend on the m/q ratio of the particle (light particles reach higher speed and heavier particles reach lower speeds). Time of flight is directly proportional to the root of the m/q ratio if the distance (length of tube) and the voltage from the ion source are held constant. In this way one can find the m/q ratio of the ion. Time of flight mass analyzers are well suited for pulsed ionization methods, as they provide better mass resolution compared to other types of mass analyzers, although at a price: a low duty factor and a more complicated set-up.

Quadrupole mass analyzer

A quadrupole mass analyzer is a linear arrangement of 4 cylindrical rod electrodes, set parallel to each other. Each opposing rod pair is connected together electrically, and a radio frequency (rf) voltage with a dc offset voltage is applied between one pair of rods and the other. Ions travel down the quadrupole between the rods. Only ions of a certain m/q ratio will reach the detector for a given ratio of voltages: other ions have unstable trajectories and will collide with the rods. This permits selection of an ion with a particular m/q or allows the operator to scan for a range of m/q values by continuously varying the applied voltage. Quadrupole

mass analyzers have limited resolution and are not well-suited for pulsed ionization methods.

Ion mass analyzers often require differential pumping to maintain a low enough pressure (of the order of 10^{-3} Pa) in the analyzer. The majority of elements have more than one stable isotope; presence of these isotopes give a multiplet structure which must be considered when analysing a mass spectrum to obtain quantitative densities. Some ion mass analyzers have limited resolution and are not well-suited for pulsed ionization methods. They are large in size, heavy in weight, and expensive.

1.3.3 Energy analyzer

It is often important to measure the energy distribution of the ions in a plasma. There are two most common analyzers to measure the energy of the ions: electrostatic sector analyzers, and retarding field analyzers (RFA).

Electrostatic sector analyzer

The electrostatic sector analyzer allows a direct measurement of the energy distribution function, but at the expense of a much reduced signal compared to the RFA (detailed in the next section). It is similar to a time of flight analyzer in that it separates the ions while in flight, using an electric field. Electrostatic sector analyzers can be of two types: (1) Parallel-plate electrostatic sector analyzers, which consist of two parallel plates separated by a distance. One of the plates is electrically grounded, while the other is biased to a positive potential. Ions enter through a sampling orifice and transit through a drift tube before entering the section composed of the two charged plates. The electrostatic field between

these plates causes the ion trajectories to curve in a parabola. At the output of the analyzer is a slit that leads to a detector. Due to the geometry of the system, only ions with a specific energy will reach the detector. By varying the field between the charged plates, the entire spectrum of ion energies can be measured. (2) Cylindrical electrostatic sector analyzers, which consist of two curved plates of equal and opposite potential, such that the electric field is radial. As the ion travels through the electric field, it is deflected, and the force on the radial component of velocity of the ion due to the electric field is equal to the centripetal force on the ion. The radial force on the ions maintains them in a circular orbit. This type of analyzer has the advantage of passing particles having a determined energy, and a sweep of the analyzer plates produces directly an energy spectrum. If the analyzer is in contact with a plasma, the slit width must be narrower than the Debye length to prevent plasma intruding inside. However, the signal is much reduced since the particle flux is limited by the entrance slit.

Retarding field analyzer

The most commonly used energy analyzer is the retarding field analyzer (RFA) or multi-grid analyzer, where a series of grids is used to select particles having a given charge sign, and to analyze the energy distribution of these particles. Depending on the grid biasing, the analyzer can be configured to measure energy distribution of either ions or electrons. The most usual application of the RFA is to measure ions from the plasma, which are accelerated toward the analyzer entrance by the sheath field. A review of a modern compact RFA design for the measurement of ion energy distribution is given by researchers [17, 18]. The research work

described in this thesis will focus primarily on RFA measurements.

1.4 Ancillary plasma diagnostics

During the course of research work carried out, other plasma diagnostics have also been used to aid the RFA measurements and are briefly summarized here.

1.4.1 Langmuir probe

The Langmuir is a conducting wire placed inside the plasma with a variable bias, V applied. The current I, is measured as a function of V. This is called the I-V characteristic and it has three regions; the electron collection region, the electron retardation region, and the ion collection region. Various plasma parameters can be deduced from this I-V characteristic. In the I-V curve, the point where ion collection current equals electron retarding current, or more precisely, the point at which the curve crosses the V axis, is called the floating potential (V_f). This is the potential at which an isolated object, will float when placed in the plasma. The knee of electron collection region or more precisely, the cross point between electron retardation and electron collection region is called the plasma potential (V_p). The plasma potential is the potential of the space the plasma occupies. Above V_p we enter the electron collection region. It is possible to calculate the electron density (N_e) from the magnitude of the current at the plasma potential. The ion density (N_i) is determined from the ion current in the ion collection region. The electron temperature (kT_e), is determined from the rate at which the electron current falls in the electron retarding region. Finally the electron energy distribution

function (EEDF), can be obtained from the second derivative of the I-V characteristic with zero energy at the plasma potential.

1.4.2 VI probe

The VI probe consists of an inductive pickup to measure the rf current and a capacitance to measure the rf voltage. From the measured values of current and voltage, the phase of a single fundamental frequency and its harmonics, as well as the power being delivered from the generator to the reactor can be worked out. It sits in line between the match unit and the plasma chamber transmission line for the real time monitoring of the voltage, current, phase and actual rf power transferred to the plasma reactor to map the state of the plasma.

1.5 Motivation and thesis structure

Knowledge of ion related parameters at the substrate surface is crucial when tight control over the process is desired. As compared to other diagnostics described in previous section, the RFA sensor provides measurement of ion related parameters exactly at the location of the substrate's surface. RFA technology is easy, small sized, low cost, has reliable diagnostics, and suits almost any plasma processing system. The motivation for the research work presented in this thesis is to develop various designs, methods and techniques based on planar RFA for the measurement of ion related parameters, mainly spatial profile of ion energy and ion flux, ion angular distribution and ionized flux fraction at the substrate surface. The developed design and techniques are tested in various plasma discharges for their validity. Techniques described in this

thesis add important functionality to the existing RFA technology, and will help advance the nano-manufacturing industries.

Chapter 2 describes the constructional and operational details of a compact sized RFA which can be placed on a grounded, floating and rf biased electrode without the need for any modification to the electrode structure. A study is presented to determine sensor to sensor variability in terms of measured ion parameters under similar plasma conditions in a capacitively-coupled plasma reactor.

Chapter 3 describes a multi-sensor design of spatially resolved planar RFA which is capable of measuring the spatial uniformity of the ion energy and ion flux across the surface of a semiconductor wafer. The design consists of thirteen individual, compact-sized, analyzers, all of which are multiplexed and controlled by a single acquisition unit. Without the need for any modification to the electrode structure, this device can be placed directly on top of the biased or unbiased electrode, at the wafer location. The ion energy distribution, average ion energy and average ion flux are measured at the thirteen locations over the surface of the powered electrode to determine the degree of spatial nonuniformity in an industrial capacitively-coupled plasma reactor.

Chapter 4 describes a novel concept of angle resolved planar RFA which can measure the angular distribution of plasma ions bombarding the substrate surface. The technique involves discrimination of ions with different angular spread by varying the aperture depth. By varying the effective aspect ratio (depth/width) of the analyzer's aperture, ions with different angular spread that are allowed through the device for detection are controlled. The analytical theory developed to define the ion current as a function of incident ion angle, ion energy, aperture geometry

18

and aspect ratio is presented. The method used to vary the effective aspect ratio of the aperture is discussed. The mathematical theory is derived and the numerical solution is also discussed. Effect of grid potentials on the angular movement of ions inside a retarding field analyzer is studied through a model made in a charged particle simulator SIMION and a set of simulations are conducted by injecting a cluster of ions at varying incidence angles from the aperture surface and collected them at the collector plate to determine resultant ion current. Simulation results were used to compare with calculated values from the analytical theory derived. The analytical theory and derivative method with minor constructional modification in the sensor design are used to investigate the angle distribution of argon ions in a capacitively coupled plasma (CCP) reactor.

Chapter 5 describes a unified design of RFA with an embedded quartz crystal microbalance, which is capable of measuring deposition rate, ionized flux fraction, and ion energy distribution arriving at the substrate location. The unified design does not require water cooling since a novel calibration method utilising a reference crystal is implemented to compensate for temperature effects in the quartz crystal. The deposition rate, ionization fraction and energy distribution of copper ions arriving at the substrate location are investigated in an asymmetric bipolar pulsed dc magnetron sputtering reactor under grounded, floating and rf biased conditions.

Conclusions and scope for further work are given in Chapter 6.

19

CHAPTER 2

The Retarding field analyzer

A Retarding field analyzer (RFA) is a diagnostic instrument that is used
to measure the energy distribution of ions arriving at a substrate surface
in a plasma discharge. RFA sensors have been used in a great extent
by a number of researchers [17–29] to characterize a variety of plasma
discharges in last few decades. Modern planar RFA's are compact in
size and easy to install in process chambers without any need to modify
system design and structure. Owing to their compact design they suits
almost any plasma processing system. A planar gridded RFA with a
compact cylindrical geometry consists of a current collector shielded from
the plasma by a series of biased grids. Four grids are typically used in
a RFA, of which the first grid is floated at the electrode potential to
reduce plasma perturbation, the second grid is negatively biased to repel
electrons, a potential sweep is applied to the third grid (discriminator) to

present a gradually increasing retarding field to the incoming ions, and the fourth grid is negatively biased with respect to the collector to repel secondary electrons. Collected ions at the collector plate comprises the net ion current, which is measured as a function of discriminator grid potential and then differentiating this current potential characteristic, the integrated form of ion energy distribution (IED) is obtained. The diagram of the design which provides an illustration of the RFA concept is shown in figure 2.1.

2.1 Theoretical background

In a plasma discharge, if $f(u)$ is a velocity distribution of the ions in a three dimensional velocity space, where $u = (u_x, u_y, u_z)$ being the velocity vector in cartesian coordinates. In the case of an almost perfectly anisotropic velocity distribution with respect to the z orientation (parallel to the surface normal of the analyzer plane), both the x and y component of $f(u)$ may be eliminated by considering them as the equivalent of Dirac delta functions. Then, partial integration over all u_x and u_y reduces $f(u)$ to a one-dimensional velocity distribution $f(u_z)$. For the sake of simplicity, since $u_x = u_y = 0$, the z component of the velocity vector u_z, can be referred to as u. $f(u)$ can be related to the ion density (n) as

$$n = \int_0^\infty f(u)du \tag{2.1}$$

By definition,
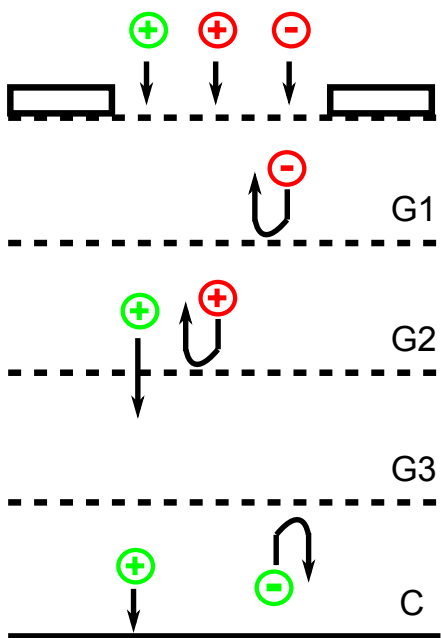
$$f(u)du = dn = g(E)dE \tag{2.2}$$

Figure 2.1: *Diagram of a retarding field analyzer illustrating the effect of grid biasing.*

where $g(E)$ designates the ion energy distribution. Since

$$E = \frac{1}{2}mu^2 \qquad (2.3)$$

and

$$dE = mu \ du \qquad (2.4)$$

where m is ion mass. Using (2.2) and (2.4) we can put

$$f(u) = mu \ g(E) \qquad (2.5)$$

If a RFA sensor is placed on the electrode surface inside the plasma reactor having it's axis parallel to the normal of electrode surface plane. Plasma species will enter the analyzer through the aperture. After the repellor grid has screened out the electrons, the total ion current that can get over the potential barrier (V), produced by the discriminator grid, reaching the collector plate is given by

$$I = neA \int_{u_{min}}^{\infty} uf(u)du \qquad (2.6)$$

where e is elementary charge, A is collecting area and u_{min} is minimum velocity to overcome the potential barrier. The kinetic energy of ions reaching the collector can be given by

$$\frac{1}{2}mu^2 = eV \qquad (2.7)$$

Now taking the derivative of (2.6) with respect to discriminator grid potential and simplifying,

$$\frac{dI}{dV} = neA \ \frac{d}{dV} \int_{u_{min}}^{\infty} uf(u) \ \frac{du}{dV} \ dV = -neA \ uf(u) \ \frac{du}{dV}|_{u=u_{min}}$$

substituting the value of u from (2.7)

$$\frac{dI}{dV} = -neA \ uf(u) \ \frac{d(\sqrt{\frac{2eV}{m}})}{dV}|_{u=u_{min}} = -neA \ uf(u) \ \frac{e}{mu}$$

therefore

$$\frac{dI}{dV} = -\frac{ne^2 A}{m} \, f(u) \qquad (2.8)$$

from (2.5), (2.7) and (2.8)

$$\frac{dI}{dV} = -ne^2 A \, \sqrt{\frac{2eV}{m}} \, g(E) \qquad (2.9)$$

We thus see that the derivative of the collector current with respect to discriminator grid potential can be used to obtain the ion velocity and ion energy distribution functions [28, 30].

2.2 Sensor geometry and components

The planar RFA consists of plane parallel grids for electron rejection, ion energy selection, secondary electron suppression and an ion collector. Electrically insulating spacers isolate all the grids and collector. All these components are assembled in a metallic housing having a series of holes on the front surface to allow ions enter the device. The whole assembly is closed by a 1 mm thick metallic lid. While designing and building an RFA, there are a number of constraints which needs to be considered.

2.2.1 Grid/Mesh material

The mesh material selection is critical to address several plasma environmental concerns. One obvious requirement of the mesh material is high electrical conductivity. Sputter yield of the material needs to be low enough to provide sufficient resistance to sputtering, especially for the top grid. Thermal expansion coefficient should be low to prevent any change in transparency due to temperature increase. The mesh material should have sufficiently large thermal conductivity in order to prevent

sagging of the grid which would distort grid electrode areas and conse-
quently the electric field.

2.2.2 Grid/Mesh Size

The size of the mesh that makes up the grids of the RFA is determined
by the Debye length. The individual wires in the mesh must be closer to-
gether than the Debye length in order to adequately discriminate against
the particles of the plasma. If the spacing is too large, particles will pass
through the grid due to a dimple of low potential at the center of each
cell. However, if the mesh size is too small, the number of particles that
can pass through is reduced due to an increase in surface area and which
will result in lower levels of signal detected at the collector. It is known
[31] that the potential tends to "sag" between the grid wires, presenting
a nonuniform retarding potential. Particles can pass through due to the
unevenness of the potential field, causing inaccuracies in the measured
current. The largest deviation from the retarding potential (V_r) occurs
midway between the grid wires (at the center of each cell) and is given
by (2.10) [32]

$$\frac{\Delta V_r}{V_r} = 1 - \frac{2\pi(d/a) - \ln 4}{2\pi(d/a) - 2\ln[2sin(\pi r/a)]} \tag{2.10}$$

where r is the radius of the grid wires, a is the length of each cell in the
grid and d is the grid-to-grid spacing.

2.2.3 Spacing between grid-to-grid

Ideally, the grids are spaced according to (2.11) [33].

$$d = 1.02\lambda_d(\frac{eV}{k_BT_e})^{3/4} \tag{2.11}$$

where d is the spacing, λ_d is the Debye length($\lambda_d = \sqrt{\epsilon_0 k_B T / n e^2}$), V is voltage difference between two grids and T_e is electron temperature.

Practically, in order to minimize space charge and collisional effects, the spacing between the grids must be smaller than the approximation given in (2.11).

2.2.4 Spacing between front surface to collector

At a given chamber pressure the ion mean free path(λ) is given by

$$\lambda = \frac{1}{n_g \sigma} \tag{2.12}$$

where n_g is number density and σ is momentum transfer collision cross section between ions and neutrals.

The total distance an ion travel inside the analyzer before being collected should be less than the ion mean free path in order to avoid collisions which can distort the real IED. At gas pressures of around 50 mTorr, the mean free path is approximately 1.2 mm. Therefore at 50 mTorr, the total spacing between front surface to the collector should be less than 1.2 mm.

2.2.5 Electrically insulating spacer

The spacer material used to isolate grids should be reliable for a wide range of operating voltages and temperatures in terms of their related leak current and out-gassing properties. The spacer material should be flexible enough to be machined to desired shape and size and should have extremely low conductivity and high dielectric strength to effectively isolate the grids.

2.3 Sensor description

2.3.1 Constructional and operational details

Considering all the constraints listed above, a number of compact RFA sensors similar to as reported by researchers [18, 34, 35] are constructed. Each analyzer is assembled in aluminium housing and all the components are built using high precision manufacturing techniques having minimal manufacturing variations to ensure high level of repeatability of each sensor.

The constructed sensors have a set of four grids which are stacked between the entrance orifice and the collector plate (C). Each grid is made from nickel with square shaped windowpane aperture structure having a side length of 20 μm and 50% transmission. Flat washers of mica in the shape of a flat disc with a centrally located hole are employed as spacers between the grids. The entrance orifice faces the plasma and allows a sample of the ions, arriving through the sheath, into the RFA for analysis. The sensor allows only those ions with sufficient energy to overcome the retarding potential to reach the collector. The schematic of the RFA design and internal potential diagram are sketched in figure 2.2. The schematic shows only one ion entrance orifice for simplicity but actually there is an array of 800 μm diameter orifices with a sampling area of approximately 20 mm^2 which maintains a measurable ion flux to the analyzer. The first grid G_0 is electrically connected to the chassis so as to keep it floating at the electrode potential to reduce plasma perturbation. Grid G_0 with 20 μm aperture size covers the plasma facing orifices from the back side and so reduces the sampling area open to the plasma. This grid ensures that the diameter of the open area, seen by the plasma, is less

Figure 2.2: *(a) Schematic of the RFA structure and (b) RFA potential configuration for ion discrimination.*

than the Debye length and prevents plasma extending inside the device and also minimizes any disturbance to the sheath electric field. A second grid G_1 is biased negatively ($-60V$) to repel plasma electrons that enter the analyzer. A third grid G_2 is biased with a positive potential sweep, from the dc potential of G_1 (corresponding to zero retarding potential) to about $20V$ above the dc plasma potential which covers the entire range of energies that the ions may have. The potential sweep at G_2 creates a retarding electric field to discriminate ions based on their energy. A fourth grid G_3 is biased slightly more negative ($-70V$) than C, creating a retarding potential for secondary electrons that can be emitted from the surface of C due to impact of energetic ions. Thus the secondary electrons get immediately reflected back to C and the true IV characteristic can be measured. The collector, C, is biased with the same negative potential as G_1 and used to collect and record the ion current as a function of discriminator potential. The spacings between the grids are optimized to minimize collisional and space charge effects and set at 200 μm so as to have a total distance of 0.8 mm between sampling orifice and the collector. This distance is smaller than the mean free path of ions at typical chamber pressures of up to 100 mTorr. This compact and shallow structure provides greater operating pressure range, up to approximately 100 mTorr, without the need of any differential pumping. The electrical connections to the grids and collector plate are made with gold plated spring contacts. A fully assembled analyzer is 3 mm thick with 33 mm diameter and 1 mm deep. This simple construction offers versatility, robustness and compactness. A picture of the constructed RFA sensor is shown in figure 2.3 [36].

The analyzer is enabled to be placed on grounded, floating, dc bi-
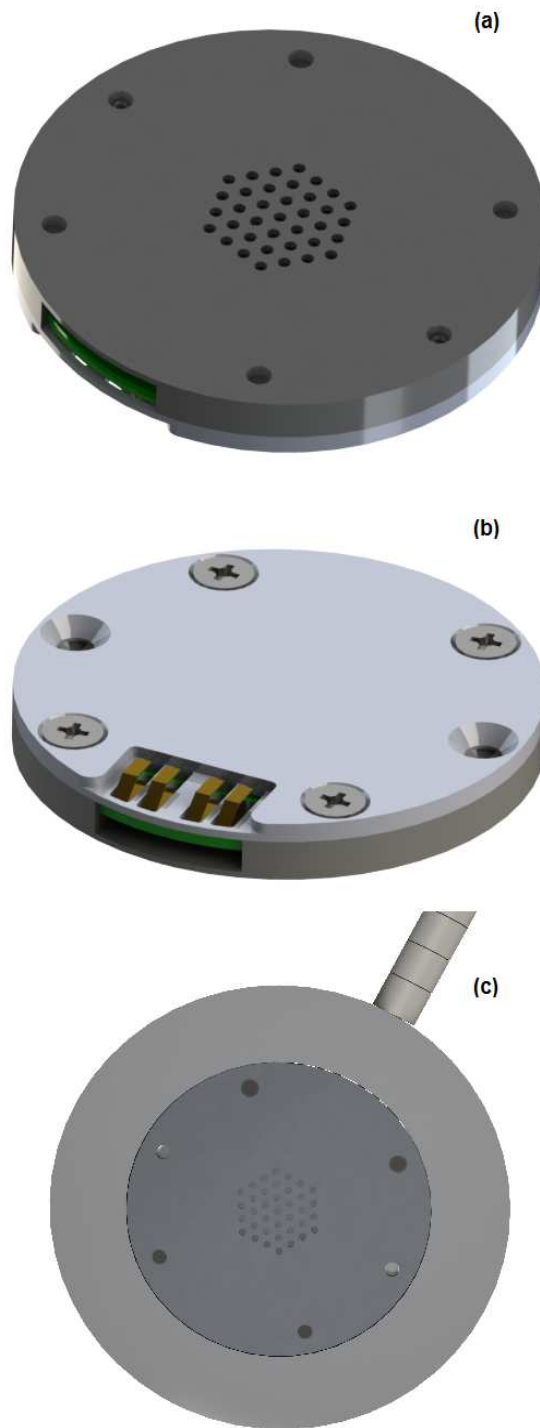
Figure 2.3: *(a) Plasma facing front surface of the RFA sensor and (b) Back surface with gold plated spring contacts. (c) RFA sensor embedded in to the holder*

ased or rf biased electrodes by employing low pass filters with high input impedance having inductor - resistor - capacitor (LRC) configuration, placed between each grid and collector and the RFA electronics. When electrode is rf biased, these filters allows the rf potential at the electrode/analyzer-body to be almost fully coupled (capacitively) to the grids and collector, since the filter input impedance is chosen to be significantly greater (at the frequencies of interest) than electrode impedance to ground and the impedance associated with inter-grid capacitance ($\sim$ 100 pF). The filters also have greater than 60 dB of attenuation at the output over the frequency range (500 kHz - 40 MHz), preventing any significant rf current reaching the measurement electronics. This range covers some of the most common frequencies used in low temperature rf plasma processes. High input impedance ensures that there is no significant loading of the electrode impedance and that there is a negligible difference between the rf bias applied to the electrode and the rf bias coupled to the grids. The measured input impedance and attenuation offered by the filters are shown in figure 2.4 [18].

2.3.2 System hardware and electronics

The complete RFA system [36] consists of three major hardware components: sensor with the cabling, vacuum feedthrough with electronic circuitry and data acquisition control box. A block diagram of the major components of the system electronics is shown in figure 2.5.

A 50 mm diameter mounting plate with electrical contacts and integrated cable bundle holds the RFA sensor. The cable bundle is 650 mm long and contains the lines for the individual grid and collector biasing extending from the sensor and is terminated with a plug con-
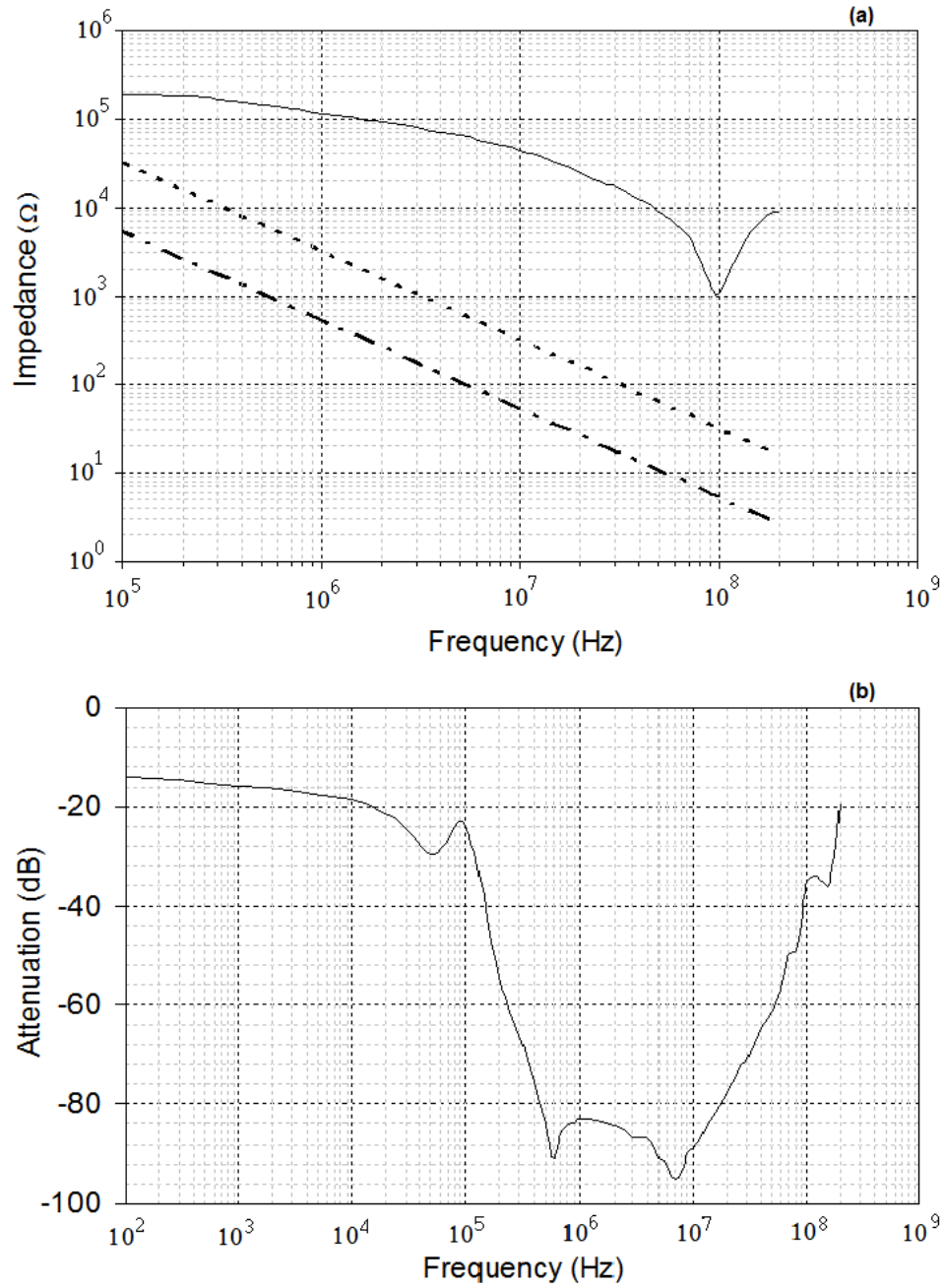
Figure 2.4: *(a)Filter input impedance (solid line), electrode impedance to ground (dashed line), and grid impedance to casing (dot-dashed line) and (b) output attenuation as a function of frequency.*
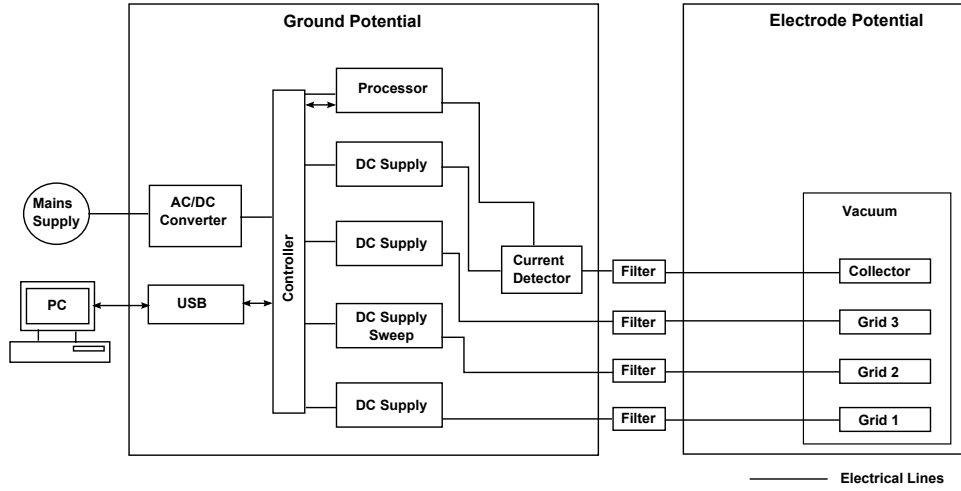
Figure 2.5: *Block diagram of the system electronics and the data acquisition setup.*

nector which mates to the vacuum feedthrough at the reactor wall. The vacuum feedthrough forms the interface between the vacuum and the atmosphere. The atmospheric side of the feedthrough has an integrated enclosure which encases the collector current measurement circuitry. The front end of the circuitry is isolated from ground and floats at the electrode bias potential. The back end of this circuitry is at ground potential. A strong isolation barrier separates the two sides. The collector current passes from the floating side to the ground side through the high impedance low pass filters before being measured and digitised on the data acquisition unit.

The data acquisition unit is powered from the mains supply and communicates with the host personal computer (PC) via universal serial bus (USB) connection. It houses four independent dc power supplies which deliver the required potentials to the RFA grids. The power supplies are bipolar with a range of ± 2.5 kV and whose outputs are configured by the user through the main controller board. The on-board processor receives

the current data from the feedthrough. The data is processed and sent to the host PC for further analysis and graphical display.

2.3.3 Sensor resolution and sensitivity

According to Bohm and Perrin [28], the resolution of analyzer depends on the deviation of incoming ions from their original trajectories parallel to the analyzer's axis before being filtered by the discriminator grid. Any deviation from this direction results in a decrease δE of the component of the ion kinetic energy E oriented parallel to the analyzer's axis. The ratio $\delta E/E$ is defined as the analyzer resolution. It is a function of the initial ion kinetic energy, of the potential distribution between the grids, and of many other factors such as (i) the inter-grid distance, (ii) the design of the sampling orifice, and (iii) the mesh size.

Sakai and Katsumata [37] defined the resolution in terms of the diameter of mesh wire (d), the spacing between mesh wires (s) and the distance between grids (l). They have proposed that energy resolution ($\delta E/E$) $\sim s/l$, which is applicable in a range $0.1 \leq d/s \leq 1$. This suggests that the larger the l, the better the resolution. However, the absence of differential pumping puts an upper limit on l to minimize the effects of ion collisions inside the analyzer.

Conway *et al* [38] built a four gridded analyzer having 23 μm spacing between mesh wires and 0.9 mm distance between repellor to discriminator grids while separation between other grids was 0.4 mm. They have demonstrated that the repellor to discriminator distance was the primarily factor affecting the resolution. For their design the energy resolution was theoretically calculated to be 0.2 eV. Our analyzer have similar and more compact design, the spacing between mesh wires is 20 μm while

distance between repellor to discriminator is only 0.2 mm, therefore we expect the resolution to be better than 1 eV.

In order to determine sensitivity of this sensor while measuring IED in different ion energy regimes, an experiment is conducted in a symmetric rf driven capacitively coupled reactor. Argon is used as the working gas and chamber pressure is maintained at 1 Pa. A rf power of 40 W at 13.56 MHz is applied to the top electrode through an automatic matching unit and the sensor is placed on the bottom electrode. The bottom electrode is dc biased in a range from -30 V to +20 V to change the bombardment energy of the ions. The IED and ion flux measurements are shown in figure 2.6 When bottom electrode is biased with a dc voltage of -30 V, the IED shows a peak around 46 eV and the ion flux (which is the area under the IED curve) is measured to be 0.07 A/m^2. The IED peak shifts towards low energies as we decrease the negative dc bias but the ion flux remain almost same. When electrode is biased positively at +20 V, the electrode potential approaches towards plasma potential and IED shows a peak around 6 eV. In this low energy regime, the ion flux is lower by a factor of 20-25%. There does not appear to be any significant loss in sensitivity at lower energies since the well defined single peak structure is still visible and the full width at half maximum remains constant. The increase in ion flux at large negative bias is to be expected since the electrode is now biased in to the ion saturation region. The increase of the sheath voltage causes an increase of the sheath width and any departure from precisely planar sheath geometry will cause an effective increase in the ion flux collected.
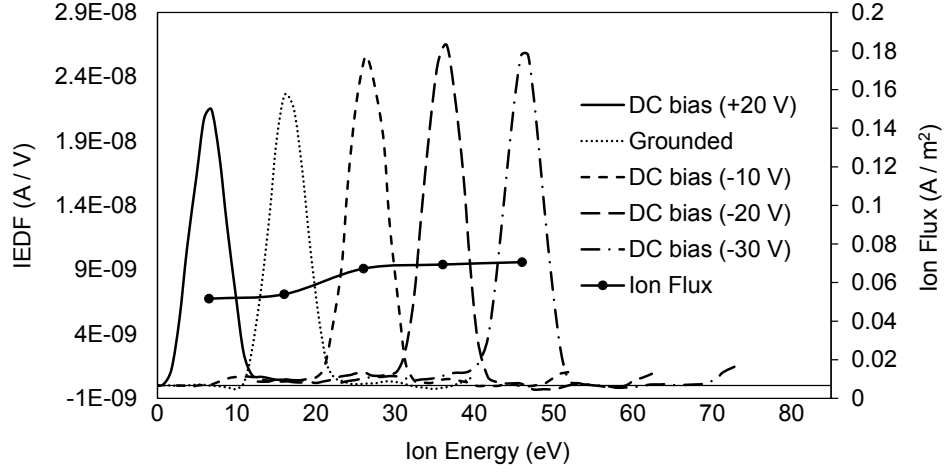
Figure 2.6: *IED and Ion flux at different substrate dc biasing.*

2.3.4 Sensor calibration

The sensor needs to be calibrated to accurately determine the ion flux reaching to the substrate surface. The calibrated average ion flux J_i to the surface on which the sensor is mounted is estimated from

$$J_i = \frac{\int_{E_{min}}^{E_{max}} f(E)dE}{AT} \tag{2.13}$$

where E_{max} and E_{min} are maximum and minimum ion energies, f(E) is IED, A is the ion collection area and T is the combined transmission of the RFA grids.

The collection area is given by the area of the orifice which consists of 37 circular holes each of diameter 800 μm:

$$A = 37\text{x}\pi r^2 = 1.86\text{x}10^{-5}m^2 \tag{2.14}$$

The transmission of each of the 4 grids is 50 % and so:

$$T = (\frac{1}{2})^4 = 0.0625 \tag{2.15}$$

36

Therefore the integration of IED is scaled by a scaling factor $1/AT$ in order to calculate the absolute ion flux received at the substrate surface.

The average ion energy $< E >$ is estimated from

$$< E >= \frac{\int_{E_{min}}^{E_{max}} E f(E) dE}{\int_{E_{min}}^{E_{max}} f(E) dE} \qquad (2.16)$$

The integration is performed using the trapezoidal approximation:

$$\int_{E_{min}}^{E_{max}} f(E) dE = \frac{1}{2} \sum_{i=1}^{n} (y_i + y_{i-1})(x_i - x_{i-1}) \qquad (2.17)$$

where x_i and y_i are the data points of the IED and n is the number of points.

2.4 Sample measurements

Sample measurements were taken by placing the RFA sensor at the bottom electrode of a symmetric rf driven capacitively coupled plasma (CCP) reactor. Argon was used as the working gas and chamber pressure was maintained at 1 Pa. A rf power of 50 W at 13.56 MHz was coupled to one of the electrodes through an automatic matching unit and the other electrode was grounded. In figure 2.7 the I-V and IED data curves are shown when (a) Top electrode was powered and bottom electrode was grounded, (b) Top electrode was grounded and bottom electrode was powered. The measurements are reproducible and the standard deviation of the average was calculated as less than 2%.

When bottom electrode is grounded, a dc sheath forms in the vicinity of the electrode. Ions are accelerated from the bulk plasma to the electrode and acquire an energy equal to the dc sheath potential. The measured IED contains a single peak relating to the average energy gained

by the ions traversing the sheath which is as expected. When the bottom electrode is rf biased, a rf modulated sheath in the vicinity of the electrode can be assumed. At 50 W of rf power the bottom electrode attains a self dc bias at around - 440 V which causes the ions to accelerate more and their energy distribution shifts towards higher energies. In this case a bimodal IED is measured, the low energy peak occurs when the electrode potential is closest to the plasma potential at the positive peak of the rf cycle. More number of ions reach the electrode with this energy because the rf potential is varying slower at this stage. As the rf cycle advances the rate of potential variation increases to a maximum (minimum in the IED) then slows again toward the negative peak of the rf cycle. Again, more number of ions now reach the electrode resulting in the high energy peak of the IED. A detailed description of the characteristics of the ion energy distribution is discussed by Gahan *et al* [18, 39, 40]. This test verifies the normal operation of constructed analyzer.

2.5   Sensor to sensor variability

RFA sensors are built using high precision manufacturing techniques to minimize constructional variation between sensor to sensor and achieve high level of repeatability. In order to determine the unit-to-unit variability of individual RFA sensors, experiments were carried out in which random samples of 9 sensors were selected from a total of 13 built. Each sensor was used to measure the ion energy distribution (IED), average ion energy and ion flux at the same location under the same conditions in a test plasma chamber. The sensors were mounted on the lower grounded electrode in a symmetric rf driven CCP reactor one unit at a time. Ca-
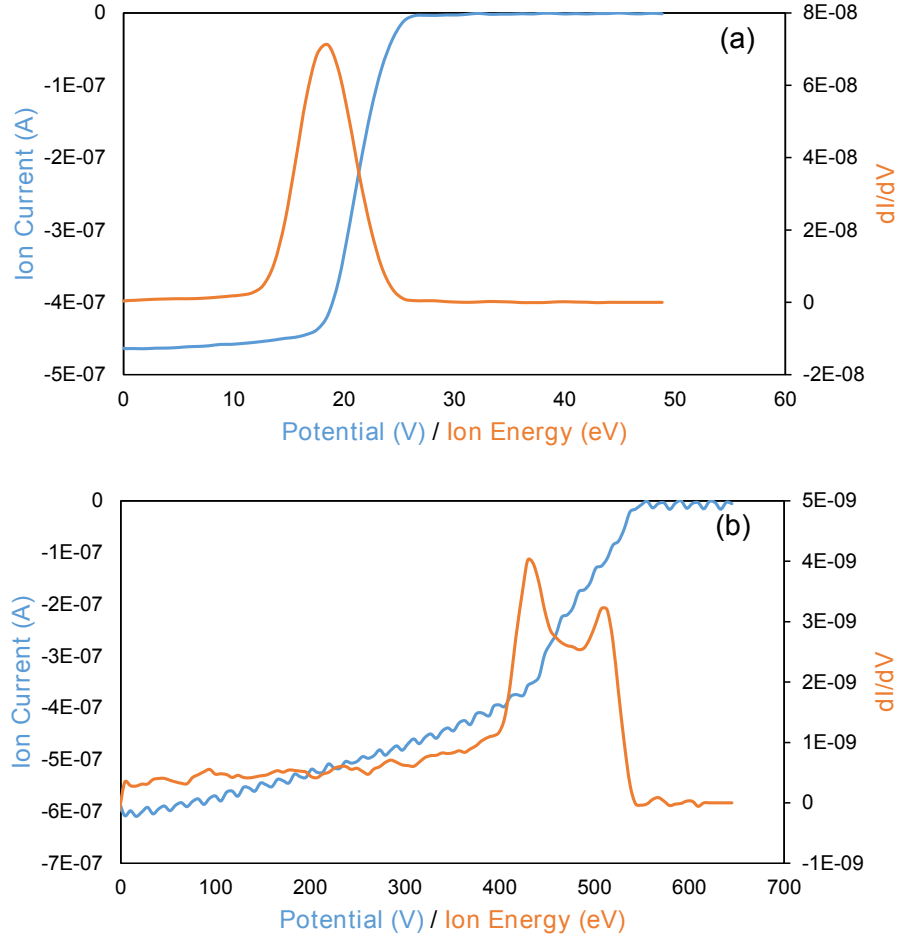
Figure 2.7: *Plot of ion current and IED when bottom electrode is (a) grounded and (b) rf biased.*
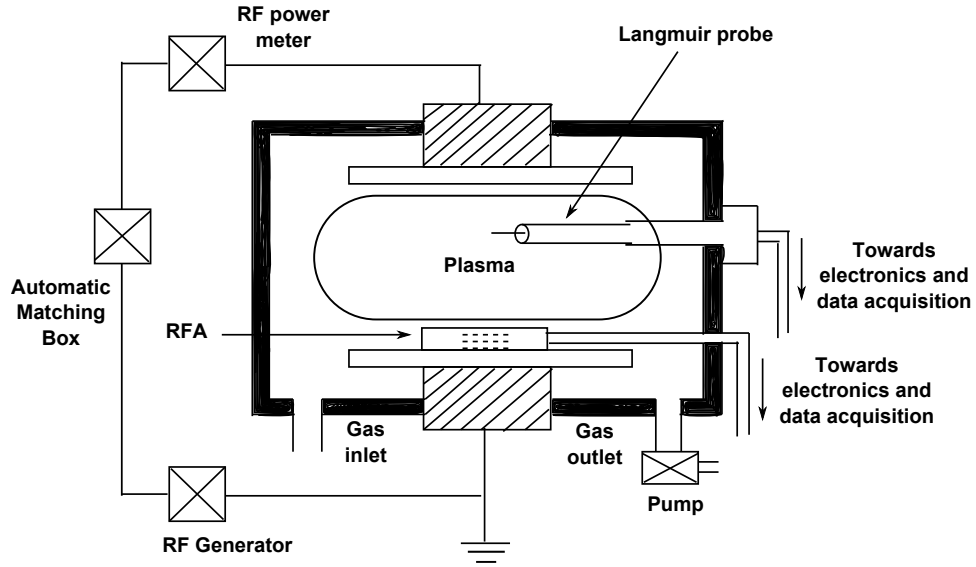
Figure 2.8: *Schematics of the reactor showing mounting of langmuir probe and the RFA sensor.*

bling for the RFA is fed through one of the vacuum ports on the sidewall of the plasma chamber. A commercial VI probe Octiv-Suite [41] was installed between the automatic match box and the electrode. Octive-Suite was used to measure the exact rf power being delivered to the reactor from the rf generator. A commercial langmuir probe system [42] was also mounted just above the RFA sensor position to measure the plasma electron density. Separate data acquisition units for RFA and langmuir probe are used to record, digitize and transmit the signals to the PC for analysis. The schematics of the set-up and mounting of langmuir probe and RFA sensor inside the reactor is shown in figure 2.8.

Using the VI probe and langmuir probe, similar plasma conditions were maintained every time while testing the individual RFA sensors. To ensure similar plasma conditions the rf power transferring to the reactor was kept at 30 ± 1 W while plasma electron density measured by the
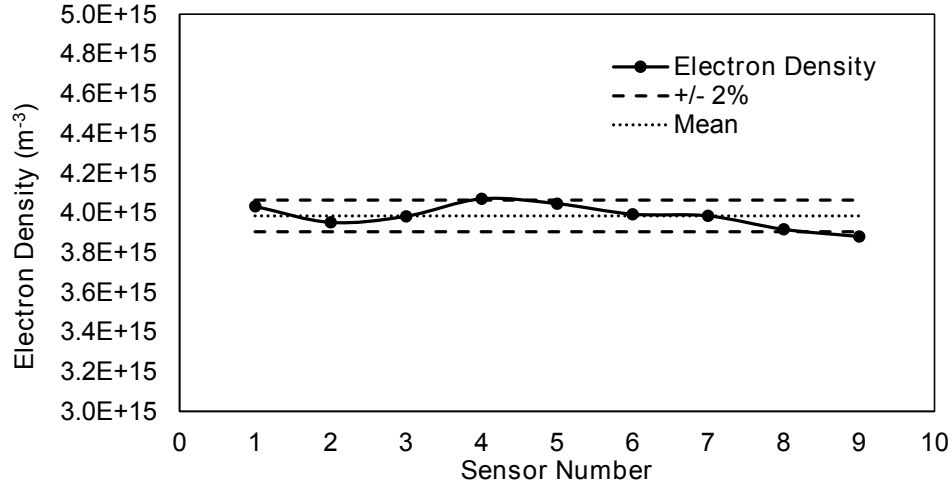
Figure 2.9: *Variation of electron density across the sensors.*

langmuir probe was kept at $3.98 \times 10^{15} m^{-3} \pm 2\%$ as shown in figure 2.9 during each run. The measured I-V curve and ion energy distribution (IED) are shown in figure 2.10 and figure 2.11 respectively for all 9 sensor maintained in similar plasma conditions. Ions show similar energy distribution having a peak around 24 eV for all the sensors tested. From the measured ion energy distributions, average ion flux and average ion energy are calculated to define sensor to sensor variability.

It was found that I-V and IED curves are similar and the total ion signal level in measuring average ion energy and ion flux varied consistently by less than 2% across a set of 9 sensors tested. A representative sample of the measured variation in ion energy and ion flux across 9 sensors is shown in figure 2.12. The measured signal level is controlled by the sampling area of the orifices and the transmission of the set of grids. The use of high precision manufacturing techniques enables the high level of repeatability of each sensor build. Less than 2% manufacturing variation ensures reliable measurement of plasma parameters from unit to unit.
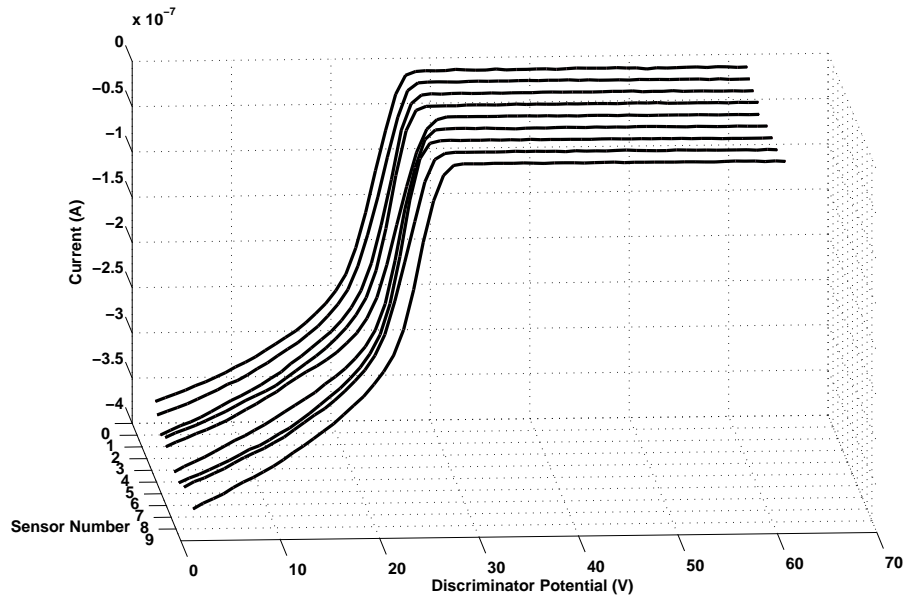
Figure 2.10: *I-V plot for a set of 9 RFA sensors tested.*
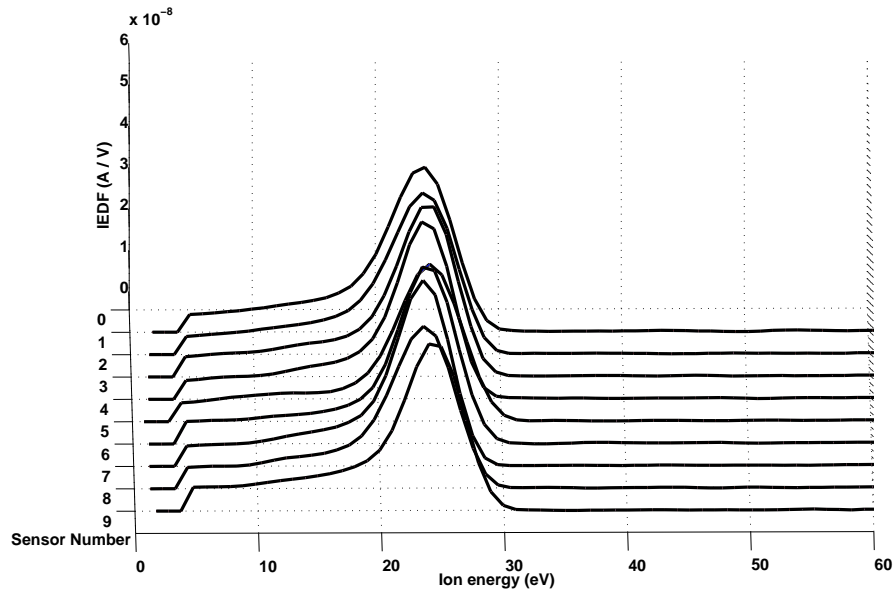
Figure 2.11: *IED plot for a set of 9 RFA sensors tested.*

42
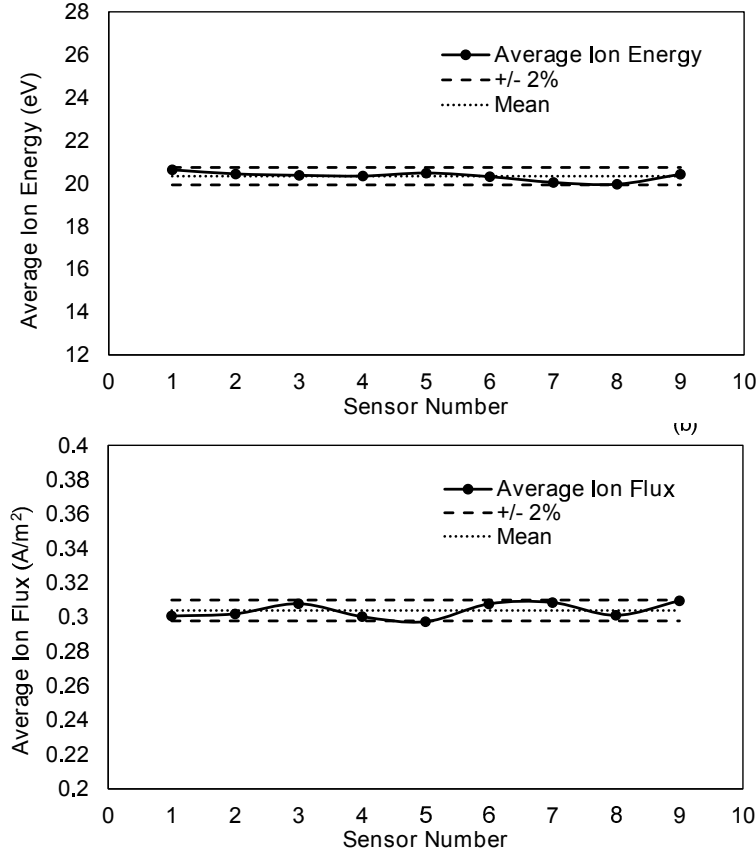
Figure 2.12: *Variation of (a) average ion energy and (b) average ion flux across the sensors at similar plasma conditions.*

In reality much of the statistical variation determined in this manner is likely due to slight difference in plasma conditions after each sensor installation rather than due to the sensors themselves. It gives a "worst case" statistic for the measurement.

2.6   Summary

A detailed constructional and operational description of the RFA system is presented. Major constraints which needs to be considered carefully

while building the RFA sensor have been detailed. By considering important constraints, 13 individual RFA sensors have been assembled having all of their components built with high precision manufacturing techniques. Sensor to sensor variability in terms of ion energy and ion flux measurements have been determined by testing each sensor in similar plasma environment. A variability of less than 2% has been observed which ensures high level of repeatability between the sensors. These sensors have been used to build a multi-sensor design to measure spatial plasma profile which is described in Chapter 3.

A spatially resolved retarding field analyzer design suitable for uniformity analysis

3.1   Introduction

The semiconductor manufacturing industry is being driven by the need to produce integrated circuits (ICs) at lower cost and to improve the performance of these ICs by generating even more transistors on each chip. Larger plasma chambers are required to process larger wafers to reduce the cost of each IC, while more control of the plasma uniformity is required to produce smaller feature sizes. If the plasma is spatially non-uniform, it can lead to differences in etch or deposition rates across the wafer which can consequently impact localized device performance and overall yield [43–45]. Moreover strongly nonuniform plasma over the wafer can give rise to lateral dc currents within a film on the wafer

that can damage the film [46]. Therefore, in order to control the spatial plasma uniformity; detection of variations in plasma parameters across the wafer is of great significance.

The reasons of plasma nonuniformity and its effect on plasma parameters has been studied by a number of researchers [47, 48]. Plasma nonuniformity leads to a local imbalance between electron and ion currents in the plasma. This imbalance in local particle currents in the plasma can lead to issues such as gate charging during plasma etching [49]. The rate at which plasma species impact the wafer surface, specifically, the flux and energy of the ions bombarding the wafer surface determines the process outcome. In an effort to address the need to monitor the spatial uniformity of the ion energy and ion flux across the surface area of the wafer, a multi-sensor design has been developed by using the set of sensors as described in Chapter 2. The principle motivation of this work is to describe this novel muti-sensor RFA design and to demonstrate its capabilities through a series of ion energy and ion flux measurements in a plasma processing reactor. The content of this chapter has been published as a journal article [50].

3.2 Experimental set-up

3.2.1 Capacitively coupled plasma (CCP) reactor

A commercial plasma reactor Oxford Instruments - Plasmalab System 100 [39, 51, 52] reactive ion etcher (RIE) is used in this study. These type of reactors are one of the most common type of industrial plasma sources [46, 53]. The reactor has an asymmetric parallel plate, capacitively coupled, 13.56 MHz rf driven configuration. The system consists of

a 205 mm diameter powered electrode, with wafer clamp, and a grounded electrode (295 mm diameter) with a showerhead configuration to supply the process gases. The electrode separation distance is approximately 45 mm. The top electrode is grounded and has a shower head structure through which the working gas is coupled to the reactor. The rf power in the range of 50-300 W at 13.56 MHz, is coupled to the bottom electrode (known as the rf chuck) which holds the substrate/sensor, through an automatic matching unit. Chiller water is supplied to each electrode for cooling purposes. The plasma extends to the reactor wall as there is no radial confinement of the plasma. The resultant rf potential controls the energy and flux of ion species bombarding the substrate surface during processing [40]. The working gas is argon at a pressure of 20 mTorr for all experiments presented. The schematic of the experimental set up is shown in figure 3.1.

3.2.2   The spatially resolved RFA design

The schematic diagram of the spatially resolved RFA assembly, with 300 mm diameter, is shown in figure 3.2. The multi-sensor design [54] has 13 RFA systems mounted on a 300 mm diameter disk. All the 13 sensors used to build the multi-sensor design have less than 2% manufacturing variability as described in Chapter 2, to ensure reliable measurement of plasma parameters from unit to unit. The multi-sensor design is placed upon the lower RF powered electrode (with diameter of 205 mm) as shown in figure 3.1. The comparatively larger size of RFA assembly than the electrode might impact the plasma properties but it must be emphasized that the purpose of this experiment is to demonstrate the capabilities of the sensor design and not to study the complete plasma
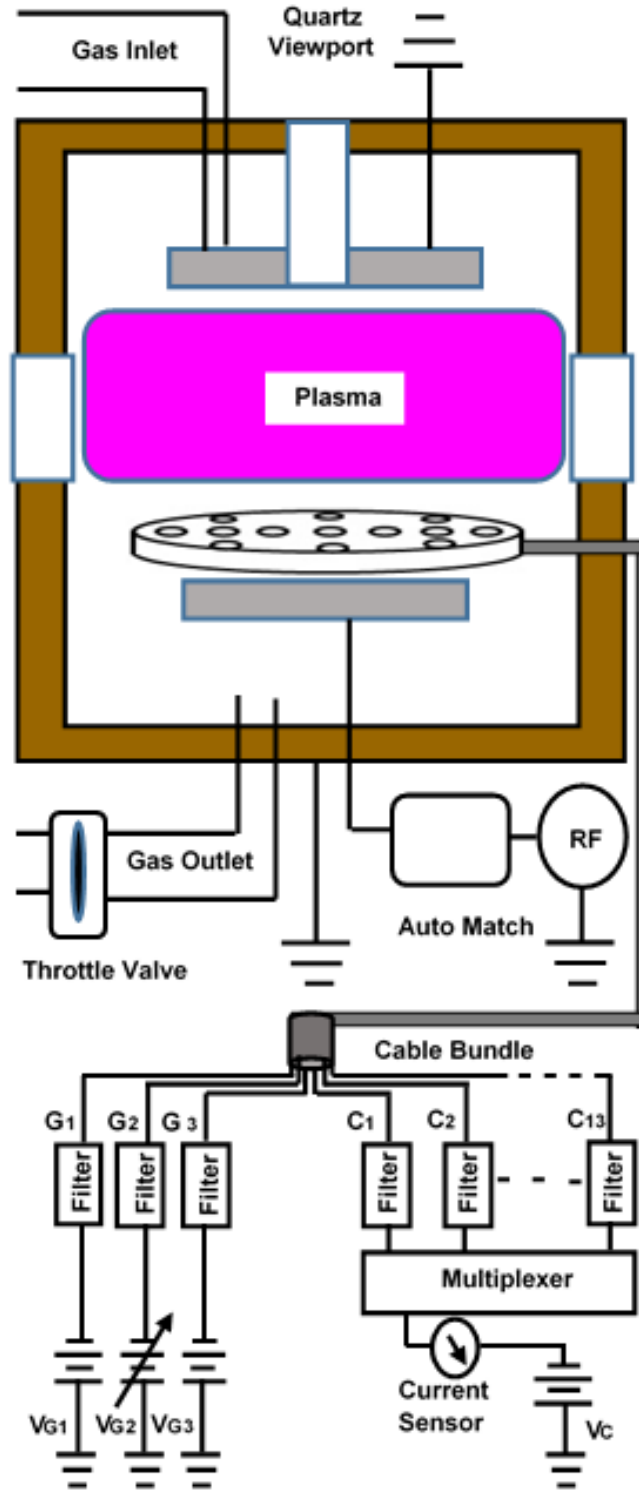
Figure 3.1: *Schematic of the experimental set up. The multi-sensor RFA device is mounted on the bottom, rf biased, electrode.*
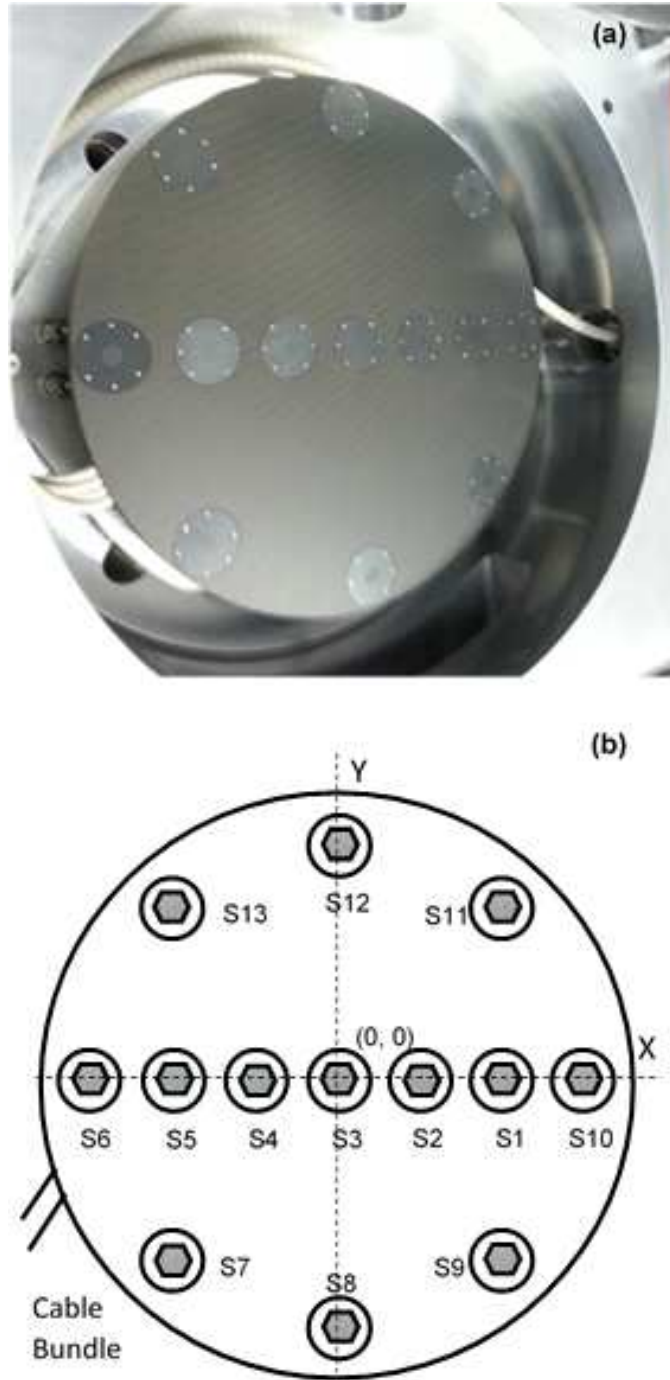
Figure 3.2: *(a) Photograph and (b) Schematic of the spatially resolved RFA assembly.*

discharge characteristics. Cabling through which signals are taken out from the RFA assembly is fed through one of the vacuum ports on the sidewall of the plasma chamber using a vacuum feedthrough where rf filtering and signal multiplexing is carried out. The signals from the 13 sensors are recorded sequentially using multiplexer circuitry. A data acquisition unit is used to record, digitize and transmit the signals to the PC for display and further analysis. This RFA assembly provides the user with a means of measuring the ion energy distribution and ion flux at thirteen different locations across the surface of a wafer and therefore provides a spatial map of these critical parameters.

3.2.3 Filtering, multiplexing and electronics

The cable bundle, which carries the signals to/from the RFA grids, is connected to a vacuum feedthrough mounted at the reactor wall. The rf filters, as described in Chapter 2, which enable the sensor to float at the rf bias potential, are located here. The cables, sealed in a flexible ceramic shield, are resistant to discharge temperature and reactive species present in the process under investigation. The cables enter the vacuum feedthrough where they are passed through low pass rf filters. After filtering, the collector lines are multiplexed (with help of a thirteen-to-one stage analog multiplexer), sampled and digitized using a 16 bit analogue to digital converter.

The data acquisition unit has four output voltage channels with a range of -1.5 kV to +1.5 kV. Three of these are set to a constant output level to bias the collector plate (C), plasma electron repelling grid (G_1) and secondary electron suppression grid (G_3). The fourth voltage channel sweeps the discriminator grid (G_2) from the sensor floating potential to

a large positive potential to cover the range of all possible energies that ions crossing the sheath may have. The collector current is plotted as a function of G_2 potential for each sensor. Data are transferred from the measurement electronics to the computer for the analysis through a universal serial bus (USB) connection.

3.3   Results and discussion

The spatially resolved RFA assembly has been used to measure the ion flux and IED at different locations across the wafer holder to determine the spatial profile of these plasma parameters. The CCP discharge pressure is maintained at 20 mTorr in Argon gas and RF power has been varied in the range of 50-300 W.

3.3.1   Ion energy distribution (IED's)

Measured IED's at thirteen different locations across the wafer holder at 300 W are shown in figure 3.3. A minor variation in IED shapes is readily seen across the wafer. The measured IED's can be compared with each other to define the degree of spatial non-uniformity. Variation of measured IED's at different discharge powers at the position of sensor one shows that the peak separation (which is a function of the magnitude of the rf bias) and the area under the IED curve (which is a function of the magnitude of the ion flux) both increase with increasing power. This behavior confirms normal plasma characteristics of a CCP discharge in which both the ion energy and flux are controlled by applied rf power.
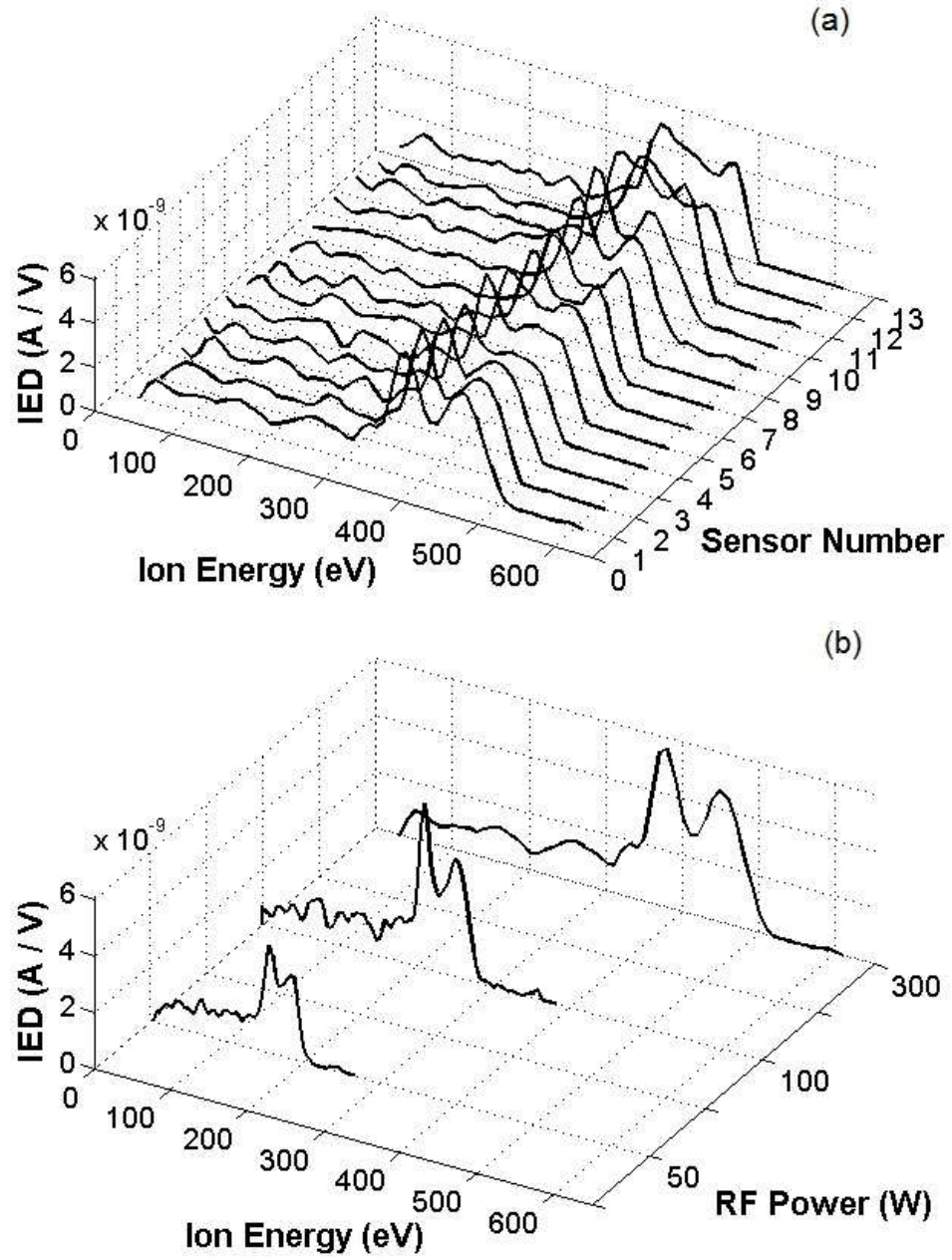
Figure 3.3: *(a) IED's measured at 13 different locations across the wafer and (b) variation of measured IEDs received at the position of sensor one with discharge power.*
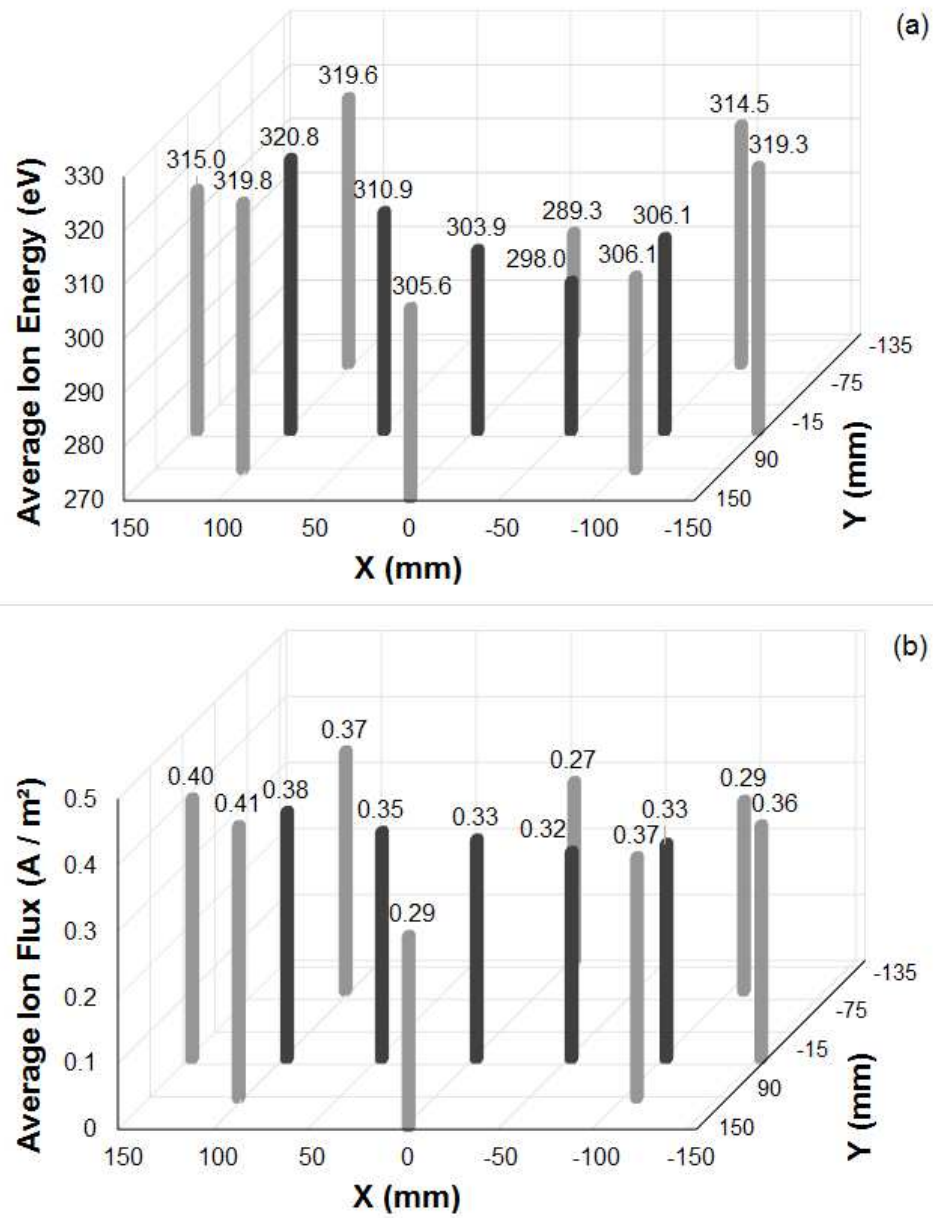
Figure 3.4: *(a) Average ion energy and (b) ion flux at 13 different locations across the wafer.*

3.3.2 Average ion energy and flux

The average ion energy $< E >$ and ion flux J_i are calculated using the expressions (2.16) and (2.13) respectively as given in Chapter 2. In figure 3.4, the magnitudes of the average ion energy and ion flux at thirteen different specified locations across the wafer at a discharge power of 300 W are shown. It is evident from the graph that average ion energy at different points on the wafer displays a non-uniformity of 5.1% which is calculated using the following formula

$$Non - uniformity = \frac{Maximum\,Value - Minimum\,Value}{Maximum\,Value + Minimum\,Value} \quad (3.1)$$

A similar variation is observed in the average ion flux at different parts of the wafer surface. Non-uniformity in average ion flux is found to be 20.2%.

3.3.3 Ion energy and flux as a function of discharge power

In figure 3.5, the variation of ion energy and flux across the wafer at different discharge powers is shown. It is evident from the graph that spatial variance of ion energy and flux increases with increase in discharge power however relative uniformity is similar.

The spatial variance of plasma parameters measured across the wafer is extremely important for plasma processing. Using this spatially resolved RFA device the degree of spatial nonuniformity in the plasma parameters can be monitored.
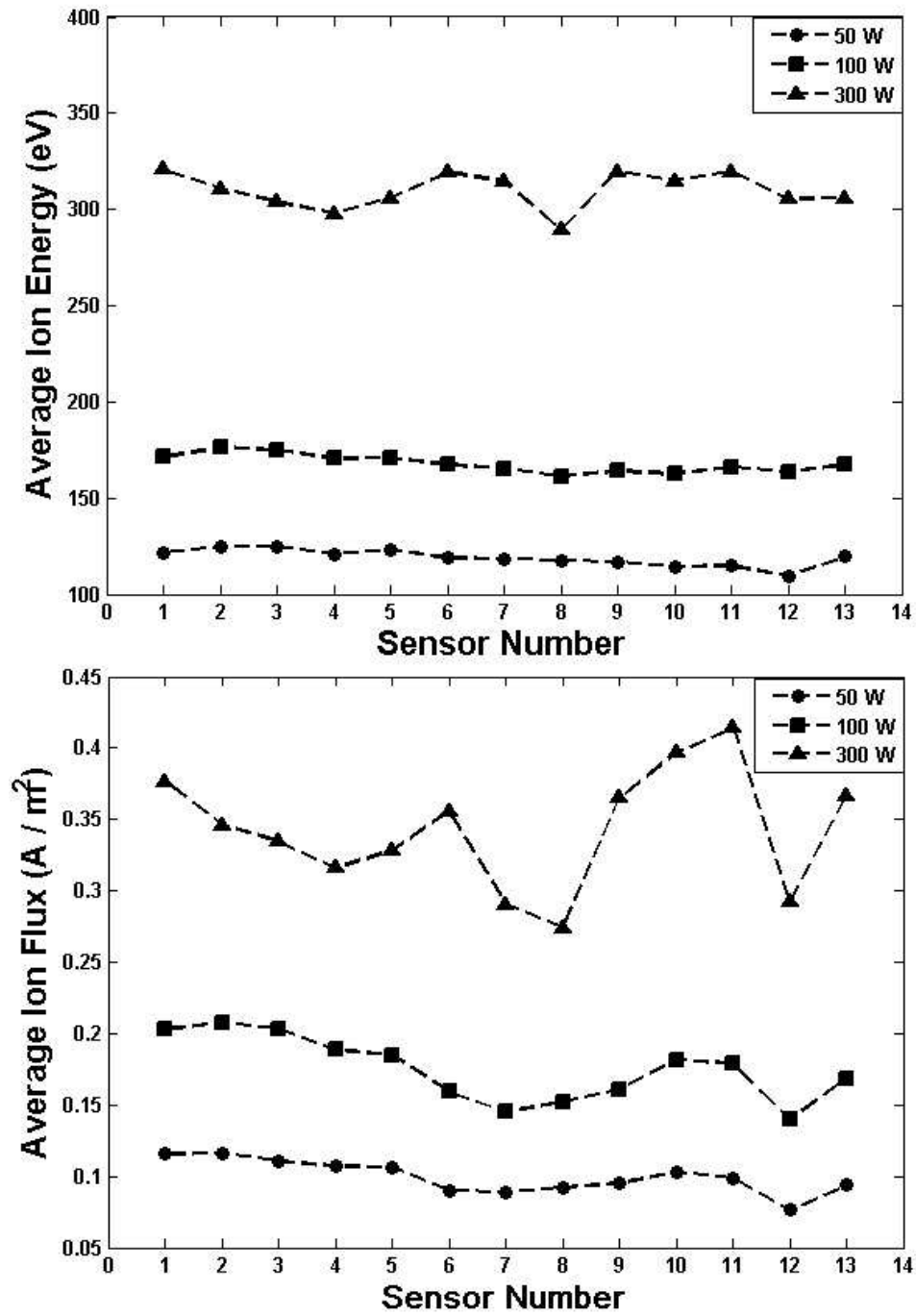
Figure 3.5: *Average ion energy (top) and flux (bottom) across the wafer at different discharge powers.*

3.4 Summary

A novel retarding field energy analyzer design capable of measuring the spatial uniformity of the ion energy and ion flux across the surface of a semiconductor wafer is presented. It can be installed without the need for any modifications to the plasma reactor. The multi-sensor design can be mounted on a grounded, floating or rf biased electrode at the substrate position in a plasma reactor. The design consists of 13 individual, compact-sized, RFA analyzers, all of which are multiplexed and controlled by a single acquisition unit. All the analyzers used to build this multi-sensor design have less than 2% variability from unit to unit due to tight manufacturing tolerances. The main sensor assembly consists of a 300 mm disk to mimic a semiconductor wafer and the plasma sampling orifices of each sensor are flush with disk surface. Individual RFA's are located strategically across the surface of the disk plate and is therefore capable of measuring the spatial profile of plasma parameters across the substrate/wafer location.

This device has been used to measure ion energy distribution, average ion energy, and average ion flux at 13 different locations over the surface of the powered electrode in an industrial capacitively coupled plasma reactor. Data are presented for varying discharge power levels of 50 W, 100 W and 300 W. The spatial variance and degree of spatial nonuniformity of the measured plasma parameters across the electrode has been determined. The ion energy and ion flux have been found to vary by approximately 5.1% and 20.2%, respectively, across the surface of the electrode for the range of conditions investigated in this study. This type of analysis is extremely important for modern plasma process design.

Following the measurement of plasma spatial profile, it is also important to measure ion angular distribution which can help achieve high etch directivity and conformal layer deposition. In order to measure ion incidence angle at the wafer surface, certain modifications are made in the internal geometry of the existing RFA design and a novel ion angular theory is developed. The angle resolved RFA with detailed analytical theory as well as simulation and experimental results is described in Chapter 4.

Ion angle distribution measurement with a planar
retarding field analyzer

4.1   Introduction

Angular distribution of ions and their energy play an important role in
plasma assisted etching and conformal deposition processes. Ion impact
at wider angles may be required for better step coverage in certain sputter
deposition and ion implantation processes while large angle ion impact
can be detrimental to anisotropic etch processes. Only a small number of
measurements have been reported of ion angular distribution in plasma
discharges either by rotating/tilting a quadrupole analyzer [55–57] or by
using a complex shaped electrostatic analyzer design with hemispherical
grids and large physical depth (~ 25 mm) [29, 58–60].

Stenzel *et al* [61, 62] developed a directional RFA in which particles

are geometrically filtered through a microchannel plate prior to energy analysis. The high aspect ratio of the holes/channels in the plate selects particles within a geometric acceptance angle of $\pm~0.6^0$. By rotating the directional analyzer, which was mounted on a movable shaft, across the beam direction they were able to determine angular beam divergence with precision. Azziz [63] carried out a set of experiments to determine plume divergence of a hall thruster using a planar RFA. The RFA was mounted on an automated rotating arm, which was driven by a stepper motor, and measured the ion energy distribution at angles of 0^0 to 90^0 in 10^0 increments.

In this chapter a novel method is introduced which can be applied to a planar RFA for the measurement of ion angular distributions. The RFA design, as detailed in Chapter 2, has a wide acceptance angle to allow ions with a wide angular spread to enter the device for detection. Due to their plane surface geometry the analyzer accept ions from all the angles within a hemisphere above their surface. The method enables the measurement of the ion energy distribution for a wide range of incident angles with an angular resolution of 3^0. The advantage of this technique is that the angular distribution of the ions arriving at the RFA surface can be determined at a fixed location. This is particularly useful for diagnosing rf plasma etching processes where the angular distribution of the impacting ions can play an important role in the process outcome. To our knowledge there have been no previous measurements of ion angular distribution, at a fixed location, reported using a planar retarding field analyzer. The content of this chapter has been published as a journal article [64].

59
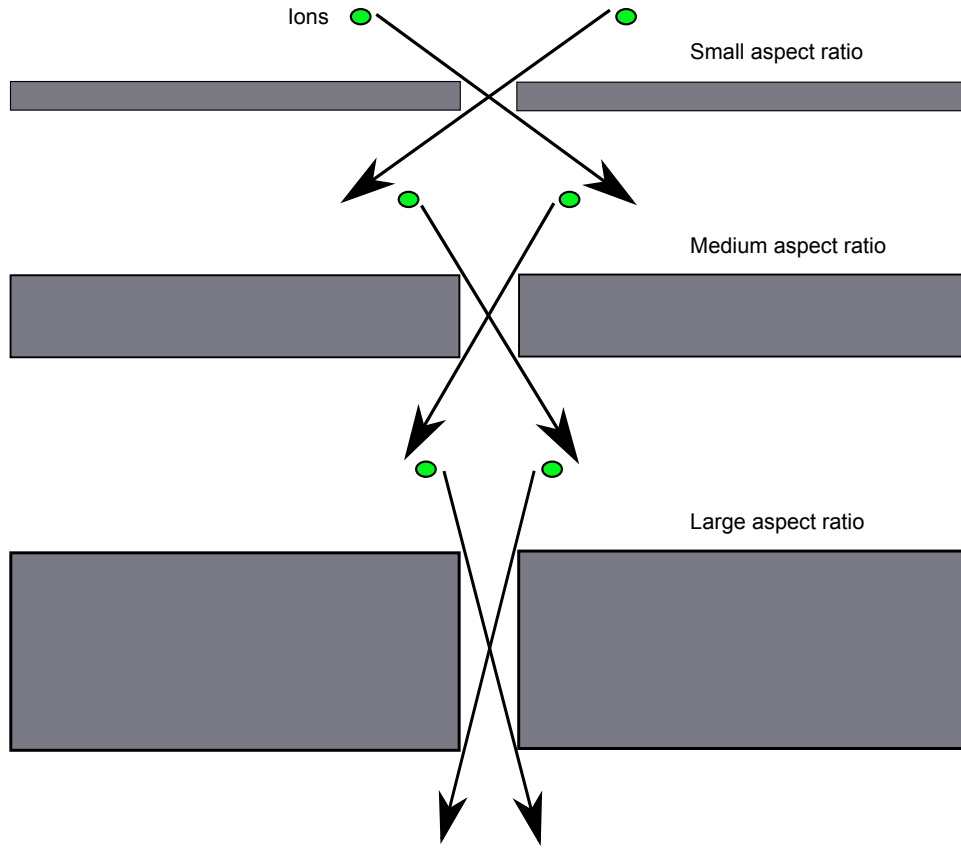
Figure 4.1: *Separation of ions with different angular spread by varying aperture aspect ratio*

4.2 Ion angular theory

Ions enter the retarding field analyzer through apertures of finite width and depth. As shown in figure 4.1, apertures with variable aspect ratio (depth / width) can be used to separate ions with different angular spread. The effective aspect ratio of the aperture in the standard retarding field analyzer structure can be varied either by physically adding additional thickness to increase the aperture depth, which can be accomplished by using a piezo-electric material or it can be done by changing the electric field between the two grids with a fixed separation. In this

work we employ the latter technique which we believe is novel to effectively vary the aspect ratio and discriminate ions with different angles of incidence.

Let us consider ions with total energy E bombarding the surface of a planar gridded RFA at a certain angle from the surface normal. The incoming ions will have a velocity component in the direction perpendicular to the sampling aperture v_I which corresponds to vertical energy component E_I and a velocity component in the direction parallel to the sampling aperture v_{II} which corresponds to parallel energy component E_{II}. In three dimensional space, if the axis of analyzer is assumed to be in z direction then the parallel and vertical velocity components can be interpreted as $v_{II} = \sqrt{v_x^2 + v_y^2}$ and $v_I = v_z$ respectively. If α is the angle of incidence at the surface of the retarding field analyzer then

$$\tan \alpha = \frac{v_{II}}{v_I} \tag{4.1}$$

$$\tan \alpha = \sqrt{\frac{E_{II}}{E_I}} \tag{4.2}$$

And

$$E = E_{II} + E_I \tag{4.3}$$

Equation (4.2) suggests that ion angle is determined by its vertical and parallel energy components. Ions with large E_I and small E_{II} have a small angle of incidence while ions with small E_I and large E_{II} have a wide incident angle. Therefore from figure 4.2, if

$$E_I^a < E_I^b < E_I^c < E_I^d < E_I^e < E_I^f \tag{4.4}$$

then

$$\theta_1 > \theta_2 > \theta_3 > \theta_4 > \theta_5 > \theta_6 \tag{4.5}$$
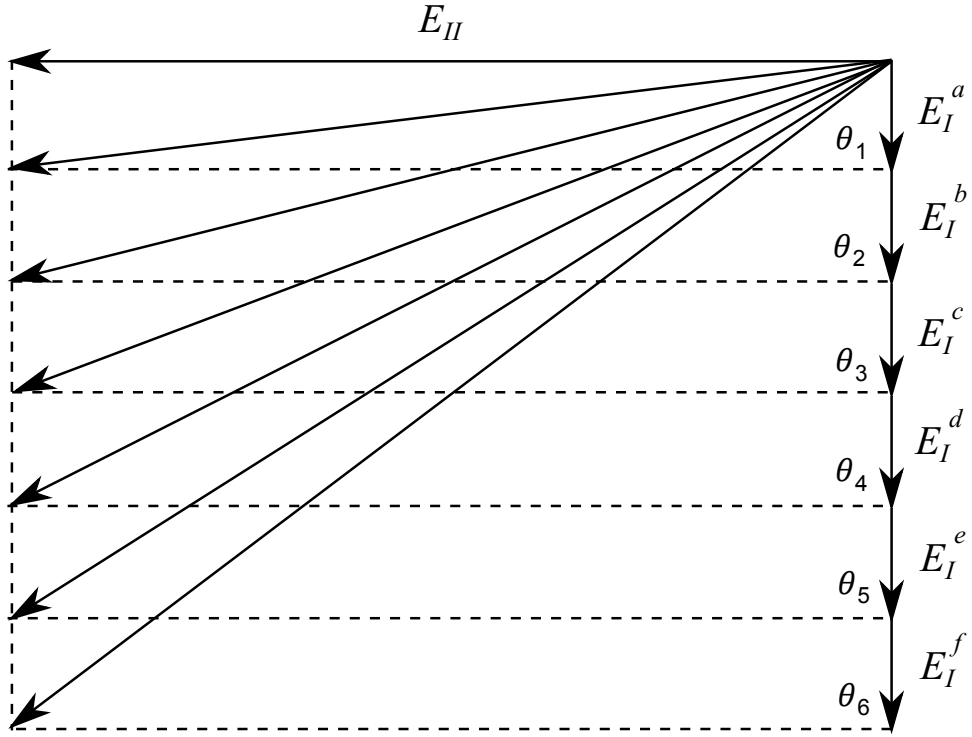
Figure 4.2: *Determination of ion angle by parallel and vertical energy component.*

Retarding field analyzers are designed to have electric fields in the vertical direction perpendicular to the grid surface only. Therefore potentials applied to any grid act primarily on the vertical energy component E_I of the incoming ions. The parallel component of ion energy E_{II} remains in theory unaffected by the electric field inside the sensor. Using the fact that at any location inside the sensor the E_{II} component of the ion energy remains identical to it's value when it entered the sensor through the sampling aperture, a mathematical approach to calculate incidence ion angle has been developed. The approach consists of increasing the electric field between the grids step by step in a systematic manner to collect ions with increasing order of incident angles.

4.2.1 Derivation of ion current as a function of ion angle

Let us assume ions arrive at a circular aperture of radius R and depth L at an angle ϕ from the surface normal. Ions hitting the side wall are lost and ions arriving at the bottom surface are collected. The ion current collected at an angle ϕ can be written as

$$I(\phi) = \int f(\phi)dS \tag{4.6}$$

Where $f(\phi)$ is the flux of ions at an angle ϕ, dS is the surface area element and the integral is around the surface of the aperture. The aperture area is comparatively very small relative to the total cross sectional area of the ion flux coming from plasma volume and hence it is reasonable to assume the flux of ions $f(\phi)$ to be constant over the integral. Therefore

$$I(\phi) = f(\phi) \int dS \tag{4.7}$$
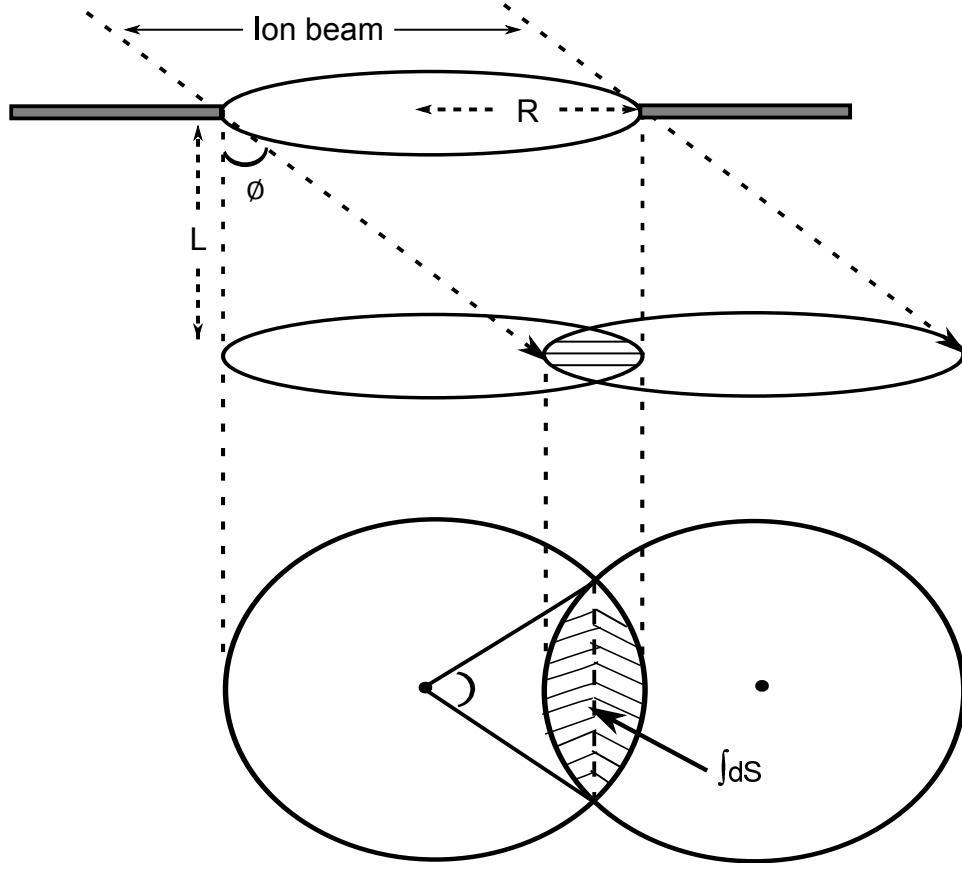
Figure 4.3: *Geometrical calculation of effective ion current collection area.*

$\int dS$ is the overlapping area (which is shown as the dark region in figure 4.3) of two circles where one circle is the projection of circular aperture and the other circle is the projection of the circular ion beam on the collector plate. Ions arriving in this overlapping area will be collected and therefore $\int dS$ can be said to be the effective ion current collection area.

The effective ion current collection area $\int dS$ is calculated using trigono-geometrical methods in terms of angle ϕ as,

$$\int dS = 2R^2 \cos^{-1}\left(\frac{L\tan\phi}{2R}\right) - L\tan\phi\sqrt{R^2 - \left(\frac{L\tan\phi}{2}\right)^2} \qquad (4.8)$$

From (4.7) and (4.8), setting R = L (which is of the order of $\sim 400 \ \mu$m) as per the device design and since ion flux is constant, the normalized collected ion current at an angle ϕ can be approximated as

$$I(\phi) \approx 2 \cos^{-1}(\frac{\tan \phi}{2}) - \tan \phi \sqrt{1 - (\frac{\tan \phi}{2})^2} \qquad (4.9)$$

(4.9) defines ion current as a function of incidence angle ϕ when $\tan \phi <$ 2, ions will be lost hitting the side wall when $\tan \phi \geq 2$ and no ion current will be collected. (4.9) suggests that variation of ion current is equivalent to variation of effective ion current collection area.

4.2.2 Simulation and ion current approximation

A commercial charged particle simulation software package SIMION [65] version 8.0 was used to model a circular aperture of radius R and depth L and a collector plate located just behind the rear end of the aperture as shown in figure 4.4. SIMION has widely been used for over 30 years to simulate lens, mass spec, and other types of 2D or 3D charged particle optics systems. This software calculate electric fields and the trajectories of charged particles in those fields when given a configuration of electrode geometries with voltages and particle initial conditions (velocity, kinetic energy, angle, mass, charge, distribution etc.). The program uses direct methods such as finite-difference with much optimized linear-time solving, Runge-Kutta with variable-length and controllable time-steps which provides correct and reasonably fast calculations to determine resultant fields and particle trajectories. The software is programmable with data recording and visualization capabilities to effectively simulate real-world analyzers and instruments. The software package is easy to install and runs well on windows.
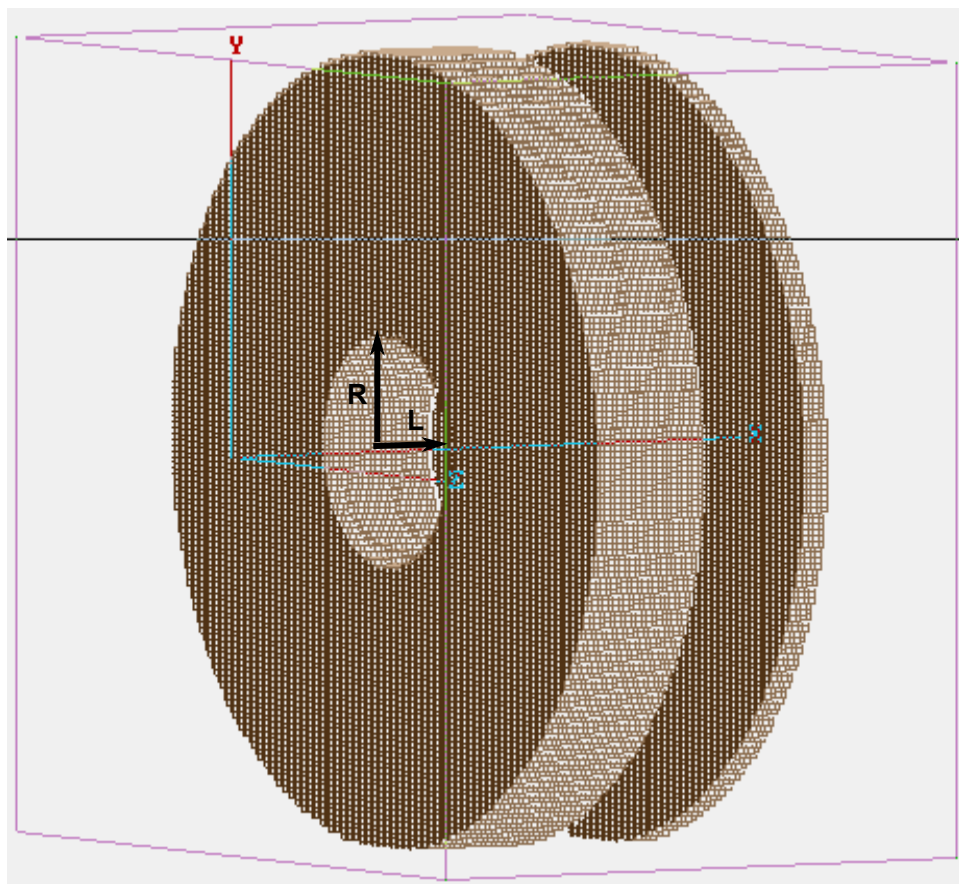
Figure 4.4: *Circular aperture and the collector plate defined in a potential array space.*

Using SIMION, an aperture having a geometrical diameter of 80 grid units was created in a solid electrode of thickness 40 grid units in the three dimensional potential array space. The dimension of one grid unit was set to be 10 μm and therefore R = L = 400 μm. A sufficiently large number greater than 10^4, of positively charged particles with 40 amu mass and initial kinetic energy in uniform distribution between 1 eV to 100 eV, to imitate argon ions, were defined in a filled circle distribution just above the front end of the aperture as shown in figure 4.5 (a). The defined particles forming a directional circular ion beam were injected from the front end of the aperture as shown in figure 4.5 (b).

The circular ion beam was injected at various angles with respect to the aperture axis. Initially ions were injected at 0^0 so that maximum number of ions can reach the collector. Next, ions were injected at an initial angle of 3^0 which resulted in a fraction of the ions getting lost by hitting the side aperture walls and the remaining ions transmitted through the aperture depth reaching the collector plate were recorded. The process was repeated at slightly higher angle of 6^0 and then 9^0 and so on, in the steps of 3^0, until the number of transmitted ions reaching the collector plate approached to zero. In each run, the number of particles injected through the aperture were chosen to be same so as to keep the ion flux constant. The size of time-steps was mainly controlled by the trajectory quality factor which was set at the default value of +3 providing reasonable speed and accuracy of ion trajectory calculation. The whole process of injecting ions at various incident angles is summarized in figure 4.6.

A similar set of simulations was also conducted for an isotropic ion beam. In order to mimic an isotropic ion beam, positively charged parti-
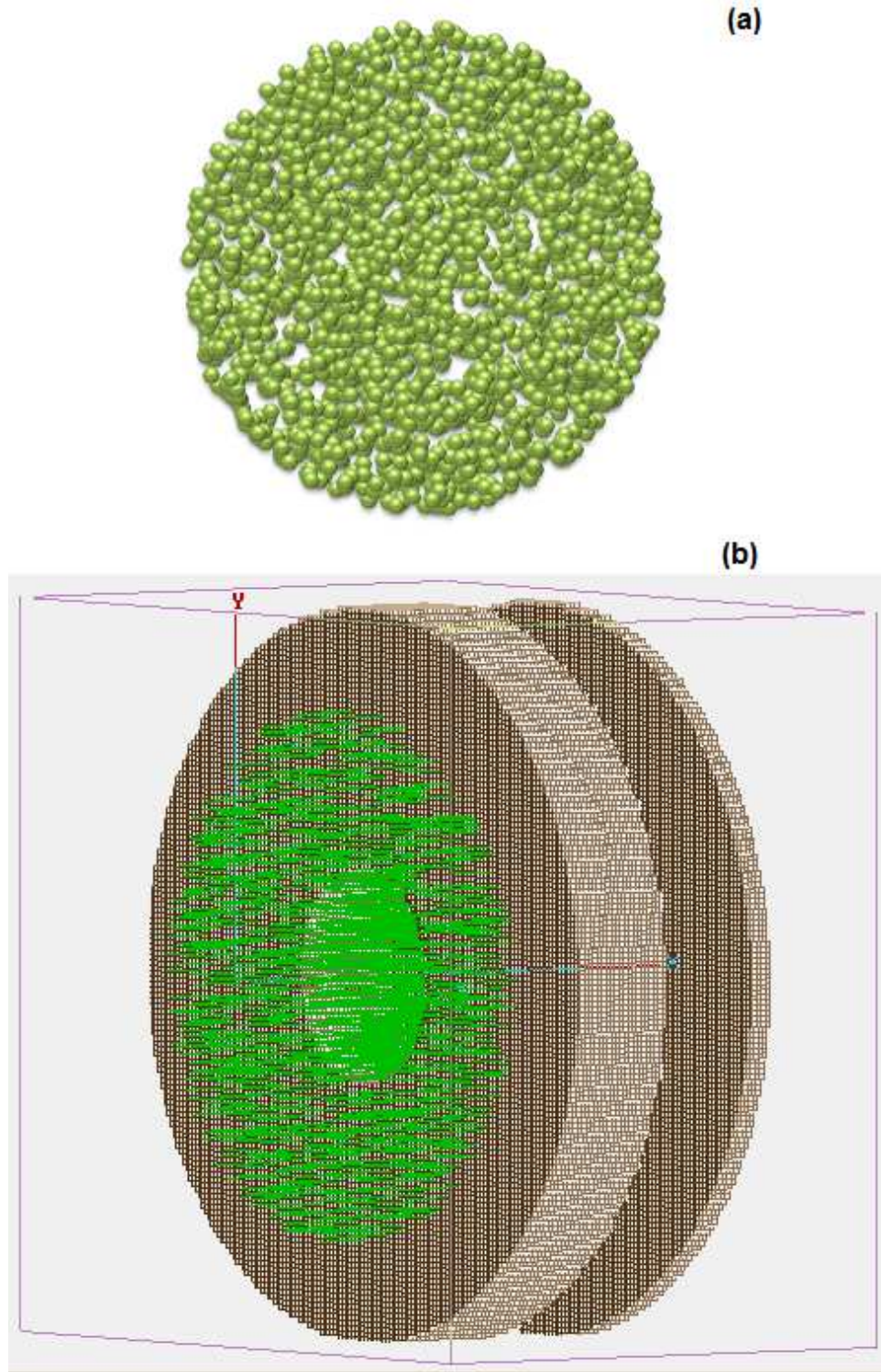
Figure 4.5: *(a) Ions defined in a filled circle distribution and (b) Ions injected into the aperture.*
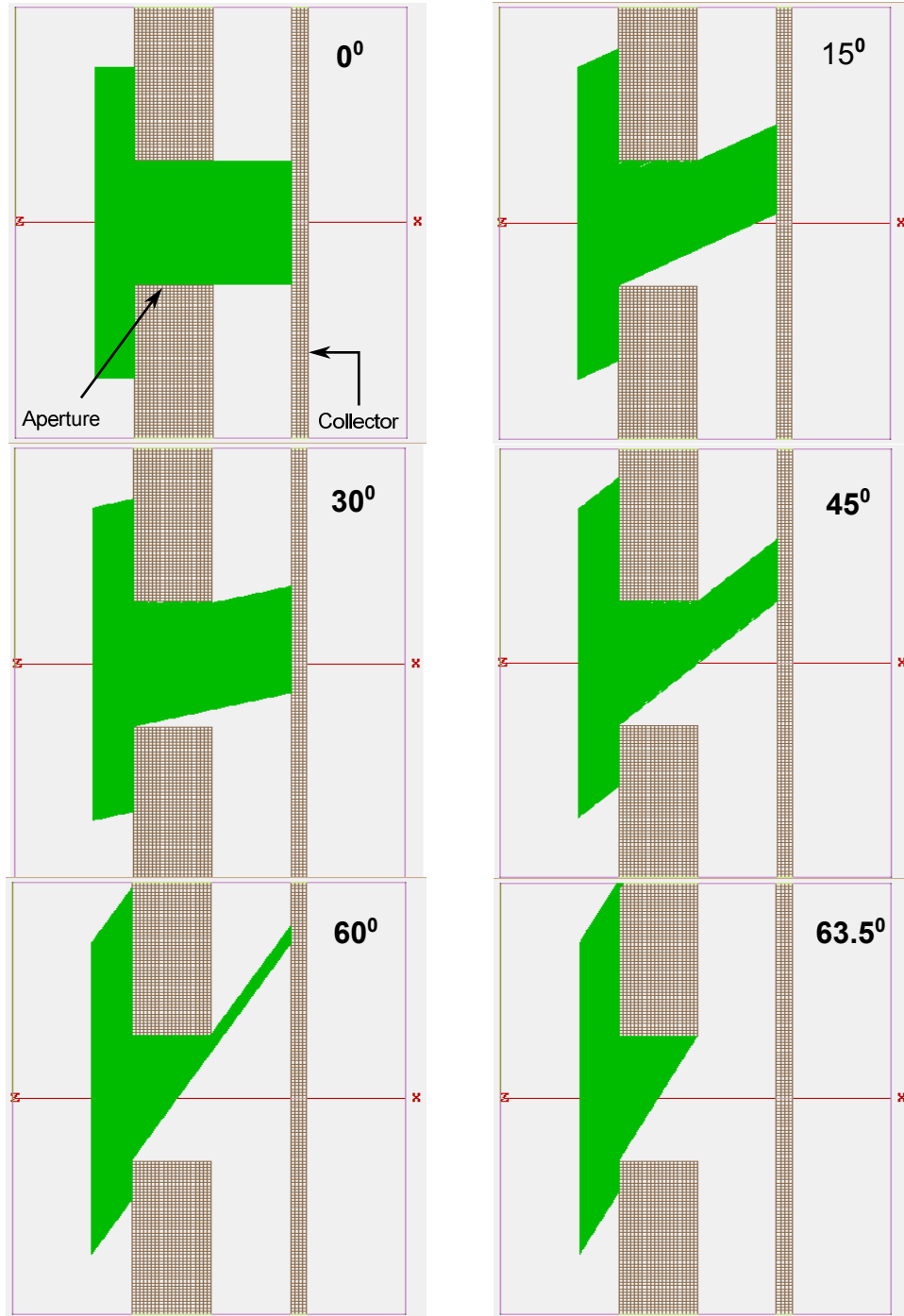
Figure 4.6: *Injection of circular ion beam in to the aperture at various angles.*
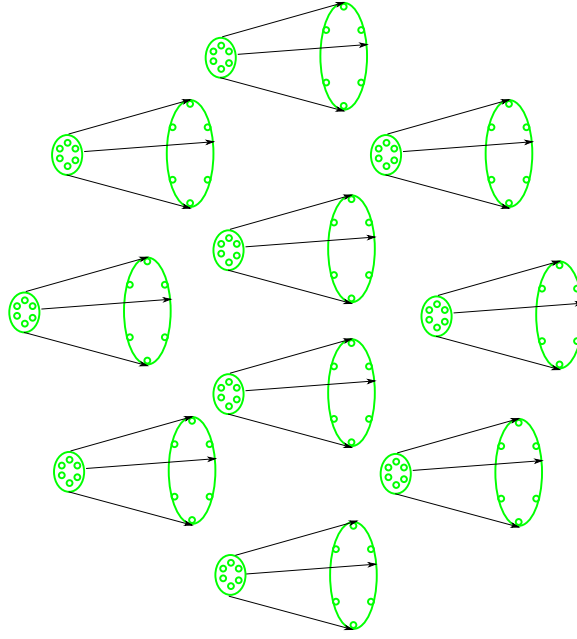
Figure 4.7: *Particle sets having cone direction distribution defined in a circle.*

cles defined in a filled circle distribution were divided in to a number of
particle-sets, each set has fixed number of particles having cone direction
distribution as shown in figure 4.7. These sets of ions were injected in to
the aperture at various half-angles. Ions transmitted through the aper-
ture and reaching the collector plate were recorded. The whole process
of injecting cone directional ion-sets at various half-angles is summarized
in figure 4.8. We have found that number of ions recorded at the collec-
tor plate having various incident half-angles were exactly same as that of
directional ion beam incident at similar incident angles. In both cases of
directional and isotropic circular ion beam configurations, no ion reaches
the collector when incidence angle approaches to 63.5^0.

Then, using (4.8), the resultant ion current collection area as a func-
tion of incident ion angle was calculated. In figure 4.9, the variation
of normalized ion current and effective ion current collection area with
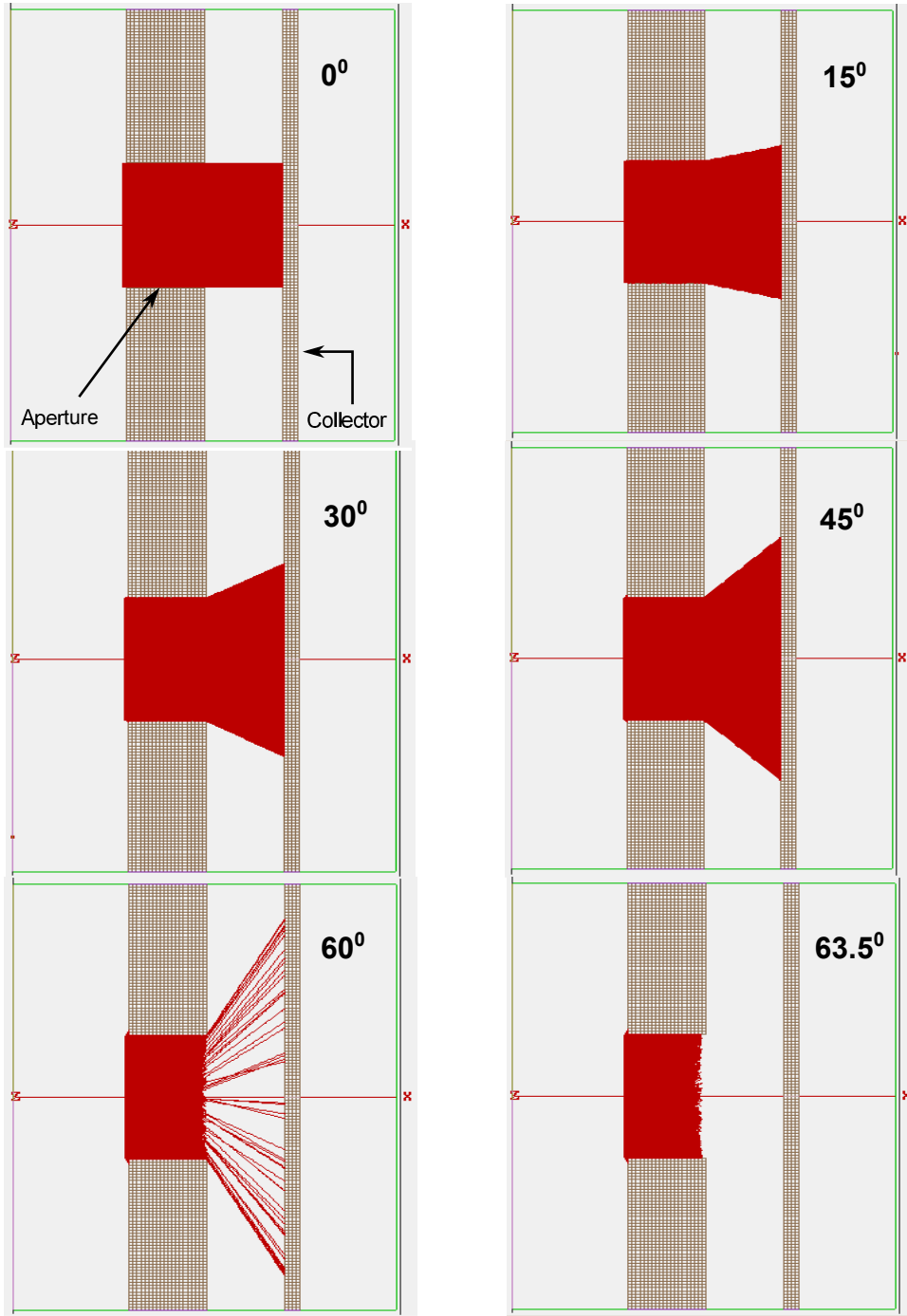
Figure 4.8: *Injection of isotropic ion beam in to the aperture at various half-angles.*
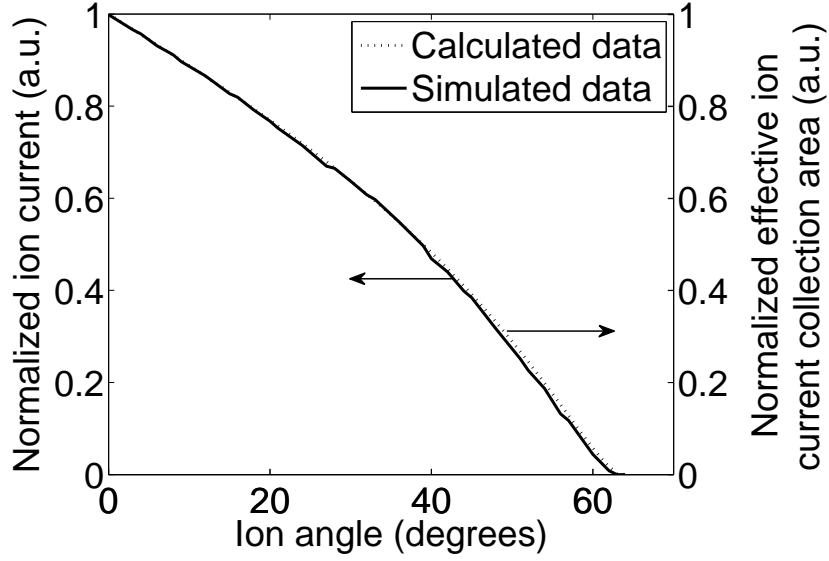
Figure 4.9: *Comparison of simulated and calculated graphs for ion current and ion current collection area respectively.*

incident ion angle is shown for simulated and calculated data. The two graphs show excellent agreement, which confirms that the formula derived for effective ion current collection area can also be used to approximate the total ion current.

4.3 Calculation method

The internal design of standard RFA as described in Chapter 2, has been slightly modified to enable the method work. The RFA has 4 grids (including the first grid which is electrically joined to the analyzer's orifice) and one collector plate as shown in figure 4.10. Each grid has a thickness of 30 μm and 50% transmission. The spacing between first and second grid as well as second and third grid is 200 μm, it is 400 μm between third and fourth grid, spacing between fourth grid and collector is 200

μm. In addition, thin metallic foils having a thickness of 30 μm with similar arrays of orifices as that of the plasma facing surface are electrically joined with third and fourth grid, precise alignment of orifices is maintained throughout the depth of the sensor such that wide angle ions from one cell are lost hitting the metallic foil before entering the nearby cell and no cross talk between the cells can occur. The total distance an ion travels within the analyzer before reaching the collector is therefore only 1.15 mm, the compact design can be considered as collision free at pressures up to 100 mTorr and does not need any differential pumping for argon plasma. A potential V_0 is applied to the orifice surface and Grid G_0, V_1 to grid G_1, V_2 to grid G_2, V_3 to grid G_3 and V_c is applied to the collector plate.

If ions are bombarding the aperture surface and hitting the top grid G_0 at an angle α from the normal, angle (α) can be expressed by (4.1). If the potential difference between grid G_0 and G_1 adds up to the ion's vertical energy component, it will cause the ion to deflect and changes the angle when it exits G_1 to β, it is worth mentioning here that in reality ion trajectories would not be straight as shown in figure 4.10 and would be curved instead. The ion would keep changing angle while passing between the two grids and eventually leaves G_1 at an approximate angle β given by

$$\tan \beta = \sqrt{\frac{E_{II}}{E_I + e(V_0 - V_1)}} \tag{4.10}$$

After passing through G_1, the ion will deflect again due to the potential difference between G_1 and G_2 and change angle to γ while exiting grid G_2

$$\tan \gamma = \sqrt{\frac{E_{II}}{E_I + e(V_0 - V_1) + e(V_1 - V_2)}} \tag{4.11}$$
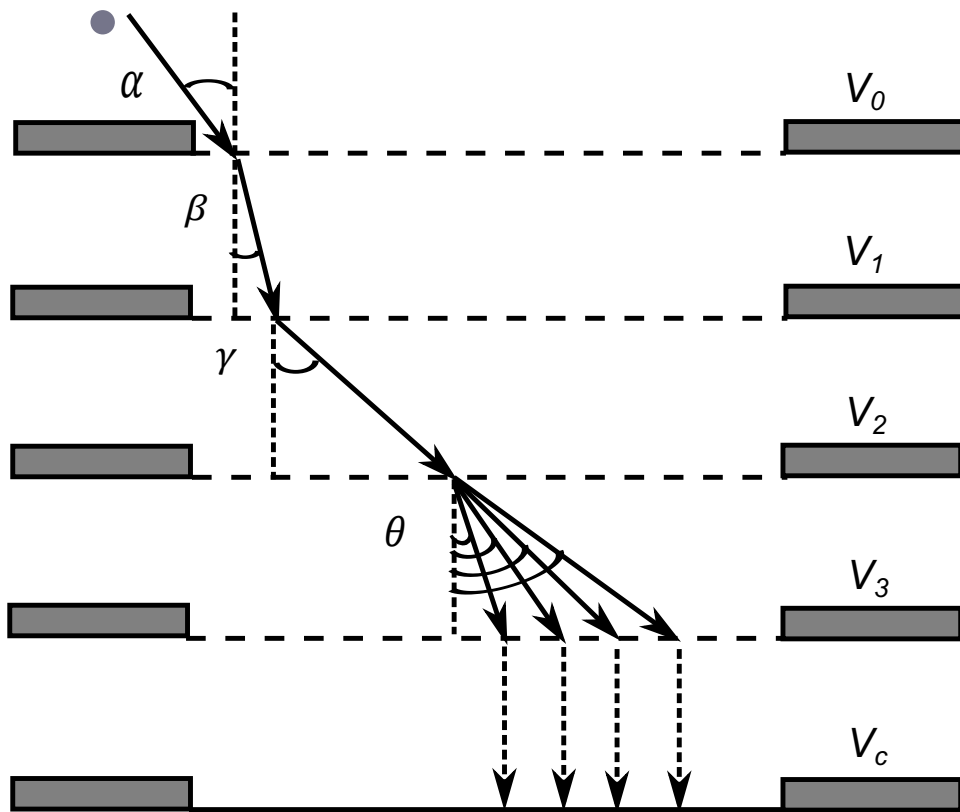
Figure 4.10: *Internal grid structure and ion movement inside a typical planer retarding field analyzer.*

In the end the ion will hit the surface of grid G_3 and exits at an angle θ such that

$$\tan\theta = \sqrt{\frac{E_{II}}{E_I + e(V_0 - V_1) + e(V_1 - V_2) + e(V_2 - V_3)}} \qquad (4.12)$$

The compact analyzer design (thickness $\sim$ 1 mm) and the accelerating potential (V_c) applied at the collector plate allows all the ions passing through G_3 to be collected and so angle θ can be said to be the collection angle.

The collection angle θ can also be expressed as

$$\tan\theta = \sqrt{\frac{E_{II}}{(r + r')E_I}} \qquad (4.13)$$

where r and r' are constants which depend on grid G_2, grid G_3 potentials and vertical ion energy component E_I. Collection angle θ can be related to incidence angle α such that

$$\tan\theta = \sqrt{\frac{1}{(r + r')}}\,\tan\alpha \qquad (4.14)$$

We have empirically derived an expression for r given by

$$r = \frac{e(V_2 - V_3)}{E_I} \qquad (4.15)$$

r is the ratio of grid G_2 to grid G_3 potential difference to the vertical ion energy component. A similar expression is derived empirically for r' as

$$r' = \frac{E_I - e(V_2 - V_0)}{E_I} \qquad (4.16)$$

r' is the ratio of difference between the vertical ion energy component and grid G_0 to grid G_2 retarding potential to the vertical ion energy component.

A similar expression to (4.4) can be written for ion current at a collection angle θ as

$$I(\theta) \approx 2\cos^{-1}(\frac{\tan\theta}{2}) - \tan\theta\sqrt{1 - (\frac{\tan\theta}{2})^2} \qquad (4.17)$$

Using (4.14) and (4.17) the total ion current at an incidence angle α can be calculated as

$$I(\alpha) \approx 2\cos^{-1}(\frac{\tan\alpha}{2\sqrt{(r+r')}}) - \frac{\tan\alpha\sqrt{1 - \tan^2(\alpha)/4(r+r')}}{\sqrt{(r+r')}} \qquad (4.18)$$

(4.18) describes ion current as a function of incidence angle α and ratios (r and r').

(4.15) and (4.16) suggest ratios to be functions of ion energy and grid potentials, therefore (4.18) defines ion current as a function of ion energy, incidence ion angle and grid G_2 / grid G_3 potentials when $\tan\alpha < 2$, ion current will be zero when $\tan\alpha \geq 2$. (4.18) proposes the possibility to segregate ions with different energy and angular spread by varying grid G_2 and grid G_3 potentials. Using the above equation, a mathematical algorithm has been developed to relate different ion angular segments with variable ratios (r and r'), by smart selection of ratio values ion current at different incident angles are related to grid G_3 potential. In the algorithm, resultant ion current is calculated by varying grid G_2 potential in a range to cover all possible energies the ions may have and for each selected grid G_2 potential, the potential at grid G_3 is swept in a range to cover all possible angles the ions can have. In this way a matrix of ion current values with n rows and m columns is constructed and can

be represented as

$$M = \begin{pmatrix} M_{1,1} & M_{1,2} & \cdots & M_{1,m} \\ M_{2,1} & M_{2,2} & \cdots & M_{2,m} \\ \vdots & \vdots & \ddots & \vdots \\ M_{n,1} & M_{n,2} & \cdots & M_{n,m} \end{pmatrix}$$

All the data for ion energy and angle is contained in this matrix and there may be a number of ways to extract the information. One simple method to extract the ion energy and angle data is to take a derivative across the first row and repeat the same for all n rows. In this way a new matrix of derivative values with n rows and $(m-1)$ columns is constructed and can be represented as

$$\delta M = \begin{pmatrix} \delta M_{1,1} & \delta M_{1,2} & \cdots & \delta M_{1,m-1} \\ \delta M_{2,1} & \delta M_{2,2} & \cdots & \delta M_{2,m-1} \\ \vdots & \vdots & \ddots & \vdots \\ \delta M_{n,1} & \delta M_{n,2} & \cdots & \delta M_{n,m-1} \end{pmatrix}$$

The success of this method depends on how well grid G_3 potential is chosen to be a certain fraction of grid G_2 potential determined by the ratio r. This ratio and the grid G_3 potential steps are managed in such a way as to relate each consecutive row of the matrix δM to a subtended angle of approximately 3 degrees. If the first row of matrix δM is represented by δM_1, the second row is represented by δM_2 and so on then a plot of δM_1 with respect to grid G_2 potential will approximate the ion energy distribution between 0 to 3 degrees, a plot of δM_2 reveals ion energy distribution between 3 to 6 degrees, δM_3 plot uncovers the ion energy distribution between 6 to 9 degrees and so on. In this way ion angles up to 24 degrees in steps of 3 degrees can be measured correctly as per the
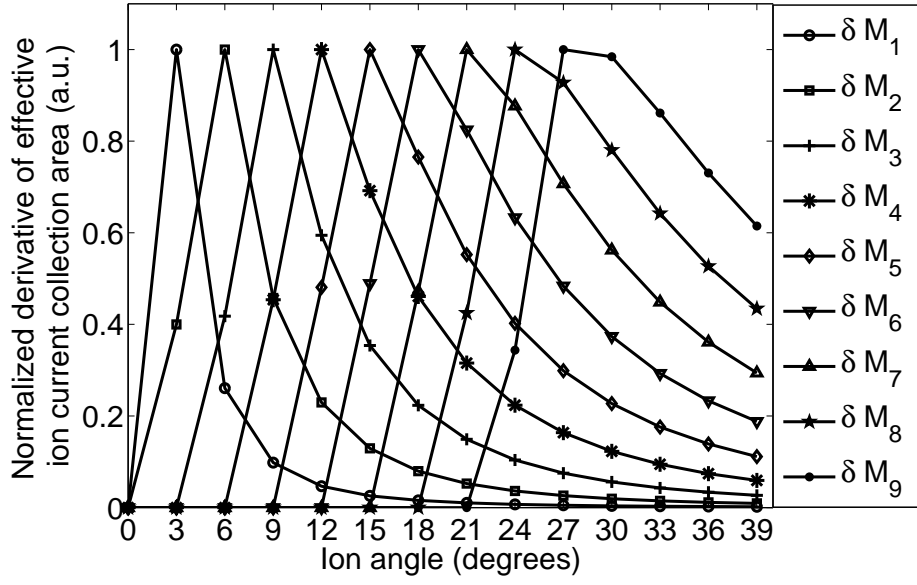
Figure 4.11: *Ion angle measurement with the calculated derivative values.*

analytical theory derived. For most plasma processes ions are expected to have less than 20 degrees of incidence angle with chamber pressure of up to several hundred milli-Torr, and therefore the method and the technique presented in this chapter is capable of diagnosing various plasma processes for the measurement of ion energy and angular distributions.

The method is described in figure 4.11 showing the variation of the derivative of the effective ion current collection area as a function of incident angle. Matrix row δM_1 exhibits peak at 3 degrees, δM_2 at 6 degrees, δM_3 at 9 degrees and so on up to 24 degrees calculated correctly. As described in (4.7), the ion current is the product of ion flux and effective ion current collection area, hence depending upon at what angles ion flux is coming to the surface of analyzer, the ion current will exhibit a peak depending on which angle the derivative is sensitive to and how much ion flux is at that specific angle. The derivative approach has good
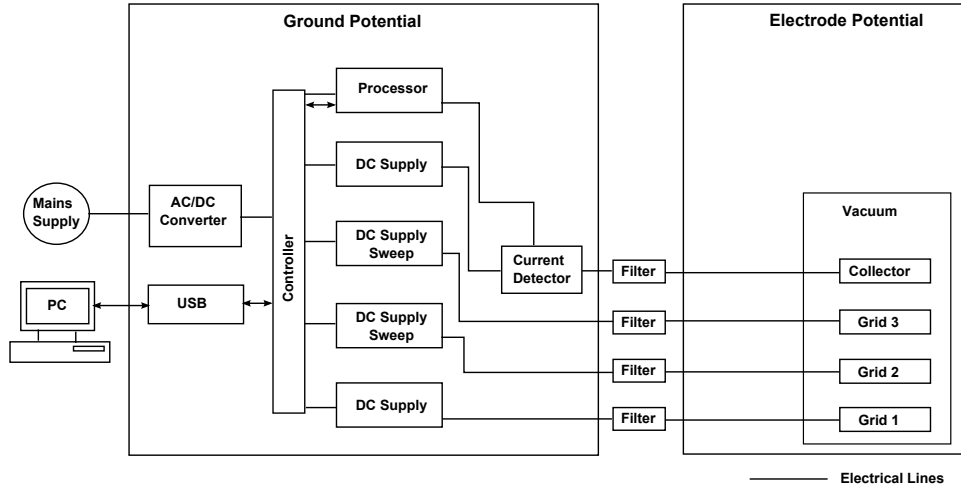
Figure 4.12: *Block diagram of the system electronics and the data acquisition setup.*

resolution at low angles but the resolution is poorer at higher angles. More complex methods to extract the angular distribution are possible but are outside the scope of this work.

4.4 System electronics and experimental investigation

The complete angle resolved RFA system consists of three major hardware components: sensor with the cabling, vacuum feedthrough with electronic circuitry and data acquisition control box. A block diagram of the major components of the system electronics is shown in figure 4.12. The overall control electronics and data acquisition unit is same as for standard RFA system and which is described in Chapter 2, except that a dc supply sweep is used for G_3 instead of a fixed supply.

The angle resolved RFA system [66] was set up to conduct an ex-

periment on a parallel plate, capacitively coupled, 13.56 MHz RF driven plasma reactor. The reactor consists of two metal electrodes of 300 mm diameter separated by a relatively small gap of 45 mm. RF power of 20 W is supplied to the top electrode, through an automatic matching unit and the discharge is maintained at a pressure of 2.5 Pa in argon gas. The planar retarding field analyzer is placed on the grounded bottom electrode, top grid G_0 is kept in electrical contact with the chassis which is at the electrode potential, grid G_1 is biased negatively (-60 V with respect to G_0) to repel plasma electrons, a potential sweep (-10 V to +50 V with respect to G_0 and a step size of 1 V) is applied at grid G_2 to select the energy window, a second potential sweep (100% to 70% of existing G_2 potential in the steps of 3%) is then applied at G_3 for each energy selected which discriminate the ions based on their incidence angle. The collector, C, is biased with the same negative potential as G_1 (-60 V with respect to G_0) and used to collect and record the ion current as a function of grid potentials.

A matrix of recorded current values is constructed with varying G_2 potential across the row and varying G_3 potential across the column which is followed by a second matrix constructed by taking derivatives across each row. For the given plasma discharge ions are expected to be low in energy ($\sim$ 10 - 30 eV), arriving at the analyzer surface in a small and narrow angle range as the sheath electric field would be sufficient enough to straighten them out before entering the RFA's aperture. In figure 4.13, a plot of the first row shows a large signal which confirms that most of the ions are incident in an angle range of $0-3^0$, a very small signal is seen for the second row indicating a comparatively very small number of ions are incident in $3-6^0$ of angle range and no detectable
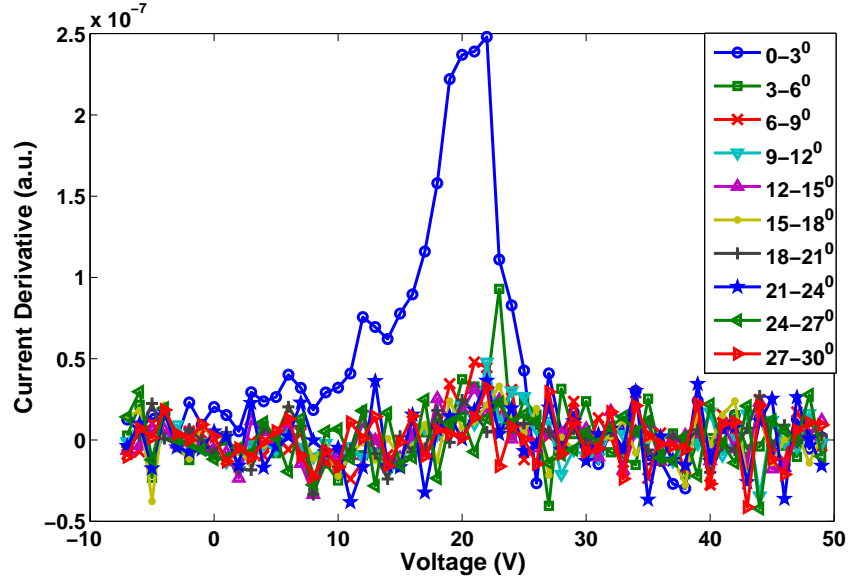
Figure 4.13: *Ion angle determination with current derivative method.*

signal is seen at large angles from the normal which is as expected.

4.5   Summary

In summary a mathematical formula has been derived for ion current as a function of incident ion angle, ion energy, aperture geometry and grid potentials. Based on calculated ion current values a novel technique has been demonstrated to measure ion angle distribution using a planar retarding field analyzer. The technique involves discrimination of ions with different angular spread by varying the effective aperture aspect ratio. The aspect ratio is varied by increasing the electric field between two grids having fixed separation in a systematic manner so as to relate each voltage step to a subtended angle of approximately 3 degrees. A one-to-one comparison of simulated and calculated values of the ion current and ion current collection area (which shows excellent agreement)

provides strong support to the developed theoretical framework.

The analytical theory and derivative method presented in this chapter to extract the ion angle information from the populated matrix has been tentatively validated by conducting an experiment on a capacitively coupled plasma (CCP) reactor and it has been found that for the given plasma process the major angle of ion incidence is between $0-3^0$ from the normal as expected. More sophisticated methods to extract precise ion angle information from the matrix can be developed. Additional work of measuring higher ion angles in wide ion angle plasma processes to further validate this technique is required.

One more crucial parameter together with ion angular distribution which can influence etch anisotropy is the ion-to-neutral flux ratio. Certain improvements are made in the existing design of RFA to enable the sensor to measure ionized flux fraction and deposition rate by employing a quartz crystal in place of the collector plate. The improvement in the design with details of the modifications followed by theoretical and experimental research work is presented in Chapter 5.

A retarding field analyzer with embedded quartz

crystal microbalance to measure deposition rate, ion

energy distribution and ionization fraction

5.1 Introduction

Thin films of various materials are deposited on semiconductor wafers for a variety of applications in integrated circuit manufacturing. The rate of deposition is controlled by neutral and ionic species arriving at the substrate surface. In sputtering processes the ionization fraction, defined as ratio of ion to total (ion + neutral) deposition rates, is mainly determined by the applied cathode power, chamber pressure and the target material (since the ionization potential is material dependent). Plasmas with a wide range of fractional ionization find applications in semiconduc-

tor processing. Depending on the deposition process, ionization fraction can vary significantly in a range from less than 1% to as high as nearly 100%. Thin film quality and deposition rates are strongly dependent on the fraction of ionization and therefore measurement of ionized flux fraction to the substrate is becoming critical for process development and control.

Over the past two decades, several researchers have reported measurements of ionization fractions in deposition processes. Bohlmark *et al* [67] measured the ionization fraction of Titanium (Ti), sputtered by a HiPIMS process, using optical emission spectroscopy (OES). Yamashita [68] used a retarding potential method to make a rough estimation of the ionization fraction of the sputtered copper (Cu) atoms. A control grid was placed directly above the substrate and biased to either repel or admit Cu ions. Using optical profilometry, a sample with Cu ions repelled and a sample with Cu ions admitted were compared and the ionization fraction of sputtered atoms impinging on the substrate was determined. Rossnagel and Hopwood [69, 70] developed a quartz crystal microbalance (QCM) with integrated grids to determine the ionization fraction in a magnetron sputtering discharge. By suitable biasing of the grids, ions were either admitted or repelled. Their setup required differential pumping to avoid collisions of metal ions with the background gas inside the analyzer. An important limitation of their setup is that the QCM is maintained at ground potential and does not mirror the variations in the substrate potential. Another limitation is that their design is only useful at low plasma densities since the grids becomes ineffective at higher ion densities (>3 x 10^{11} cm^{-3}) when plasma penetrates through. Green *et al* [71] built a similar but improved design, they employed a three-grid

energy analyzer to reduce plasma penetration and maintained the QCM at the substrate potential, overcoming the limitations which Rossnagel and Hopwood had. They have further calibrated the measurement of ionization fraction by considering the effects of pressure and shadowing of the gridded energy analyzer geometry. Based on a solid angle calculation, a geometric correction factor as a function of QCM characteristic dimension was determined.

Allain *et al* [72] measured ionization fraction for two metal targets (Cu and Ti) using three different working gases (Kr, Ar and Ne) to investigate the effect of target material and working gas on the ionization fraction and deposition rates using the same diagnostic as described by Green *et al* [71]. Meng *et al* [73] constructed a similar three gridded analyzer combined with a QCM to study variation of ionization fraction as a function of input power (2 - 15 kW) and pressure (5 - 40 mTorr) in a commercial high power hollow cathode magnetron deposition tool. Wu *et al* [74] utilized a similar QCM design to investigate Argon (Ar) ion flux to Cu ion flux ratio in an ionized PVD system with Cu target and Ar as working gas. Snodgrass *et al* [75] developed a totally grid-less ionized metal flux fraction measurement tool in which voltage bias was directly applied to the front surface of the QCM in order to repel or admit ions. The need for grids above the QCM was eliminated by employing a magnetic field which was oriented parallel and just above the surface of the crystal to protect the crystal from drawing the unwanted electron current when biasing the crystal surface above the plasma potential. Poolcharuansin *et al* [76] utilised the same method of applying potential directly to the QCM but instead of employing a magnetic field an external grid to repel electrons was used.

In this work we present a compact deposition rate monitor with some similarities to the design proposed by Green *et al* [71] in which a quartz crystal is embodied within a compact RFA. In the developed design, the collector plate was replaced by the front facing electrode of the quartz crystal. The quartz crystal provides a direct measurement of the deposition rate at the substrate location while the RFA grids can be configured to turn on and off the ion flux. In this way the deposition rate can be determined when both neutrals and ions are present and when only neutrals are present. From these two measurements the ionized flux fraction and neutral flux fraction can easily be determined. The unified RFA-QCM design [77] is also capable of measuring the ion energy distribution (IED) at the substrate location under processing conditions.

One of the key advantages of this sensor design in real world applications is that it does not require water cooling to compensate for temperature effect. Calibration of the measurement crystal using an undeposited reference crystal eliminates the need for a complex water cooling mechanism. Another key feature of this design is that it can be placed on a grounded, floating, dc, pulsed-dc (p-dc) or rf biased electrode without the need to modify the electrode in any way. The use of high input impedance low pass filters enables the collector and grids to float at the electrode potential. The compact and shallow structure provides greater operating pressure range, up to approximately 100 mTorr, without the need for differential pumping.

In this research work, the IED and Cu deposition rates are studied using the unified RFA-QCM design in an asymmetric bipolar p-dc sputtering system which is a common technique in the deposition of high quality thin film and advanced coatings having improved electro-mechanical

86

properties and fewer defects and voids. Compared to conventional dc sputtering, bipolar p-dc sputtering has higher ion current density, self bias voltage and thermal substrate load, due to the strong ion and electron bombardment on the substrate, thereby depositing dense and rigid films. Commonly seen arcing problems during sputter deposition processes can also be suppressed to a large extent by pulsed powering the cathode[78]. Typically, these sources are operated in the frequency range of 20-350 kHz with duty cycles varying from 40% to 90%. A detailed review of unipolar and bipolar (symmetric and asymmetric) p-dc magnetron sputtering techniques have been given by Schiller [79] and Sproul [80] *et al.* The effect of ion energy, substrate rf biasing, discharge power and pressure on the deposition rate are also examined. The content of this chapter has been published as a journal article [81]

5.2   Theoretical background of the QCM

The use of a piezoelectric quartz crystal resonator to measure deposited mass was first investigated by Sauerbrey [82] in 1959. It was found that the change in resonant frequency of the crystal was proportional to the mass of a uniformly deposited layer on the crystal surface. The Sauerbrey equation relates the decrease in resonant frequency Δf to the added mass Δm as follows:

$$\Delta f = -\frac{2f_0^2}{A\sqrt{\rho_q \mu_q}}\Delta m \tag{5.1}$$

where f_0 is the resonant frequency (Hz), A is the active crystal area (area between electrodes, cm^2), ρ_q is the density of quartz (g/cm^3), μ_q is the shear modulus of quartz crystal (g.cm^{-1}.s^{-2}).

(5.1) can be rewritten as

$$\Delta m = -\frac{\Delta f}{C_f} \tag{5.2}$$

where $C_f = \frac{2f_0^2}{A\sqrt{\rho_q\mu_q}}$ is the sensitivity factor of the quartz crystal.

For small masses of material the shift in resonant frequency is independent of the material properties and as long as the accumulated mass deposited on the crystal does not shift the resonant frequency by a few percent of its original value, Δf varies linearly with Δm . The validity of (5.2) requires:

(1) the deposited mass and thickness are much less than that of the quartz crystal,

(2) the deposited mass is uniform, rigid and integral to the quartz crystal,

(3) the quartz crystal vibration takes place in vacuum or in air and the frequency change $\Delta f/f_0 \leq 0.02$.

If ρ_f is the density of the deposited material, the thickness (T_f) can be calculated from the following equation

$$T_f = \frac{\Delta m}{\rho_f} = -\frac{\Delta f}{C_f\rho_f} \tag{5.3}$$

The linear equation proposed by Sauerbrey has been extended over time to allow measurement of even greater mass loads deposited on the crystal. If the change in frequency is greater than 2%, that is, $\Delta f/f_0 > 0.02$ the Z-match method must be used to determine the change in mass. The formula for the Z-match method is:

$$\frac{\Delta m}{A} = \frac{N_q\rho_q}{\pi Z f_L}\tan^{-1}\{Z\tan(\pi\frac{f_U - f_L}{f_U})\} \tag{5.4}$$

where f_L is the frequency of loaded crystal (Hz), f_U is frequency of unloaded crystal, i.e. resonant frequency (Hz), N_q is frequency constant for AT-cut quartz crystal ($Hz.\mathring{A}$), Z is the ratio of acoustic impedance of the crystal to that of the deposited film.

All the experiments reported in this study were operated in the sauerbrey regime $\Delta f / f_0 \leq 0.02$.

The temperature of the crystal may increase due to radiant heat exposure from the depositing material source, heat of condensation liberated by depositing atoms and other plasma process conditions [83]. The resonant frequency of the standard A-T cut quartz crystal used here exhibits a strong temperature dependence, typically, the temperature increase of a few degrees celsius results in a frequency shift of 10-100 Hz. This is equivalent to a mass change of 10^{-7} to 10^{-6} g/cm^2 and therefore the crystal must either be kept at a constant temperature to provide reliable results or the temperature effect must be compensated for. A second quartz crystal is incorporated in the design presented here which is not exposed to any deposition and whose role is solely to detect frequency shifts due to temperature alone. This avoids the need for water cooling at the temperatures experienced in many plasma processes.

5.3   Experimental apparatus

5.3.1   The quartz crystal

Inficon AT-cut quartz crystals with 14.0 mm diameter and 0.25 mm thickness are used in this study. These crystals are cut from a bar of synthetic α - quartz at a specific angle $\sim 35^0$ 15' to minimize thermal or stress induced noise. The crystal has a full pad electrode pattern on one
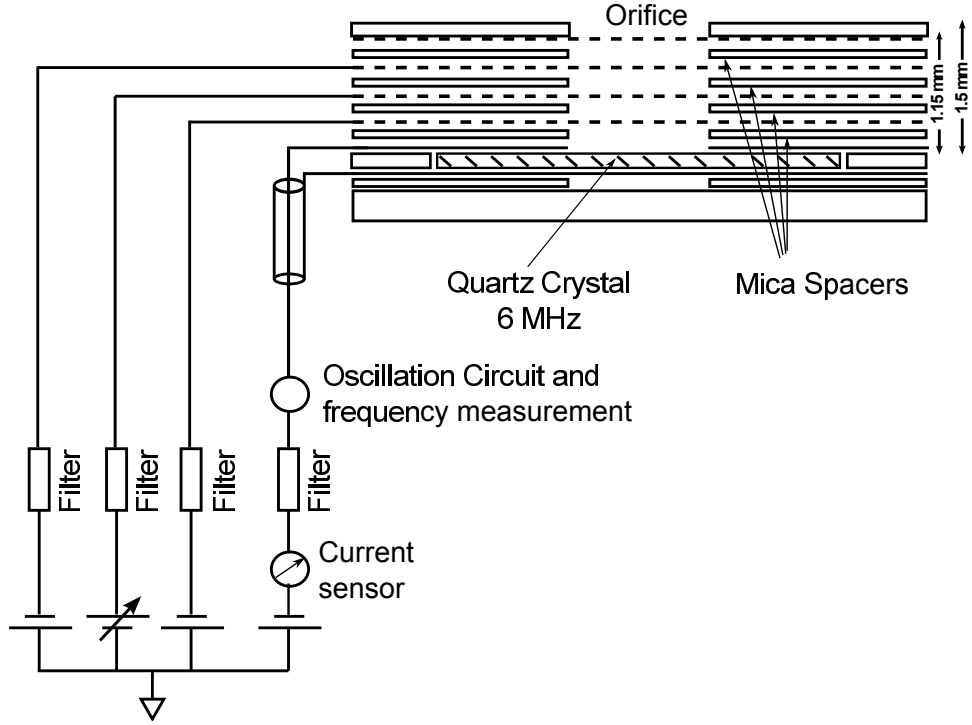
Figure 5.1: *Schematic of QCM embedded RFA design.*

side and a double-anchor electrode pattern on the other side. The double-anchor pattern provides a more reliable electrical connection and focuses the excitation energy into the center area of the crystal to help avoid unwanted vibrational modes. The crystals are oriented with the full pad electrode facing the deposition source and oscillates at its fundamental resonance frequency of 6 MHz when excited with a radio frequency bias.

5.3.2 The QCM integrated RFA design

The schematic of the RFA-QCM structure is shown in figure 5.1. The RFA-QCM consists of a set of 4 grids stacked between the entrance orifice and the quartz crystal. The entrance orifice with a diameter of 5 mm faces the deposition plasma and allows a sample of ions and neutrals into

the sensor for analysis. Grids are separated using electrically insulating rigid mica spacers. Each grid is made from nickel with square shaped windowpane aperture structure with a side length of 20 μm and 50% transmission. The first grid G_0 covers the plasma facing orifice from the back side and so reduces the diameter of the sampling orifice to less than the Debye length to prevent plasma leaking inside the RFA-QCM structure. To measure the IED the other grids are biased in the usual way [50]; ; grid G_1 is biased negatively (-60 V with respect to G_0) to repel plasma electrons; a potential sweep (-10 V to +200 V with respect to G_0 and a step size of 1 V) is applied at grid G_2 to select the energy window; grid G_3 is biased with -70 V to suppress secondary electron emission and collector is biased with the same negative potential as G_1 and used to record the ion current as a function of grid G_2 potential.

To operate the device in deposition rate monitor mode the grid potentials are configured in slightly different way. To measure the total deposition rate from ions+neutrals; G_1 is biased with -60 V to repel plasma electrons and G_2/G_3/Collector are biased to the average dc electrode potential(0 V with respect to G_0). The sensor chassis and G_0 are electrically connected to the electrode potential. Therefore, by setting G_2, G_3 and collector to this potential we do not introduce any additional retarding field for the ions such that all incoming neutrals and positive ions reach the collector/quartz crystal.

To measure the deposition rate from neutrals only; G_1 is biased to repel plasma electrons and G_2/G_3/Collector are biased to a positive potential (+ 150 V) which is sufficiently high to repel the ions. By setting G_2, G_3 and collector to this potential we prevent ions from reaching the quartz crystal and thus the deposition rate measured is due to neutral

species only.

The QCM oscillator and measurement circuit are isolated from ground and the crystal resonates at its natural frequency of 6 MHz. A rf-shielded coaxial cable which protects the signal from external electromagnetic interference is employed to carry the high frequency oscillation signal between the sensor and measurement circuitry located in the vacuum feedthrough on the atmosphere side. The occurrence of a deposition on the crystal surface results in a resonant frequency shift, allowing the deposition rate to be calculated.

When the sensor is placed on a rf biased electrode surface, the orifice plate (which is part of the RFA body) will be rf biased to the same potential as the electrode surface. Thus, for accurate measurements all of the grids and collector plate must also be biased to the same rf potential. To achieve this, low pass filters with high input impedance at the frequencies of interest are placed between all of the grids and the crystal and the RFA electronics as shown in figure 5.1. The detailed description of these filters are described in Chapter 2. These rf filters allows the rf potential at the analyzer body to be almost fully coupled to the grids and crystal (acting as collector as well).

The approach of having the crystal embedded in the RFA allows the device to be miniaturized and therefore provides for a greater range of operating pressures to be achieved. The total depth from orifice to crystal surface is only 1.15 mm. This factor allows a sensor operating limit of approximately 100 mTorr in Ar gas without ion collisions inside the device.
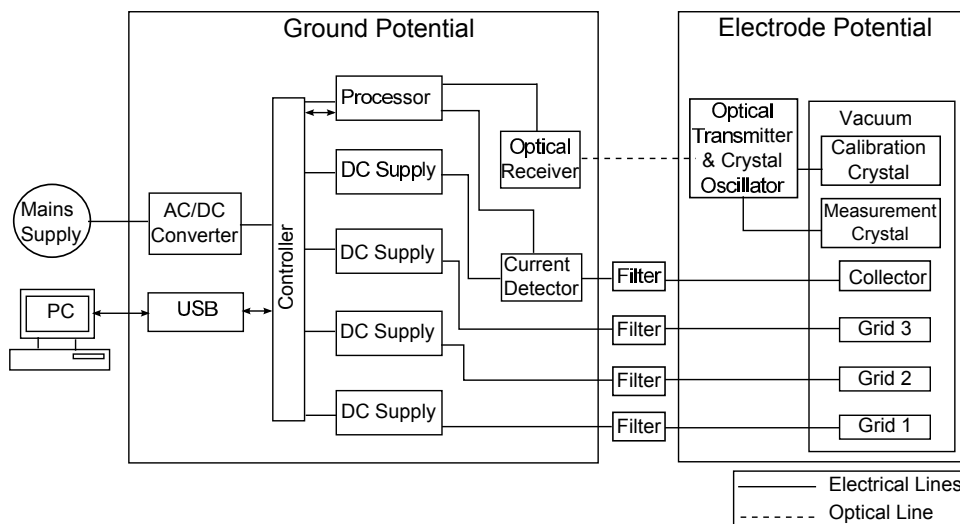
Figure 5.2: *Block diagram of the system electronics and the data acquisition setup.*

5.3.3   Control and measurement electronics

A block diagram of the major components of the system electronics are shown in figure 5.2. There are three main hardware components for this RFA-QCM system including the sensor with cabling, vacuum feedthrough with electronic circuitry and data acquisition control box.

The RFA-QCM sensor consists of a 100 mm diameter mounting plate which holds the two sensing elements containing the measurement and calibration crystals separately. The purpose of the calibration crystal will be discussed in the next section. A cable bundle (650 mm long) containing the lines for the individual grid biasing and the coaxial cables for the crystal oscillator signal extend from the sensor and is terminated with a plug connector which mates to the vacuum feedthrough at the reactor wall.

The vacuum feedthrough forms the interface between the vacuum and the atmosphere. The atmospheric side of the feedthrough has an

integrated enclosure which encases the collector current measurement circuitry and the crystal oscillator and optical transmitter circuitry. The front end of the circuitry is isolated from ground and floats at the electrode bias potential. The back end of this circuitry is at ground potential. A strong isolation barrier separates the two sides. The collector current passes from the floating side to the ground side through the high impedance low pass filters before being measured and digitised on the data acquisition unit. The crystal frequency is detected and digitised on the floating side of the circuitry. The digitised data is optically transmitted across the isolation barrier to an optical receiver on the grounded side. The optical data is converted to an electrical signal and sent to the data acquisition unit for frequency measurement.

The data acquisition unit is powered from the mains supply and communicates with the host personal computer (PC) via universal serial bus (USB) connection. It houses four independent dc power supplies which deliver the required potentials to the RFA-QCM grids. The power supplies are bipolar with a range of $\pm$ 2.5 kV and whose outputs are configured by the user through the main controller board. The on-board processor receives the current and frequency data from the feedthrough. The data is processed and sent to the host PC for further analysis and graphical display.

5.4 Calibration and temperature compensation

The frequency of the quartz crystal changes due to variations in deposition and temperature. Ideally the temperature would be constant

94

Grid Mesh   Nickel Plate

Measurement QCM   Quartz Crystal   Calibration QCM
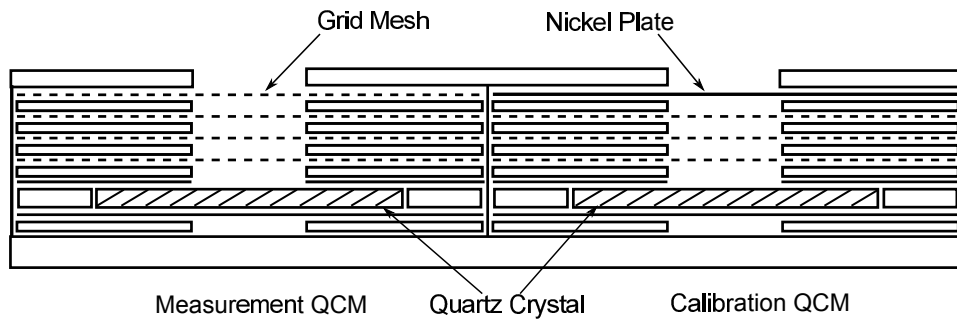
(a)

(b)

Figure 5.3: *(a) Schematic of the QCM deposition rate monitor showing the gridded element and the reference crystal side by side. and (b) Picture of the built sensor integrated in the holder.*

meaning the frequency change would be dependant purely by the deposition. In the absence of water cooling to keep the temperature of the crystal constant, a second crystal which is not exposed to the deposition is used. As shown in figure 5.3 [77], the measurement crystal on the left is open, allowing a measurement of the ion-neutral deposition. The calibration crystal on the right, which is used as a reference, is sealed from any deposition by a closed electrode at the top. However the build structure is otherwise identical in both. As a result there is no measured deposition at this crystal surface. This leads to a frequency change that is caused purely by temperature variations. This allows the determination of the effect that temperature variation has on the crystal frequency. We assume that the temperature change of both crystals is the same. The frequency shift measured on the calibration crystal due to temperature change is used to compensate the measurement crystal and therefore a true measurement of the deposition rate is obtained. The frequency shift from the measurement crystal (QCM1) and the calibration crystal (QCM2) is measured at 10 samples per second. QCM1 provides the main frequency measurement and QCM2 provides data to allow accurate frequency calibration of QCM1. (5.5) is used to calculate the corrected frequency (f_N) which is the resonant frequency of the measurement quartz crystal after being compensated for temperature effects using the calibration quartz crystal.

$$f_N = f_{N(QCM1)} - [f_{N(QCM2)} - f_{0(QCM2)}] \tag{5.5}$$

where $f_{0(QCM2)}$ is the initial resonance frequency of calibration crystal.

Experiments were conducted to determine the accuracy of the temperature compensation method. The dual sensor unit which includes the measurement and the calibration crystals, side by side, was placed inside

96

an oven and the resonance frequency of both crystals were recorded as a function of temperature. This method of heating the dual sensor in an oven does not exactly mimic the real conditions during plasma deposition. In this case the QCM set-up is exposed to the hot walls and heated homogeneously, so both of the crystals are at the same temperature. However, in a vacuum chamber where plasma deposition is taking place, heating of the measurement crystal is caused by impacting species from the plasma. During deposition, the measurement crystal is exposed to the flux of "hot" material (few electron volts) whereas the calibration crystal is not exposed to this material. As a result, a few degrees of temperature difference between the crystals is possible and may add a small error while calculating the corrected frequency. The variation of the two crystal resonance frequencies with respect to temperature and the corrected frequency for perfectly matched and actual crystals are shown in figure 5.4 (a). If the crystals were perfectly matched, in terms of their frequency versus temperature response, then the temperature compensation method would yield a temperature invariant frequency output as shown in the graph. In reality, the individual crystals are not perfectly matched and there is a some disparity between the frequency versus temperature responses. When the temperature compensation method is applied to the real crystals then the corrected frequency is not quite temperature invariant and shows a greater divergence at elevated temperatures. The difference between the corrected frequency for the actual crystals and for the perfectly matched crystals can be defined as a crystal frequency error (δf) and is plotted as a function of temperature in figure 5.4 (b). The error (δf) in corrected frequency increases with increasing temperature and approaches 178 Hz at 160 ^{o}C.
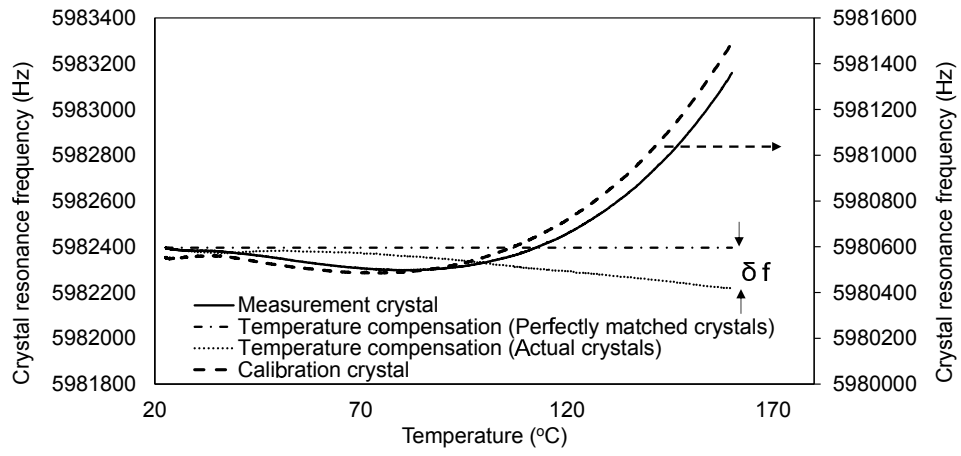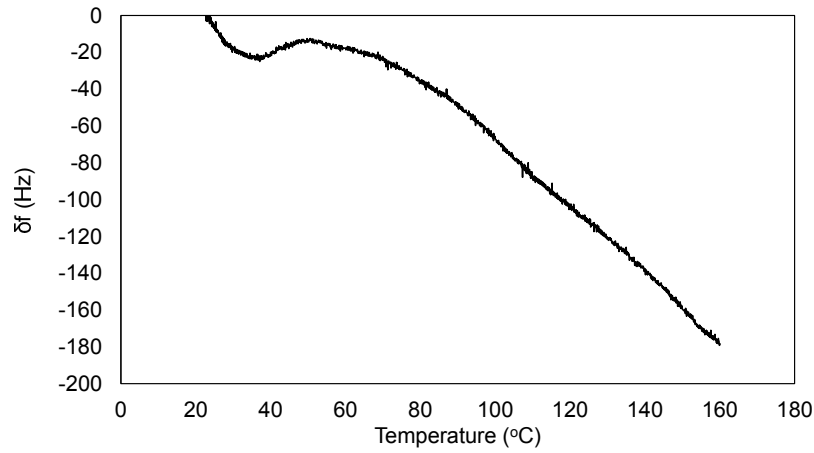
Figure 5.4: *(a) Crystal resonance and corrected frequencies vs temperature for perfectly matched and actual crystals, (b) Crystal frequency error (δf) vs temperature.*

The thickness of the layer T_f deposited on the QCM crystal can be converted to the real layer thickness deposited at the sensor surface by accounting for the grid transmission and the geometrical correction factor as follows:

$$T_{f(substrate)} = \frac{T_{f(sensor)}}{(T_g)^n G} \tag{5.6}$$

T_g is the grid transparency and n is the number of grids used in the sensor. For this RFA-QCM design $(T_g)^n$ is calculated to be 0.0625.

G is the geometrical correction factor which accounts for the shadowing effect caused by the geometry of the sensor design. The magnitude of G determines the magnitude of the shadowing effect. The calculation of G has been performed by Green *et al* [71] and is largely dependent on the aspect ratio of the sensor structure. The value of G has a maximum value of 1 for an aspect ratio of 0. As it approaches this value, there is less of a discrepancy between the measured deposition rate at the sensor surface and the crystal surface. This RFA-QCM design has a shallow structure with overall internal depth of 1.5 mm. The aperture diameter is 5 mm yielding an aspect ratio (l/2R) of 0.305. Using Green's method an estimate of the theoretical geometrical correction factor G is found to be 0.53.

Therefore (5.6) can be rewritten as

$$T_{f(substrate)} = \frac{T_{f(sensor)}}{0.033}. \tag{5.7}$$

(5.7) suggests that the deposited layer thickness at the crystal is 3.3% of that at the sensor surface.

To accurately calculate the deposited layer thickness at the substrate surface the temperature compensation factors must also be included,

therefore using (5.3) and (5.7)

$$T_{f(substrate)} = [\frac{-(f_{N+1} - f_N)\mathrm{x}10^{-6}}{81.5}]/(\rho_f\mathrm{x}0.033) \qquad (5.8)$$

the quartz crystal sensitivity factor (C_f) is 0.0815 Hz/ng/cm^2 for the 6 MHz crystal employed in the design, the density of depositing material (ρ_f) and the product of G and $(Tg)^n$, where the units are in cm. (5.8) uses the corrected frequency calculation from (5.5) at successive time-steps.

The measured variation in the deposition rate calculation before and after the temperature compensation is shown in figure 5.5 (a). Note that this data is recorded in the oven where no deposition is occurring at this time. A magnified view of quadratic fit of the deposition rate measurement is shown in figure 5.5 (b), it is seen clearly that deposition rate after temperature compensation is quite stable and does not vary considerably with temperature as compared to uncompensated deposition rate. The crystal frequency error (δf), due to crystal disparity causes an error in the deposition rate measurement which results in the temperature compensated deposition rate to diverge slightly as the temperature increases. The error in deposition rate is determined by taking the difference between the zero value and the measured deposition rate and is defined as δD. The deposition rate error δD increases with increasing temperature and approaches 0.47 $\mathring{A}/s$ at 160 ^oC.

The RFA-QCM sensor design is capable of measuring a frequency change of 1 Hz. The mass resolution Δm of the deposited layer, given the frequency resolution of 1 Hz, can be determined from (5.2) as 12.3 ng/cm^2.

The deposited mass can now be converted into a layer thickness (T_f) if the density ρ_f of the deposited material is known. For Cu the density
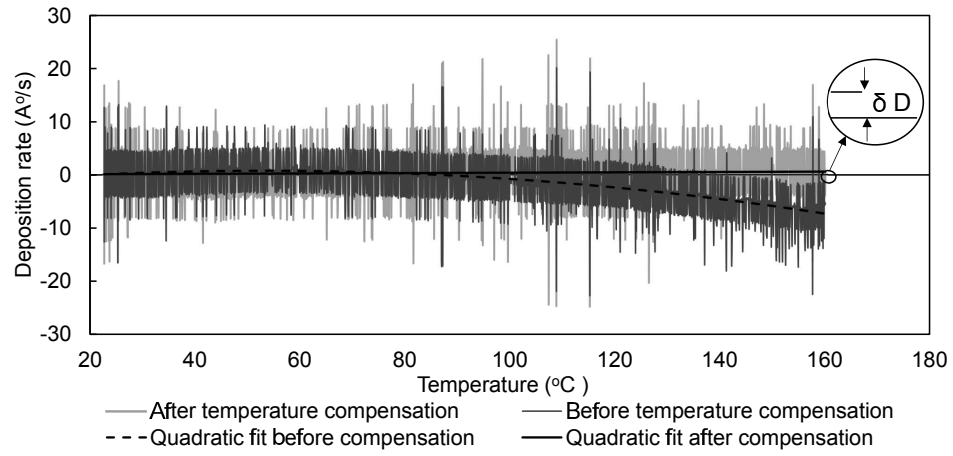
(a)
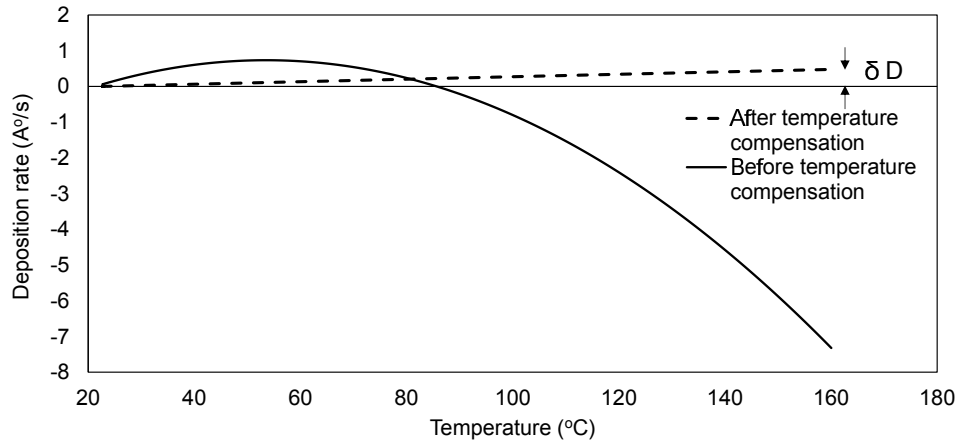
(b)

Figure 5.5: *(a) Deposition rate vs temperature, (b) Quadratic fit showing explicit variation of deposition rate as a function of temperature before and after temperature compensation.*

is 9 g/cm^3 and therefore the film thickness resolution ΔT_f of this device is approximately 0.4 nm.

5.5   Experimental results

Ion energy distribution (IED) and deposition rate of Cu were studied using an asymmetric bipolar p-dc magnetron sputtering tool. An ENI RPG-100 pulse generator was used to drive a planar magnetron fitted with the Cu target in the power regulation mode. The target was 99.99% pure Cu with 50 mm diameter and 6 mm thickness. The distance between target and substrate was set to 9 cm. The RFA-QCM sensor was mounted on the substrate holder. The target was pre-sputtered for 5 min prior to the deposition, to get a stable plasma discharge and to avoid contamination of the deposited film. The chamber was cryopumped and the sputtering was carried out in pure Ar gas. The operating pressure range, which was maintained using a mass flow controller, was 0.4-0.7 Pa. The input power of 100-200 W at a constant pulse frequency of 150 kHz having a pulse width of 2656 ns was applied to the water cooled Cu target during the experiment.

5.5.1   Ion energy distribution

The time-averaged IED's are measured at various p-dc power and pressure conditions on a grounded, floating and rf biased substrate.

The IED's on the grounded substrate holder are shown in figure 5.6 (a) for three different p-dc powers (100 W, 150 W and 200 W) at a fixed pressure of 0.55 Pa (b) for three different pressures (0.4, 0.55 and 0.7 Pa) at a fixed p-dc power of 150 W. The IED curves for the impinging ions
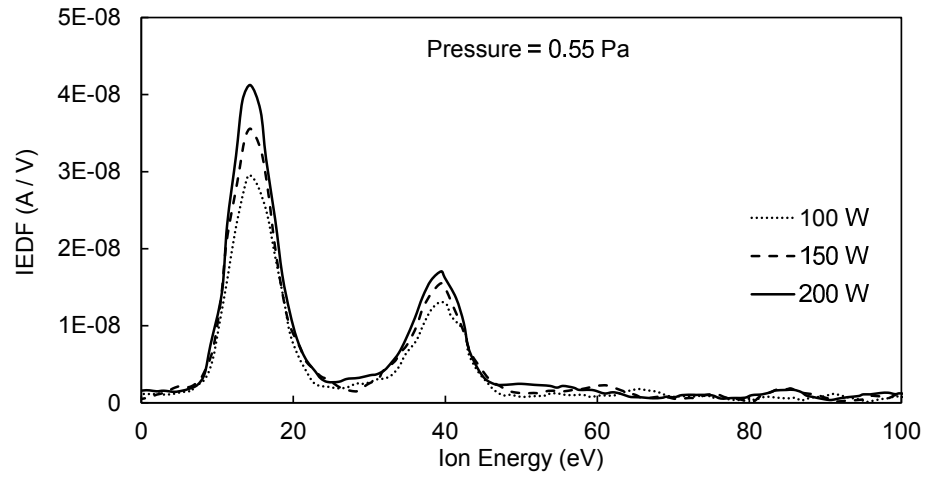
(a)
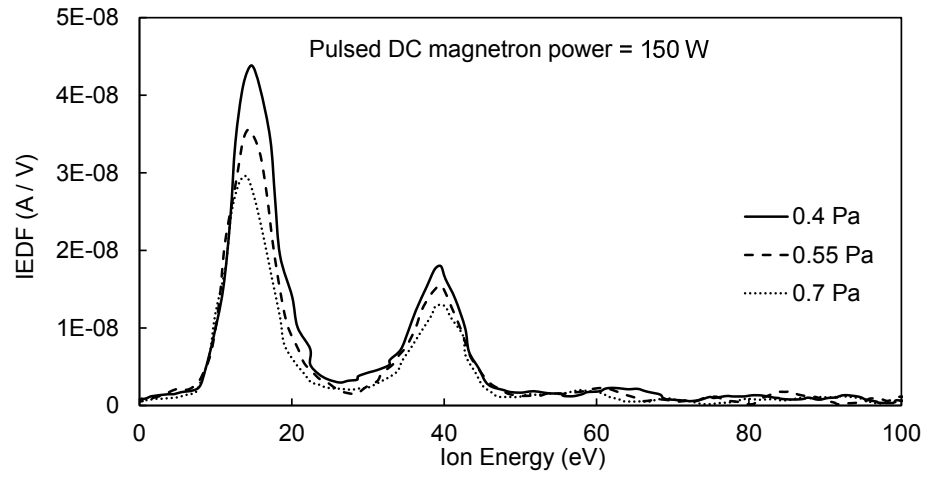
(b)

Figure 5.6: *IED on a grounded substrate at a fixed (a) Pressure and (b) Power.*

exhibit two distinct populations of the ions that reflect the target voltage waveforms. The low ion energy peak corresponds to the negative pulse period (sputtering period) in the target voltage waveform. During this phase of the bias period the plasma potential settles to approximately 15 volts above the grounded chamber wall and ions accelerate towards the grounded substrate with equivalent energy. The higher ion energy peak corresponds to the reverse positive pulse period. During this phase of the bias period the target potential settles to a relatively high positive potential and consequently the plasma potential settles to a more positive value (approximately 40 volts) than during the on time in order to remain the most positive potential in the system. In this period ions are accelerated to a slightly higher energy as seen in figure 5.6. A detailed description of the formation of the distinct populations of the ions in a p-dc magnetron sputtering system has been studied by Pei *et al* [84] and Bradley *et al* [85].

The height of the two peaks increases with increasing discharge power, as shown in figure 5.6 (a), because the height of the peaks, or more accurately the area under the IED, is proportional to the ion flux which is expected to increase with increasing discharge power. In figure 5.6 (b) IED's are shown at different pressures. The height of the two peaks decreases with increasing pressure because at higher pressures there are more ion collisions and therefore the ion flux to the substrate location decreases.

The IED's measured at the floating substrate holder are shown in figure 5.7 with the same power and pressure set points as for the grounded case. Again the IED structure is explained in detail in references [84] and [85].
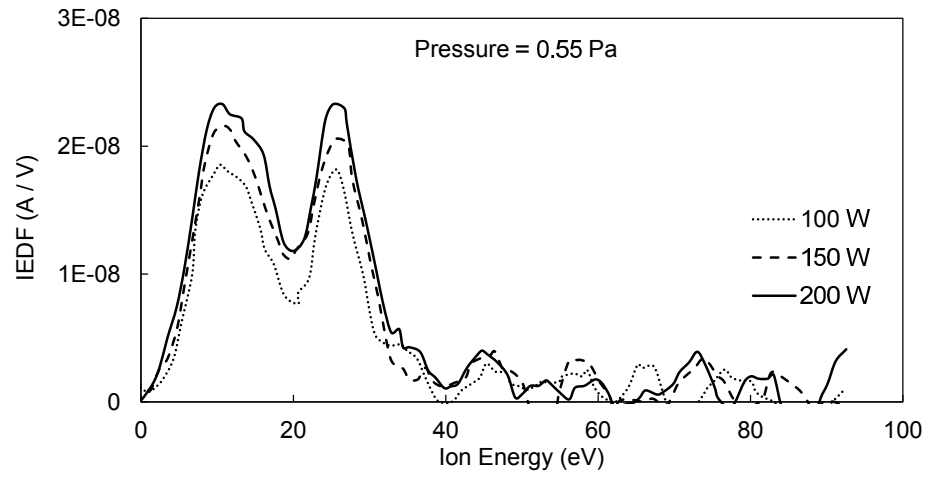
(a)
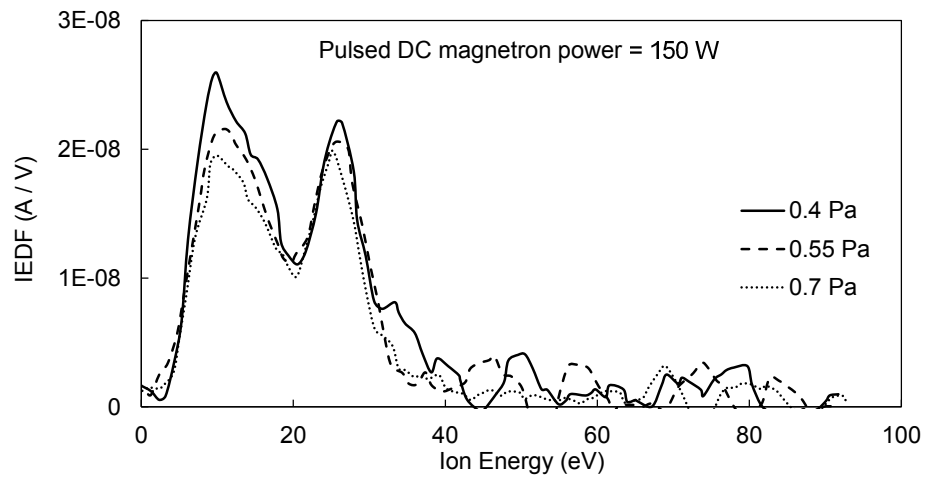
(b)

Figure 5.7: *IED on a floating substrate at a fixed (a) Pressure and (b) Power.*
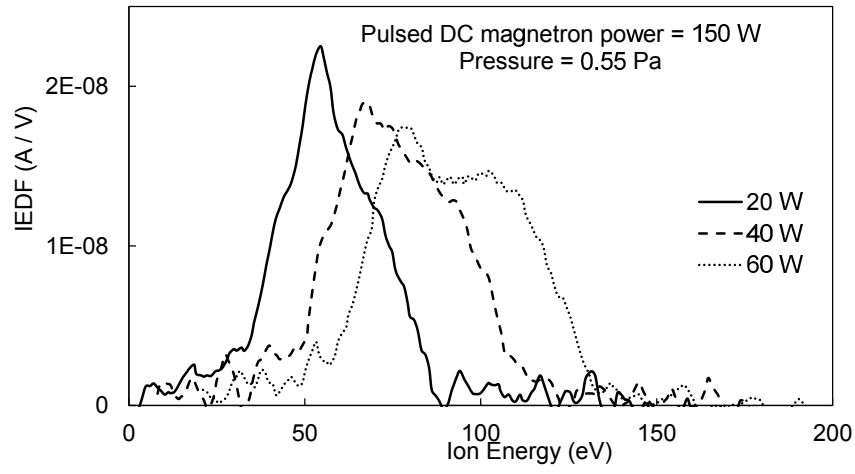
(a)
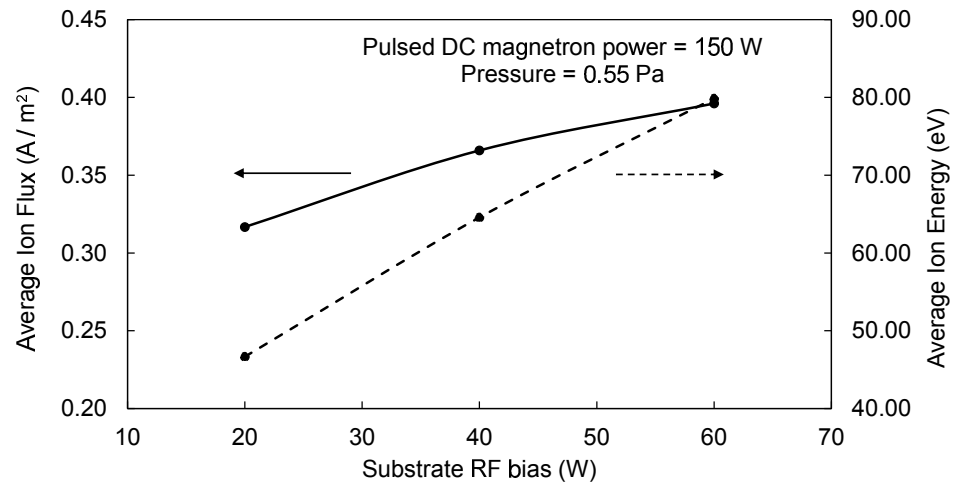
(b)

Figure 5.8: *(a) IED on a substrate biased at three different rf powers (20 W, 40 W and 60 W), (b) Average ion flux and average ion energy vs RF bias.*

One of the main goals of this study was to demonstrate the ability of the developed RFA-QCM design to measure deposition rates at rf biased substrates. To enable this, an additional rf bias has been applied to the substrate holder. While this is not common in this type of deposition tool, it nonetheless provides a convenient platform for testing this design. The effect of rf biasing (at 13.56 MHz) of the substrate on the IED is shown in figure 5.8 (a). The IED exhibits a broadening towards the commonly seen bimodal structure when rf biased plasma sheaths are present. This structure is a consequence of the interaction between rf biased substrate and p-dc driven discharge. With increasing rf bias the IED shifts towards higher energies. Along with the shift to higher energy a broadening in the IED is also visible, consistent with the increased rf voltage drop on the plasma sheath. The average energy of the distribution increases with increasing rf bias. The total ion flux (area under the IED curve) also increases with increasing rf bias which shows that the rf bias contributes to setting the plasma density. The average ion energy $< E >$ and ion flux J_i are calculated using the expressions (2.16) and (2.13) respectively as given in Chapter 2. The corresponding variation of average ion energy and ion flux as a function of substrate rf bias is shown in figure 5.8 (b).

5.5.2 Deposition rate

Before measuring Cu deposition rate, a simple experiment was conducted to examine any influence of substrate rf biasing on the QCM measurement accuracy. When plasma was not turned on and no deposition was taking place, deposition rates were recorded for a time period of 300 seconds at various rf voltages applied to the substrate holder on which the sensor was mounted. No significant effect of rf biasing was observed on
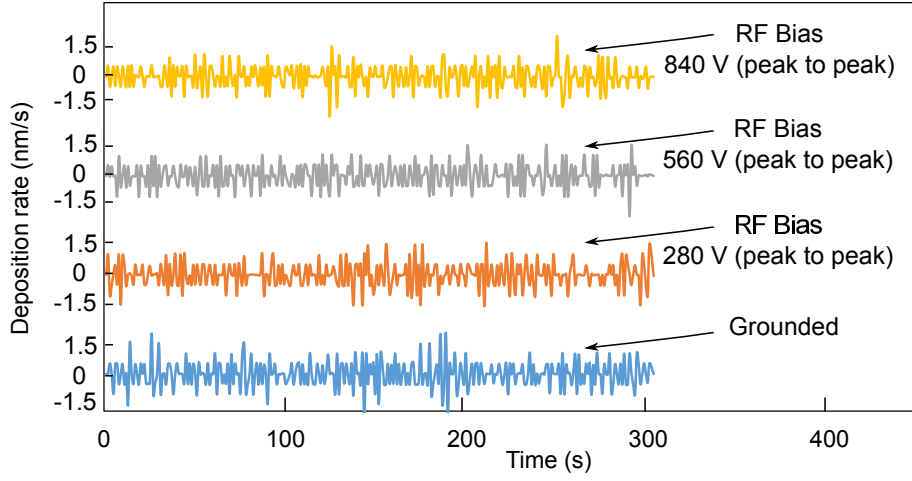
Figure 5.9: *Deposition rate vs time at different substrate rf biasing.*

the accuracy of deposition rate measurement as can be seen in figure 5.9. The rf-shielded coaxial cable and the rf filter placed between the crystals and the measurement electronics protects the signal from any external rf interference.

The metal deposition rates were measured at various p-dc magnetron powers and pressure conditions on a grounded, floating and rf biased substrate. In figure 5.10 the deposition rates are shown at three different p-dc magnetron powers (100, 150 and 200 W) and three different pressures (0.4, 0.55 and 0.7 Pa) on a (a) grounded substrate and (b) floating substrate. The deposition rate increases with increasing p-dc power as expected. The higher magnetron power leads to a higher deposition rate because more neutral atoms are sputtered from the target into the plasma. For a fixed magnetron power the deposition rate decreases with increasing pressure because more sputtered atoms are scattered to the walls of the chamber. The measured deposition rates as a function of p-dc magnetron power and pressures are in agreement with similar
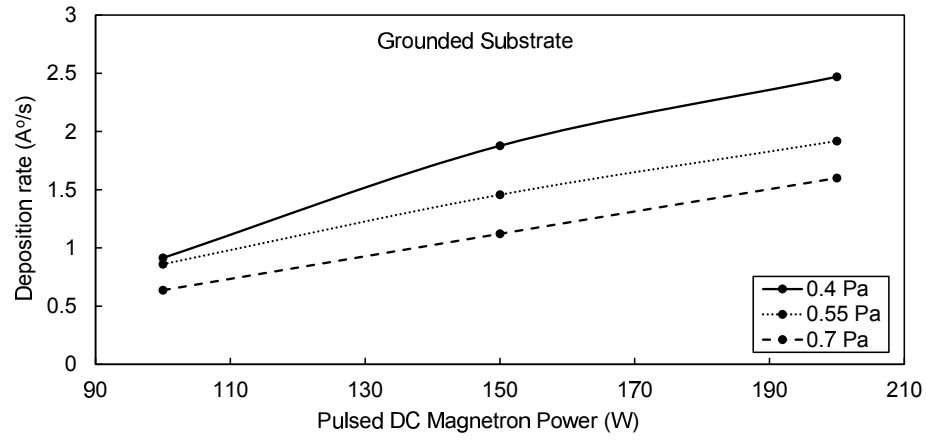
(a)
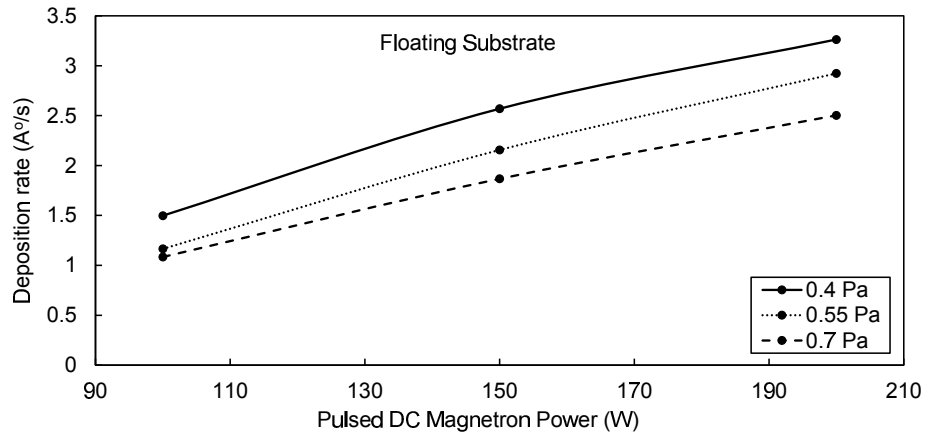
(b)

Figure 5.10: *Deposition rate vs p-dc power at different pressures on a (a) grounded substrate, (b) floating substrate.*

studies made by Hayden *et al* [86].

At a p-dc power of 150 W, deposition rates are measured with and without ions (by applying a potential of + 150 V at G_2/G_3/Collector of the RFA-QCM diagnostic). The deposition versus time graph for a typical run is shown in figure 5.11 (a). The initial part, up to 100 seconds, of the curve shows the accumulation of Cu when only neutrals are incident on the QCM. The second half of the curve (from 100 to 200 seconds) the voltage bias is turned off and the graph shows the deposition due to both neutral and ion impact. By comparing the slopes of two segments it can be seen that the deposition rate drops when the ions are allowed in. The slope of the first segment corresponds to a deposition rate of 0.99 $\mathring{A}/s$ while the slope of the second segment corresponds to a deposition rate of 0.86 $\mathring{A}/s$. The percentage decrease in the deposition rate after ions are turned on is found to be 13%. The decrease in deposition rate is due to the presence of energetic ions which causes metal neutrals to re-sputter during the deposition process and return to the vapour phase.

The percentage decrease in deposition rates after ions are turned on and both ions and neutrals are allowed at three different substrate rf biases (20, 40 and 60 W) and two different pressures (0.4 and 0.7 Pa) is shown in figure 5.11 (b). At the substrate rf bias of 20 W, the percentage decrease in deposition rate is 4%, at 40 W it is 8.5% and at 60 W it is 13%. The percentage decrease in the deposition rate increases with increasing rf bias due to the increasing energy of the incoming Ar ions which resputter more metal particles.

The sputter energy threshold for argon ions is 15.8 eV [87] for copper target. Therefore ions with average energies less than 15.8 eV does not cause resputtering, while ions with energy more than 15.8 eV shows a
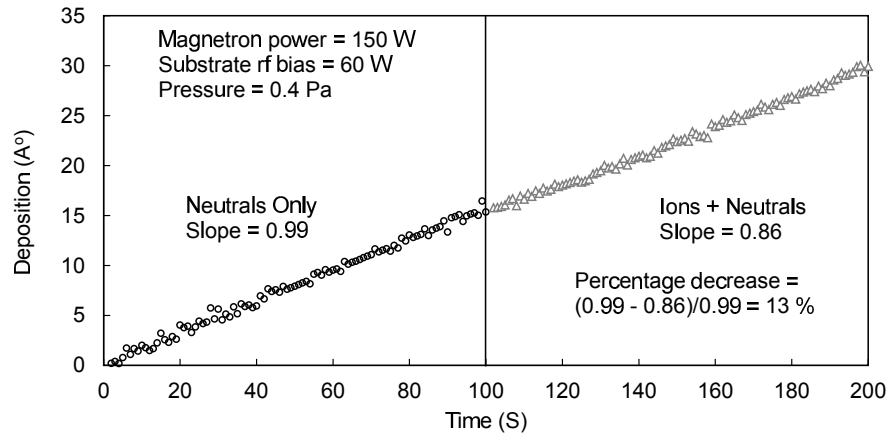
(a)
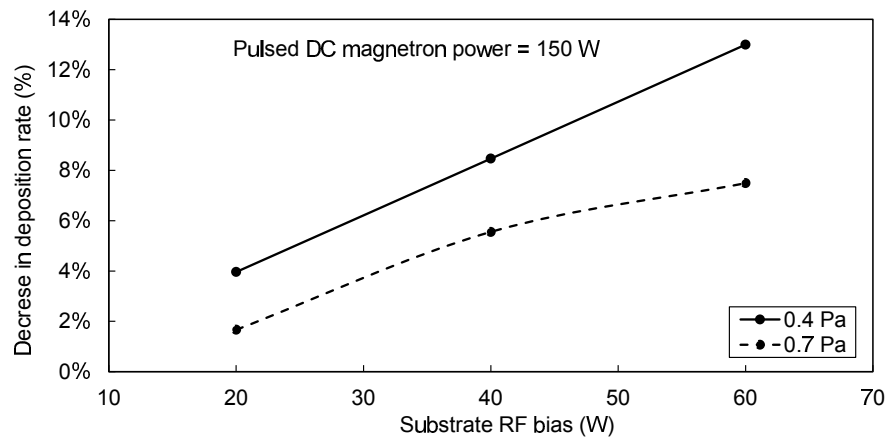
(b)

Figure 5.11: *(a) Deposition vs time graph to determine percentage decrease, (b) Percentage decrease in the deposition rate after ions are turned on.*
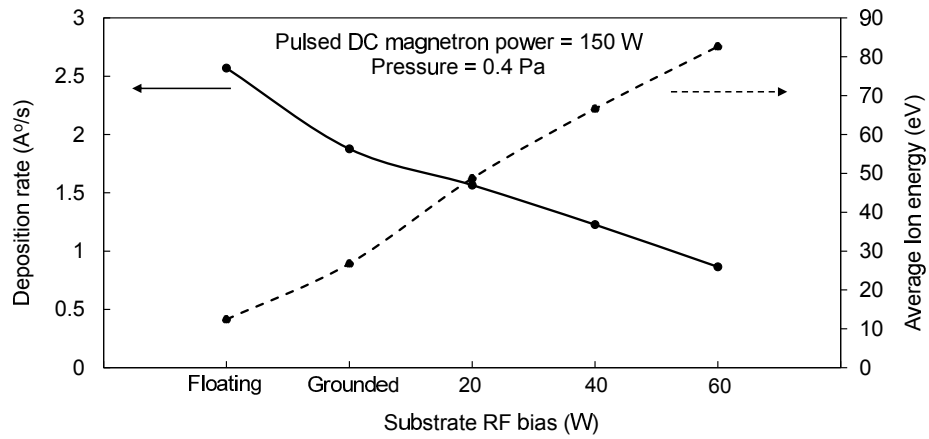
Figure 5.12: *Deposition rate and average ion energy vs different substrate biasing*

linear relation between copper sputter/or resputter yield and argon ion energy. The variation of deposition rate and average ion energy under different substrate biasing conditions at a fixed p-dc power of 150 W and pressure of 0.4 Pa are shown in figure 5.12. When the substrate is floating, the average energy of ions reaching the substrate is at a minimum of 12.4 eV which is less than the threshold, these low energy ions are unable to re-sputter. The average ion energy increases to 26.8 eV when substrate is grounded which is due to enhanced ion acceleration caused by the increased potential difference between the plasma and the substrate. These high energy ions, starts to resputter the depositing material and leads to reduction in overall deposition rate. When substrate is biased at a rf power of 20 W, the substrate attains a self dc bias potential of - 10 V which further enhances the ion acceleration and ions hit the substrate with even higher average energy of 48.7 eV. Similarly for 40 W and 60 W the self dc bias reaches -28 V and -44 V respectively corresponding to average ion energies of 66.6 eV and 82.6 eV respectively. The drop in

deposition rate with increasing average ion energy can be attributed to re-sputtering of deposited material on the substrate due to energetic ion bombardment as explained by Wu *et al* [74]. Foster *et al* [88] demonstrated that for dc magnetron sputtering powers of less than 250 W, the major ion concentration in an Ar/Cu plasma is Ar^+. In our case, the experiment is conducted using p-dc powers in the range of 100-200 W and therefore the ions responsible for re-sputtering of deposited Cu on the substrate are mainly Ar^+.

From figure 5.12, it can be concluded that at higher ion bombarding energies more re-sputtering of metal neutrals will take place. The overall deposition is therefore a compromise between two competing processes: film deposition by metal neutral and ion fluxes and film resputtering by the energetic Ar^+ ions. When the ions are stopped and only neutrals are allowed, no re-sputtering occurs and higher deposition rates are observed.

5.5.3   Ionization fraction

By comparing the net deposition rate to the QCM with and without ions, the ionization fraction of Cu can be determined from the difference between the ion and neutral deposition rates. For p-dc power of 200 W the ionized metal flux fraction on the floating substrate was estimated to be approximately 0.2% across the range of powers and pressures investigated. The ionized metal flux fraction was determined to be less than 5% which is also estimated to be the resolution limit of the device based on multiple measurements under the same conditions. In other words there is a negligible fraction of Cu ionization measured in this deposition process. The uncertainty or error in the ionization fraction measurement is the sum of the errors associated with minor measurement

inaccuracies in (a) crystal resonance frequency and (b) temperature compensation. Generally, in a dc magnetron sputtering system, additional rf power is inductively coupled through a coil to create additional plasma which raises the electron temperature and density and leads to increased ionization of the sputtered metal flux as reported by other researchers [70–72, 86]. Together with introduction of rf power, the chamber pressure is required to be elevated above 1 Pa to achieve a measurable ionization fraction ($\geq 10\%$). At low pressures (< 1 Pa), the sputtered atoms have longer mean free path and reduced residence time in the plasma due to less scattering which leads to less chances of atoms being ionized [73, 89]. The negligible ionization fraction measured in the p-dc system used in our study is as expected because no additional rf plasma was introduced and chamber pressures were ≤ 0.7 Pa. It was not possible to extend the study to higher pressures because a chamber pressure more than 1 Pa was beyond the operating pressure range of the reactor.

5.6   Summary

A compact retarding field analyzer with integrated quartz crystal microbalance is presented. The diagnostic does not suffer from complications caused by water cooling arrangements to maintain constant temperature since a method utilising a reference crystal is implemented to compensate for temperature variations. The unified design is capable of measuring the IED, deposition rate and the ionization fraction and can be placed on a grounded, floating or rf biased electrode without modifying the electrode geometry. The developed diagnostic is an attractive technique for characterizing a thin film deposition system.

The IED, deposition rate and Cu ionization fraction are investigated using the developed diagnostic in an asymmetric bipolar p-dc sputtering reactor. The dependence of IED on chamber pressure, source power and substrate biasing is qualitatively understood. The effect of p-dc power and substrate biasing on the deposition rate are also examined. The film deposition rate is found to be function of two competing processes: film formation by metal neutrals and film resputtering by gas ion bombardments.

CHAPTER 6

Conclusion and future work

6.1 Summary

The research work carried out and presented in this thesis is primarily concerned with the development of novel methods and techniques related to the RFA technology for measurement of ion related parameters in plasma processes. A series of diagnostics have been constructed with definite methods and appropriate geometries which can measure specific parameters related to the plasma ions arriving at the location of the substrate surface. Knowledge of ion specific parameters are highly desired for process engineers in developing and controlling processes for the manufacturing of next generation sub - 10 nm devices and IC chips.

In Chapter 2, detailed description of standard RFA sensors have been given. A number of standard RFA sensors have been constructed. High

input impedance low pass filters have been associated with internal grids and collector plate to enable these analyzers to be placed on a grounded, floating or rf biased electrode without modifying the electrode geometry. The variability between sensors due to manufacturing variations has been tested by conducting a set of experiments. Analyzers were found to have less than 2% variability from unit to unit due to tight manufacturing tolerances. These set of analyzers have been used to build a multi-sensor design which is of measuring the spatial plasma profile. The developed multi-sensor design presents a unique device that can provide information on the spatial variation of plasma properties in a variety of plasma processing systems. The main sensor assembly consisted of a 300 mm anodised aluminium disk to mimic a semiconductor wafer into which thirteen individual, compact-sized, analyzers were embedded and the plasma sampling orifices of each sensor were flush with the disk surface. All thirteen analyzers were multiplexed and controlled by a single acquisition unit. Using this instrument, the ion energy distribution, average ion energy and average ion flux were investigated at thirteen locations over the surface of a powered electrode in a CCP reactor. The discrepancies in ion energy and ion flux across the surface of the electrode were observed to be due to non-uniform plasma profile and the degree of non-uniformity has been determined as 5.1% and 20.2% respectively. Conclusively, the developed multi-sensor design presents a suitable diagnostics to determine the degree of spatial nonuniformity in a plasma reactor. The constructional and operational details of the developed spatially resolved multi-sensor design have been given in Chapter 3.

In Chapter 4, a technique has been presented which we believe is novel to measure ion angle distribution using a planar RFA. An analyt-

ical theory has been derived to define the ion current as a function of incident ion angle, ion energy, aperture geometry and the aspect ratio. The mathematical expression has been derived for ion current and it's numerical solution for the calculation of ion incidence angle has been discussed. The technique is based on varying the effective aspect ratio of the analyzer's aperture to control ions with different angular spread. The technique requires insertion of thin metallic foils, having similar arrays of orifices as that of plasma facing surface, into the standard RFA design. Precise alignment of orifices has been maintained throughout the depth of the sensor. Insertion of these metallic foils alters the internal geometry of a standard RFA sensor but prevents any cross talk from different orifices to take place. The technique suggested in this research work allows ion energy distributions, as a function of ion angle to be measured which adds an important functionality to the planar RFA and can advance the field of plasma diagnostic using this technology. Ion angle measurement is particularly useful for diagnosing rf plasma etching processes where the angular distribution of the impacting ions can play an important role in the process outcome. The angle resolved RFA has been tentatively tested in a CCP reactor and the major angle of ion incidence has been found to be between 0^0 and 3^0 as expected.

In Chapter 5, a compact RFA design with integrated quartz crystal microbalance (QCM) which is capable of measuring the ion energy distribution, deposition rate and the ionization fraction has been presented. The developed RFA-QCM design can be placed on a grounded, floating or rf biased electrode. The unified design has been employed with a novel method utilising an undeposited reference crystal to compensate for temperature variations which eliminate the need for a complex water cooling

118

mechanism. Using the developed sensor the ion energy distribution, deposition rate and ionization fraction of copper has been investigated in a pulsed-dc sputtering reactor. The effect of bombarding argon ion energies over deposition rate has been understood. It has been found that the deposited film was the result of two simultaneous competing processes: film deposition by metal particles and film resputtering by energetic argon ions which causes deposited metal particles to resputter and return to the vapour phase.

All the developed sensor designs and techniques presented in this thesis are not restricted to any specific plasma reactor and can be used to diagnose a variety of plasma discharges including capacitively coupled, inductively coupled and electron cyclotron resonance plasma reactors.

6.2   Suggestions for further work

The possible extension to the work described in this thesis is to apply the developed designs of sensors and techniques to typical plasma assisted deposition and etch systems.

A study of comparing the spatial non-uniformities in ion energy and ion flux to the non-uniformity in deposited thin film thickness across the wafer can be very useful in a plasma deposition reactor using the multi-sensor design described in Chaptet 3. A similar study of comparing the etch uniformity with spatial profile of ion energy and ion flux across the wafer in a plasma etch reactor could be fruitful for process engineers. A radial plasma profile showing the variation of ion energy and flux from center to the edge of the wafer can be studied using the developed multi-sensor design. The knowledge of spatial plasma profile could enable

process engineers to fine tune plasma input parameters in real time i.e pressure, power, chemistry and frequency to find the optimum ion energy and ion flux uniformities. Spatial profile of ion energy and ion flux can be compared to the low and high yielding locations across the wafer.

In the research work presented in Chapter 4, a theoretical model to measure the angular distribution of plasma ions using the planar RFA has been described. The validity of the theoretical model is analyzed by the comparison with the commercial simulation package SIMION. We have also demonstrated the technique on a rf plasma, wherein the charged particle "beam" is simply due to particle acceleration in the sheath between plasma and the RFA, is minimal at best. However, in order to strongly validate the present model and technique a set of experiments under the condition that the ions have a large incident angle are required. Additional work would need to be completed to evaluate this technique using a charged particle beam facility with adjustable energy and ion angle (or simply rotate the RFA with respect to the beam). Validating the method at higher ion angles in wide ion angle plasma processes would make a much stronger and convincing case study.

In the research work presented in Chapter 5, a mathematical formula to compensate for temperature effects in the quartz crystal has been derived. The formula gives an error up to 0.47 $\mathring{A}/s$ at 160 ^{0}C in measuring deposition rate due to disparity in used crystals. A mathematical correction factor which can counterbalance the effect of used crystal disparity needs to be identified and incorporated in to this formula to minimize the error. We have used the RFA-QCM design in studying Cu deposition rate by monitoring the decreasing crystal resonance frequency, the same design and technique can also be used to monitor etch rates in certain

plasma etch processes. Theoretically the crystal resonance frequency is supposed to increase during etch process and by monitoring this increase the etch rate can be calculated. The developed RFA-QCM sensor design can be used to study ionization fractions in various industrial scale HiPIMS processes.

Bibliography

[1] Naokichi Hosokawa, Reisaku Matsuzaki, and Tatsuo Asamaki. Rf sputter-etching by fluoro-chloro-hydrocarbon gases. *Japanese Journal of Applied Physics*, 13(S1):435, 1974.

[2] AFJ Levi. Towards quantum engineering. *PROCEEDINGS-IEEE*, 96(2):335, 2008.

[3] D Gahan, B Dolinaj, and MB Hopkins. Comparison of plasma parameters determined with a langmuir probe and with a retarding field energy analyzer. *Plasma Sources Science and Technology*, 17 (3):035026, 2008.

[4] A Von Keudell and W Jacob. Interaction of hydrogen plasmas with hydrocarbon films, investigated by infrared spectroscopy using an optical cavity substrate. *Journal of Vacuum Science & Technology A*, 15(2):402–407, 1997.

[5] Ankur Agarwal and Mark J Kushner. Seasoning of plasma etching

reactors: Ion energy distributions to walls and real-time and run-to-run control strategies. *Journal of Vacuum Science & Technology A*, 26(3):498–512, 2008.

[6] K Takechi and MA Lieberman. Effect of ion energy on photoresist etching in an inductively coupled, traveling wave driven, large area plasma source. *Journal of Applied Physics*, 89(10):5318–5321, 2001.

[7] Tansel Karabacak and Toh-Ming Lu. Enhanced step coverage by oblique angle physical vapor deposition. *Journal of applied physics*, 97(12):124504, 2005.

[8] `http://www.slideplayer.com.br/slide/46954`. Slide 5.

[9] KS Fancey, CA Porter, and A Matthews. Relative importance of bombardment energy and intensity in ion plating. *Journal of Vacuum Science & Technology A*, 13(2):428–435, 1995.

[10] MMM Bilek, DR McKenzie, RN Tarrant, SHM Lim, and DG McCulloch. Plasma-based ion implantation utilising a cathodic arc plasma. *Surface and Coatings Technology*, 156(1):136–142, 2002.

[11] Henry Windischmann. Intrinsic stress in sputter-deposited thin films. *Critical Reviews in Solid State and Material Sciences*, 17(6): 547–596, 1992.

[12] Edmond De Hoffmann, Jean Charette, Vincent Stroobant, and Jennifer Brodbelt. Mass spectrometry: principles and applications. *Journal of the American Society for Mass Spectrometry*, 8(11):1193–1194, 1997.

[13] CG Herbert and RAW Johnstone. Mass spectrometry basics. 2003.

123

[14] http://www.orgchemguide.blogspot.in/2011/04/
    magnetic-deflection-or-sector-mass.html.

[15] http://www.alevelnotes.com/Mass-Spectrometry/124.

[16] https://www.studyblue.com/notes/note/n/
    chapter-10-icp-mass-spectrometry-icp-ms/deck/16097312.

[17] Erik A Edelberg, Andrew Perry, Neil Benjamin, and Eray S Aydil.
    Compact floating ion energy analyzer for measuring energy distribu-
    tions of ions bombarding radio-frequency biased electrode surfaces.
    Review of scientific instruments, 70(6):2689–2698, 1999.

[18] D Gahan, B Dolinaj, and MB Hopkins. Retarding field analyzer for
    ion energy distribution measurements at a radio-frequency biased
    electrode. *Review of Scientific Instruments*, 79(3):033502, 2008.

[19] JW Coburn and Eric Kay. Positive-ion bombardment of substrates
    in rf diode glow discharge sputtering. *Journal of Applied Physics*,
    43(12):4965–4971, 1972.

[20] K Köhler, JW Coburn, DE Horne, E Kay, and JH Keller. Plasma
    potentials of 13.56-mhz rf argon glow discharges in a planar system.
    Journal of applied physics, 57(1):59–66, 1985.

[21] SG Ingram and N St J Braithwaite. Ion and electron energy analysis
    at a surface in an rf discharge. *Journal of Physics D: Applied Physics*,
    21(10):1496, 1988.

[22] AD Kuypers and HJ Hopman. Ion energy measurement at the pow-
    ered electrode in an rf discharge. *Journal of applied physics*, 63(6):
    1894–1898, 1988.

[23] WM Holber and J Forster. Ion energetics in electron cyclotron resonance discharges. *Journal of Vacuum Science & Technology A*, 8 (5):3720–3725, 1990.

[24] AD Kuypers and HJ Hopman. Measurement of ion energy distributions at the powered rf electrode in a variable magnetic field. *Journal of Applied Physics*, 67(3):1229–1240, 1990.

[25] SG Ingram and N St J Braithwaite. rf modulation of positive-ion energies in low-pressure discharges. *Journal of applied physics*, 68 (11):5519–5527, 1990.

[26] Joachim Janes and Christoph Huth. Bombardment energies of o2+ in low pressure reactive ion etching. *Applied physics letters*, 61(3): 261–263, 1992.

[27] C Charles, RW Boswell, and RK Porteous. Measurement and modeling of ion energy distribution functions in a low pressure argon plasma diffusing from a 13.56 mhz helicon source. *Journal of Vacuum Science & Technology A*, 10(2):398–403, 1992.

[28] Christian Böhm and Jérôme Perrin. Retarding-field analyzer for measurements of ion energy distributions and secondary electron emission coefficients in low-pressure radio frequency discharges. *Review of scientific instruments*, 64(1):31–44, 1993.

[29] Joseph R Woodworth, Merle E Riley, Dorothy C Meister, Ben P Aragon, Minh S Le, and Herbert H Sawin. Ion energy and angular distributions in inductively coupled radio frequency discharges in argon. *Journal of applied physics*, 80(3):1304–1311, 1996.

[30] Francis F Chen and Jane P Chang. Principles of plasma processing. *Univ. of California, book*, 2002.

[31] Guillermo Donoso and Pablo Martin. Grid effects on velocity analyzers of variable geometry. *Review of scientific instruments*, 57(8): 1501–1506, 1986.

[32] CL Enloe and JR Shell. Optimizing the energy resolution of planar retarding potential analyzers. *Review of scientific instruments*, 63 (2):1788–1791, 1992.

[33] I. H Hutchinson. *Principles of Plasma Diagnostics*. Cambridge: Cambridge University Press, 2005.

[34] C Hayden, D Gahan, and MB Hopkins. Ion energy distributions at a capacitively and directly coupled electrode immersed in a plasma generated by a remote source. *Plasma Sources Science and Technology*, 18(2):025018, 2009.

[35] K Denieffe, CMO Mahony, PD Maguire, D Gahan, and MB Hopkins. Retarding field energy analyser ion current calibration and transmission. *Journal of Physics D: Applied Physics*, 44(7):075205, 2011.

[36] http://www.impedans.com/semion-single-sensor, .

[37] Yoshiyuki Sakai and Ituso Katsumata. An energy resolution formula of a three plane grids retarding field energy analyzer. *Japanese Journal of Applied Physics*, 24(3R):337, 1985.

[38] GD Conway, AJ Perry, and RW Boswell. Evolution of ion and

electron energy distributions in pulsed helicon plasma discharges. *Plasma Sources Science and Technology*, 7(3):337, 1998.

[39] D Gahan, S Daniels, C Hayden, MB Hopkins, et al. Characterization of an asymmetric parallel plate radio-frequency discharge using a retarding field energy analyzer. *Plasma Sources Science and Technology*, 21(1):015002, 2012.

[40] D Gahan, S Daniels, C Hayden, P Scullin, D O'Sullivan, YT Pei, and MB Hopkins. Ion energy distribution measurements in rf and pulsed dc plasma discharges. *Plasma Sources Science and Technology*, 21 (2):024004, 2012.

[41] http://www.impedans.com/octiv-suite, .

[42] http://www.impedans.com/langmuir-probe, .

[43] Jin-Yong Kim, Se-Jin Oh, Young-Cheol Kim, Ik-Jin Choi, and Chin-Wook Chung. Wireless wafer-type probe system for measurement of two-dimensional plasma parameters and spatial uniformity. *Measurement Science and Technology*, 24(9):095102, 2013.

[44] Moshe Sarfaty, Michael Harper, and Noah Hershkowitz. A novel electro-optical probe to diagnose plasma uniformity. *Review of scientific instruments*, 69(9):3176–3180, 1998.

[45] David A White, Duane Boning, Stephanie Watts Butler, and Gabriel G Barna. Spatial characterization of wafer state using principal component analysis of optical emission spectra in plasma etch. *Semiconductor Manufacturing, IEEE Transactions on*, 10(1):52–61, 1997.

[46] Allan J Lichtenberg and MA Lieberman. *Principles of plasma discharges and materials processing.* New York: Wiley, 1994.

[47] I Denysenko, MY Yu, and S Xu. Effect of plasma nonuniformity on electron energy distribution in a dusty plasma. *Journal of Physics D: Applied Physics*, 38(3):403, 2005.

[48] SK Ahn and HY Chang. Experimental observation of the inductive electric field and related plasma nonuniformity in high frequency capacitive discharge. *Applied Physics Letters*, 93(3):031506, 2008.

[49] Sychyi Fang and James P McVittie. Charging damage to gate oxides in an o2 magnetron plasma. *Journal of applied physics*, 72(10):4865–4872, 1992.

[50] S Sharma, D Gahan, S Kechkar, S Daniels, and MB Hopkins. A spatially resolved retarding field energy analyzer design suitable for uniformity analysis across the surface of a semiconductor wafer. *Review of Scientific Instruments*, 85(4):043509, 2014.

[51] `http://www.oxfordinstruments.com`. Plasma Etch Systems.

[52] S Kechkar, P Swift, J Conway, M Turner, and S Daniels. Investigation of atomic oxygen density in a capacitively coupled o2/sf6 discharge using two-photon absorption laser-induced fluorescence spectroscopy and a langmuir probe. *Plasma Sources Science and Technology*, 22(4):045013, 2013.

[53] Francis F Chen and Jane P Chang. *Lecture notes on principles of plasma processing.* Springer Science & Business Media, 2003.

[54] `http://www.impedans.com/semion-multi-sensor`, .

[55] J Janes, U Bänziger, Ch Huth, P Hoffmann, G Neumann, H-C Scheer, B Schneemann, and U Köhler. Analysis of large-area beam attacks on surfaces and testing of etching reactions. *Review of scientific instruments*, 63(1):48–55, 1992.

[56] Joachim Janes. Mass-selected ion angular impact energy distributions at the powered electrode in cf4 reactive-ion etching. *Journal of applied physics*, 74(1):659–667, 1993.

[57] Joachim Janes. Angular impact energy distributions of argon ions at the powered electrode of a helicon plasma source. *Journal of Vacuum Science & Technology A*, 12(1):97–105, 1994.

[58] J Liu, GL Huppert, and HH Sawin. Ion bombardment in rf plasmas. *Journal of applied physics*, 68(8):3916–3934, 1990.

[59] JR Woodworth, ME Riley, PA Miller, CA Nichols, and TW Hamilton. Ion distribution functions in inductively coupled radio frequency discharges in argon–chlorine mixtures. *Journal of Vacuum Science & Technology A*, 15(6):3015–3023, 1997.

[60] JR Woodworth, ME Riley, PA Miller, GA Hebner, and TW Hamilton. Ion energy and angular distributions in inductively driven radio frequency discharges in chlorine. *Journal of applied physics*, 81(9): 5950–5959, 1997.

[61] RL Stenzel, R Williams, R Agüero, K Kitazaki, A Ling, T McDonald, and J Spitzer. Novel directional ion energy analyzer. *Review of Scientific Instruments*, 53(7):1027–1031, 1982.

[62] RL Stenzel, W Gekelman, N Wild, JM Urrutia, and D Whelan. Directional velocity analyzer for measuring electron distribution func-

tions in plasmas. *Review of Scientific Instruments*, 54(10):1302–1310, 1983.

[63] Yassir Azziz. *Experimental and theoretical characterization of a Hall thruster plume.* PhD thesis, Massachusetts Institute of Technology, 2007.

[64] Shailesh Sharma, David Gahan, Paul Scullin, Stephen Daniels, and MB Hopkins. Ion angle distribution measurement with a planar retarding field analyzer. *Review of Scientific Instruments*, 86(11): 113501, 2015.

[65] http://www.simion.com. SIMION Version 8.0.

[66] https://www.impedans.com/vertex-single-sensor.

[67] Johan Bohlmark, Jones Alami, Chris Christou, Arutiun P Ehiasarian, and Ulf Helmersson. Ionization of sputtered metals in high power pulsed magnetron sputtering. *Journal of Vacuum Science & Technology A*, 23(1):18–22, 2005.

[68] M Yamashita. Fundamental characteristics of built-in high-frequency coil-type sputtering apparatus. *Journal of Vacuum Science & Technology A*, 7(2):151–158, 1989.

[69] SM Rossnagel and J Hopwood. Magnetron sputter deposition with high levels of metal ionization. *Applied physics letters*, 63(24):3285–3287, 1993.

[70] SM Rossnagel and J Hopwood. Metal ion deposition from ionized mangetron sputtering discharge. *Journal of Vacuum Science & Technology B*, 12(1):449–453, 1994.

[71] KM Green, DB Hayden, DR Juliano, and DN Ruzic. Determination of flux ionization fraction using a quartz crystal microbalance and a gridded energy analyzer in an ionized magnetron sputtering system. *Review of scientific instruments*, 68(12):4555–4560, 1997.

[72] Monica MC Allain, DB Hayden, DR Juliano, and DN Ruzic. Characterization of magnetron-sputtered partially ionized deposition as a function of metal and gas species. *Journal of Vacuum Science & Technology A*, 18(3):797–801, 2000.

[73] Liang Meng, Ramasamy Raju, Randolph Flauta, Hyungjoo Shin, David N Ruzic, and Douglas B Hayden. In situ plasma diagnostics study of a commercial high-power hollow cathode magnetron deposition tool. *Journal of Vacuum Science & Technology A*, 28(1): 112–118, 2010.

[74] L Wu, E Ko, A Dulkin, KJ Park, S Fields, K Leeser, L Meng, and DN Ruzic. Flux and energy analysis of species in hollow cathode magnetron ionized physical vapor deposition of copper. *Review of Scientific Instruments*, 81(12):123502, 2010.

[75] Thomas G Snodgrass, John H Booske, Weitung Wang, Amy E Wendt, and J Leon Shohet. Gridless ionized metal flux fraction measurement tool for use in ionized physical vapor deposition studies. *Review of scientific instruments*, 70(2):1525–1529, 1999.

[76] P Poolcharuansin, M Bowes, TJ Petty, and JW Bradley. Ionized metal flux fraction measurements in hipims discharges. *Journal of Physics D: Applied Physics*, 45(32):322001, 2012.

[77] https://www.impedans.com/quantum-single-sensor.

[78] H Bartzsch, P Frach, and K Goedicke. Anode effects on energetic particle bombardment of the substrate in pulsed magnetron sputtering. *Surface and Coatings Technology*, 132(2):244–250, 2000.

[79] S Schiller, K Goedicke, J Reschke, V Kirchhoff, S Schneider, and F Milde. Pulsed magnetron sputter technology. *Surface and Coatings Technology*, 61(1):331–337, 1993.

[80] WD Sproul. High-rate reactive dc magnetron sputtering of oxide and nitride superlattice coatings. *Vacuum*, 51(4):641–646, 1998.

[81] Shailesh Sharma, David Gahan, Paul Scullin, James Doyle, Jj Lennon, Rajani K Vijayaraghavan, Stephen Daniels, and MB Hopkins. Measurement of deposition rate and ion energy distribution in a pulsed dc magnetron sputtering system using a retarding field analyzer with embedded quartz crystal microbalance. *Review of Scientific Instruments*, 87(4):043511, 2016.

[82] GZ Sauerbrey. Use of quartz vibration for weighing thin films on a microbalance. *J. Physik*, 155:206–212, 1959.

[83] Milton Ohring. *The materials science of thin films, 1992.* Academic Press, London.

[84] YT Pei, CQ Chen, KP Shaha, J Th M De Hosson, JW Bradley, SA Voronin, and M Čada. Microstructural control of tic/ac nanocomposite coatings with pulsed magnetron sputtering. *Acta Materialia*, 56(4):696–709, 2008.

[85] JW Bradley, H Bäcker, Y Aranda-Gonzalvo, PJ Kelly, and RD Arnell. The distribution of ion energies at the substrate in an asymmet-

ric bi-polar pulsed dc magnetron discharge. *Plasma sources science and technology*, 11(2):165, 2002.

[86] DB Hayden, DR Juliano, KM Green, DN Ruzic, CA Weiss, KA Ashtiani, and TJ Licata. Characterization of magnetron-sputtered partially ionized aluminum deposition. *Journal of Vacuum Science & Technology A*, 16(2):624–627, 1998.

[87] https://www.iap.tuwien.ac.at/www/surface/sputteryield.

[88] JE Foster, AE Wendt, WW Wang, and JH Booske. Determination of metal vapor ion concentration in an argon/copper plasma for ionized physical vapor deposition. *Journal of Vacuum Science & Technology A*, 16(4):2198–2203, 1998.

[89] RS Robinson. Energetic binary collisions in rare gas plasmas. *Journal of Vacuum Science & Technology*, 16(2):185–188, 1979.

Peer Reviewed Journal Publications and Conference Proceedings

Journal Publications

S Sharma, D Gahan, S Kechkar, S Daniels, and MB Hopkins. "A spatially resolved retarding field energy analyzer design suitable for uniformity analysis across the surface of a semiconductor wafer".
Review of Scientific Instruments, 85, 043509 (2014)
$http://dx.doi.org/10.1063/1.4870900$

Shailesh Sharma, Chanel Linnane, David Gahan, Stephen Daniels, Mike B. Hopkins. "Formation of a Double Layer in Electronegative O_2 Plasma".
IEEE Transactions on Plasma Science, 42, 10, 2798 (2014)
$http://dx.doi.org/10.1109/TPS.2014.2313179$

Shailesh Sharma, David Gahan, Paul Scullin, Stephen Daniels, and MB Hopkins. "Ion angle distribution measurement with a planar retarding field analyzer".
Review of Scientific Instruments, 86, 113501 (2015)
$http://dx.doi.org/10.1063/1.4934808$

Shailesh Sharma, David Gahan, Paul Scullin, James Doyle, Jj Lennon, Rajani K. Vijayaraghavan, Stephen Daniels, and M B Hopkins. "Measurement of deposition rate and ion energy distribution in a pulsed dc magnetron sputtering system using a retarding field analyzer with embedded quartz crystal microbalance".
Review of Scientific Instruments, 87, 043511 (2016)
$http://dx.doi.org/10.1063/1.4946788$

Conference Talks

AVS 61st International Symposium & Exhibition - 2014, Baltimore, USA
Plasma Science and Technology; Session: Plasma Diagnostics, Sensors, and Control (PS-WeA)
"Ion angular distributions measured with a planar retarding field analyzer"
$http://www2.avs.org/symposium2014/Papers/Paper_P S{-}WeA7.html$

7th International Conference on HIPIMS - 2016, Sheffield, UK
"Measurement of deposition rate, ionized flux fraction and ion energy distribution in a pulsed dc magnetron sputtering system using a retarding field analyzer with embedded quartz crystal microbalance"
$www.hipimsconference.com$

Conference Poster

Intel Ireland Research Conference (IIRC) - 2015, Dublin, Ireland
Session: Silicon & Nanotechnology Track
"Novel plasma diagnostic techniques for the measurement of ion related parameters"
$http://starcite.smarteventscloud.com/IntelIrelandResearchConference$
2015.